THE UNIVERSITY *of* EDINBURGH

Molecular Simulations of Concentrated Aqueous Salt Solutions and Dipoles

Julien Sindt

Doctor of Philosophy

University of Edinburgh

2016

Declaration

I declare that this thesis was composed by myself and that the work contained therein is my own, except where explicitly stated otherwise in the text.

(*Julien Sindt*)

Abstract

Advances in molecular-simulation methods allow for ever larger systems of particles to be studied and on longer timescales. Calculations are reaching such a scale that they can be used to address a vast range of key questions across chemistry, physics, and engineering. In this work, molecular dynamics and Monte Carlo simulations are employed to address two key areas: the structure and dynamics of simple aqueous ionic salt solutions at high concentrations; and the structure, dynamics, and phase behaviour of dipolar fluids (such as colloidal ferrofluids).

The first part of the work begins with a study of the structure and dynamics in metastable, supersaturated, aqueous solutions of potassium chloride, and the possible relevance of these to the phenomenon of non-photochemical laser-induced nucleation (NPLIN). It is thought that the potassium and chloride ions form long-lived, amorphous clusters that may, under the influence of nanosecond laser pulses, undergo structural reorganisation to form post-critical crystal nuclei. It is found that spontaneous nucleation does not occur on the simulation timescale, but that amorphous clusters do form with cluster lifetimes comparable to those of the shortest laser pulses that can be used in NPLIN (100 picoseconds). Next, an alternative scenario for NPLIN involving rapid laser heating of impurity particles is examined by simulating heated carbon nanoparticles in saturated aqueous solutions of sodium chloride. The concentration at which an aqueous sodium chloride solution first crystallises on the simulation timescale is determined. A spherical carbon impurity is then added to a system with concentration close to, but lower than, the concentration at which crystallisation occurs on the simulation timescale. The effects that adding, and heating, this impurity has on the structure of this near-crystallising system are then observed.

The second part of the work discusses model dipolar fluids, of direct relevance to colloidal ferrofluids (suspensions of magnetised nanoparticles in simple carrier liquids). The two-body, dipole-dipole interaction is long-ranged and anisotropic,

and it is computationally expensive to handle in molecular simulations. Here a new method is proposed that relies on a formal mapping between the partition function of a dipolar fluid and that of a hypothetical fluid with many-body, short-ranged, isotropic interactions. Only the leading-order two-body interactions (akin to the van der Waals attraction) and three-body interactions (corresponding to the Axilrod-Teller potential) are retained. It is shown that this simple model is sufficient to reproduce the characteristic particle chaining and the associated disappearance of the vapour-liquid phase transition of dipolar fluids. Finally, the dynamical response of ferrofluids to oscillating magnetic fields (the dynamic magnetic susceptibility [DMS]) is studied. The DMS of ferrofluids, predicted by a new theory that takes into account the leading-order effects of dipole-dipole interactions, are critically compared to those found using Brownian-dynamics simulations of monodisperse systems of dipolar particles. This new theory is found to provide more accurate predictions of the DMS than previous theories, with the DMS predicted to a high degree of accuracy for systems with dipolar coupling strength in the experimentally achievable region.

Acknowledgements

Firstly, I would like to thank my Ph.D. supervisor, Dr. Philip J. Camp, for the many fun project ideas, the helpful discussions, and for always being there to answer my (not always) work-related questions. Without his help, support, and patience this task would have been much more complicated.

I would also like to thank the other members of the group, namely Dr. Michael Doig for teaching me the ways of molecular dynamics and for patiently putting up with my many, many queries; Josh Bradley-Shaw for our vibrant 'work-related' discussion; and, Rui Apóstolo and Georgia Tsagkaropoulou. Thanks as well to everyone in the Theoretical and Computational Groups. Without you, the last three years would have been a lot less fun.

I would also like to acknowledge and thank my many collaborators. In particular, I would like to thank Dr. Ekaterina Elfimova and Professor Alexey Ivanov for inviting me to spend an amazing month in Russia and for the helpful discussions on ferrofluids, and Dr. Andrew Alexander and Dr. Martin Ward for the many fun talks on crystallisation, for letting me watch many NPLIN experiments, and for the many late-evening 'group meetings' that inevitably ensued.

EPSRC provided the studentship that enabled me to spend 3 years learning about and researching many interesting systems. For that, I would like to thank them too.

Lastly, I'd like to thank Laura Glendinning for putting up with me through these four years (and for the occasional proof-readings), and my family for their constant encouragement and support.

If I have forgotten anyone, I 'd like to thank you too, both for the help that you have contributed and for being so understanding of my awful memory with names.

Contents

Chapter 1

Introduction

Recent experimental advances in the fields of physics, chemistry, and biology have led to many new and interesting discoveries. The past century has seen huge leaps forward in all three fields, with each advance also influencing the technology available for research. It is now possible to detect particles of smaller size than was thought to exist in the 19^{th} century and to measure time-scales shorter than were thought to exist. With each new discovery, new questions arise. Often, these questions can only be solved *via* the visualization of smaller elements over shorter timescales that are not yet experimentally achievable. This has allowed for new, non-experimental predictive fields to develop, namely theory and simulation. Both methods have very interesting features. Firstly, they can be used to confirm that the current view of the physical world is accurate (or, rather, not inaccurate). This is usually best done by testing a theory against known experimental results or by predicting results that have recently become achievable (or are close to achievable). Secondly, theory and simulation can make predictions that help to direct experimental developments. This is best exemplified by the large scientific infrastructures that have been built in recent years (*e.g.* the LHC for the detection of primary particles, LIGO for the detection of gravitational waves, *et cetera*).

A very useful predictive tool, developed in the latter half of the 20^{th} century, has been the use of molecular simulations. These have enabled the modelling of systems on scales not experimentally observable. It is possible to run a simulation to look at a process that occurs on the femtosecond timescale. Simulations are usually cheap to run, with the main costs being computational power and time, and can provide accurate detail about systems of interest. The field has vastly improved in the past few years. A (very) brief introduction to molecular

simulation methods is given in Chapter 2.

In this thesis, results from molecular simulations are presented and discussed. The work herein relates to two systems. Both systems have strong experimental basis, and the simulation work studies phenomena that are currently not experimentally observable. The first half of this thesis (Chapters 3 and 4) relates to the structure of aqueous salt solutions at high concentrations, near and above the saturation point, with particular interest in the processes undergone by these systems when non-photochemical laser-induced nucleation (NPLIN) occurs. Experimental studies of supersaturated systems are difficult because of the tendency of these systems to nucleate. Furthermore, short-lived structures in these dilute solutions are nearly impossible to observe experimentally. The second part of this thesis (Chapters 5 and 6) describes work on systems of nanoparticles with magnetic dipoles. It has been possible to create magnetic nanoparticles for a long time, but recent developments have increased the strength of the magnetic dipole that can be experimentally reached. This drastically increases the potential applications of these systems to real-world problems. Though they have greater potential applications, it remains difficult to create monodisperse systems of dipole particles. Simulations enable calculations to be done for monodisperse systems of dipolar nanoparticles, and it is easy to simulate systems of particles with dipole strengths much greater than experimentally achievable. This makes simulations perfect for predicting the properties of systems that will soon be achievable. In this introductory chapter, the principles of NPLIN and of ferrofluids are introduced.

1.1 A brief introduction to NPLIN

In 1996, Garetz *et al.* demonstrated that it is possible to induce crystallisation in aged supersaturated aqueous urea solution by using laser pulses [1]. This was achieved using a laser wavelength of 1.06 μm, significantly lower than the frequency of the lowest absorption band of urea (200 nm) and higher than the highest frequency of vibrational bands (1.4 μm), implying that the observed crystallisation was a non-photochemical process. In 2001, the same group showed that systems other than aqueous urea solutions could undergo NPLIN. While studying aqueous glycine solutions, they found that, not only could glycine undergo NPLIN, but also the polarisation of the laser light could influence the

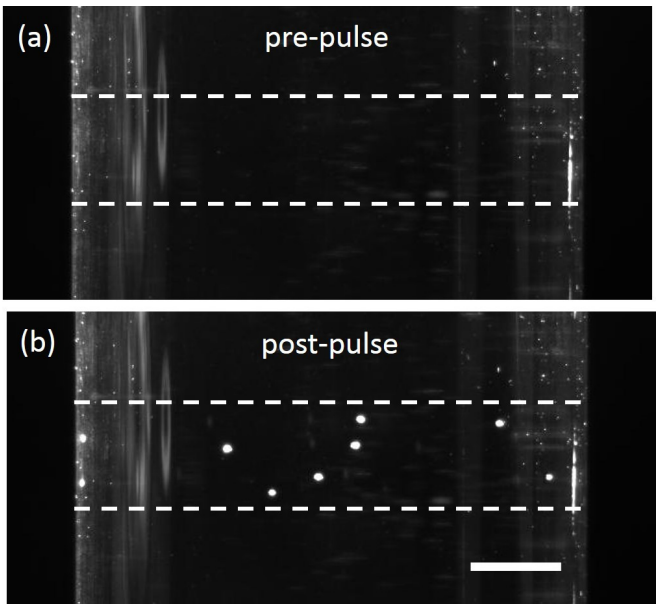

Figure 1.1: Demonstration of the NPLIN effect. (a) Supersaturated ammonium chloride solution (at concentration $b = 1.07\ b_{\mathrm{sat}}$) before laser pulse; (b) same solution moments after laser pulse has been shot into solution. The dashed lines are to illustrate the width of the laser beam. Pictures reproduced with permission of Martin Ward.

crystalline polymorph being formed. Using plane-polarised laser light induces the crystallisation of the polar γ-polymorph of glycine rather than the more stable α-polymorph [2], while circular-polarised laser light induces the nucleation of α-glycine only [3, 4].

The list of known systems that can undergo NPLIN has been steadily increasing, with systems as varied as egg-white lysozyme [5], L-hystedine [6], aqueous potassium halide solutions [7, 8], molten sodium chlorate [9], supercooled acetic acid [10], and carbon dioxide in carbonated beverages [11] all showing an affinity to nucleate *via* the NPLIN process. Some of these systems (*e.g.* potassium halides) do not need to be aged before crystallisation occurs and there is some debate regarding the necessity of the sample ageing step for any system. Some of these samples have long delays between the laser pulse hitting the sample and crystallisation occurring, whereas others crystallise near-instantaneously. Figures 1.1 and 1.2 show NPLIN occurring in supersaturated aqueous ammonium chloride. In these systems, nucleation is nearly instantaneous and crystals grow to visible sizes in solution very quickly (within seconds) after the laser pulse is shot.

Garetz *et al.* postulated that the influence of the laser polarisation on the glycine polymorph obtained indicates that the mechanism at play must be caused by an

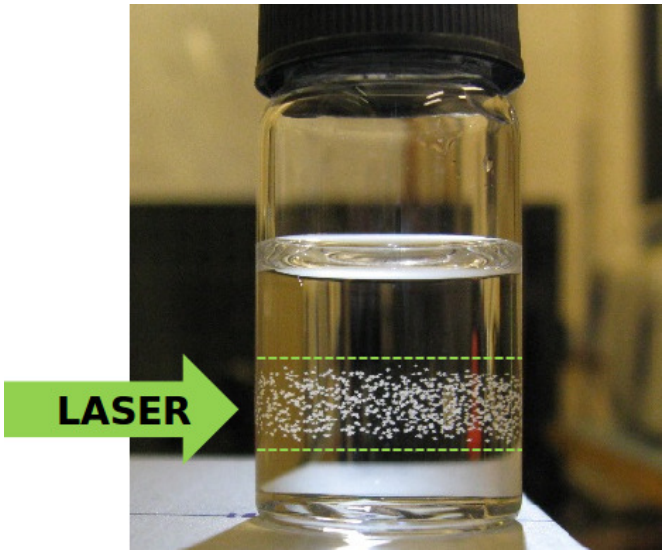

Figure 1.2: NPLIN effect in supersaturated ammonium chloride ($S = 1.07\ S_{\text{sat.}}$). The dashed lines are to illustrate the width of the laser beam. Here, it is emphasised that crystal formation only occurs within the area covered by the laser beam. Picture reproduced with permission of Martin Ward.

optical Kerr effect. In this mechanism, the electromagnetic field of the laser induces a dipole in the solute. The particle then rotates *via* molecular reorientation so that the axis with greatest electric susceptibility aligns with the electromagnetic field. Recent work by Knott *et al.* indicates that, while it is possible to reduce nucleation energy barriers by rearranging particle orientations, the laser field strengths generated by lasers used in NPLIN are much too weak to do this [12]. Furthermore, that potassium halide solutions crystallise *via* NPLIN seems to indicate that the optical Kerr effect is not the mechanism at play. The work of Alexander and Camp shows that the optical Kerr effect is highly unlikely to have any effect on such systems as the refractive indices at 1064 nm (the wavelength of the laser used) of the KCl and water were similar in value ($\varepsilon_{\text{KCl}} = 2.1897$ and $\varepsilon_{\text{H}_2\text{O}} = 1.7535$ [7]). As such, the resulting optical Kerr effect should be negligible. Alexander and Camp further argue that the frequency of laser oscillation is too quick to influence the rotation of a pre-crystallised cluster of KCl in solution. However, the laser oscillation frequency is slower than the absorption frequency for electronic polarisation. Alexander and Camp propose that the electronic polarisation of the solute in pre-crystallising clusters is able to 'follow' the field produced by the laser without phase lag. The general process of NPLIN would then work as follows. First, the supersaturated solution would equilibrate with regions of higher local solute concentration and regions of lower local solute concentration than the average concentration. Amorphous

Figure 1.3: NPLIN effect in carbonated aqueous sucrose solution (CO_2 at 25 psi). Bubbles are clearly seen forming along the path of the laser pulse. Picture reproduced with permission of Martin Ward.

pre-crystal nuclei would form in the areas of higher solute concentration. For systems where the permittivity of the solution is greater than that of the solute, the electromagnetic field produced by shining a laser beam into the solution would align the induced electronic dipoles of the solute particles in the regions of higher solute density, thereby lowering the free energy of the clusters. This alignment process should greatly increases the probability of nucleus formation, as shown below.

Note that this description of the NPLIN process rests on the idea that crystallisation is a two-step process. The most used model to describe nucleation and crystallisation remains the classical nucleation theory (CNT) [13]. This theory is based on the idea that nucleation processes (including crystallisation) occur as a particle-by-particle process. For a system to nucleate, it must be thermodynamically favourable for particles to be in a nucleus. This implies that it is more energetically favourable for the solute particles to be in contact with one another than with the solvent. A stable nucleus will therefore form when the free energy decrease from having solute in a solid particle overcomes the free energy cost of forming an interface with the solution. This is usually represented by the CNT equation, where the Gibbs free energy $\Delta G(r)$ associated with forming a nucleus

of radius r from solution is written as

$$\Delta G(r) = \frac{4}{3}\pi r^3 \Delta g + 4\pi r^2 \gamma \tag{1.1}$$

where γ is the surface tension and $\Delta g < 0$ is the difference in free energy per unit volume of a particle found fully inside the nucleus and one found outside the nucleus. From this, one can obtain the size of the critical nucleus, find the height of the free-energy barrier, and predict the nucleation rate. The addition of an external field can lead to a further reduction in ΔG, hence further increasing the probability of forming a nucleated cluster.

While CNT is a good starting model, many assumptions of this model are now known to be wrong. For instance, this model assumes that clusters will grow by the same mechanisms regardless of size, which is not the case [14–16]; the predicted free energy barrier often does not match that inferred from experimental work [14]; and the nucleation rates predicted by CNT are often wrong by several orders of magnitude [14, 16]. Recently, new models for crystallisation have been proposed. In particular, Erdemir *et al.* propose a two-step nucleation theory [17], where the first step comprises of the formation of pre-nucleating clusters that are amorphous and could be seen as local fluctuation in solute concentration, and the second step occurs when particles in the high density pre-nucleated amorphous cluster reorient to form a crystalline post-critical nucleus. This nucleation model is the one used by Alexander and Camp, and they propose that the NPLIN process increases the probability of the reorientation step taking place.

Other mechanisms have been suggested to explain the NPLIN process. Alexander, Ward, and coworkers have noticed that using highly pure solvents and solutes and using very fine filtration processes decreases the probability of a system undergoing NPLIN [11]. Furthermore, work on NPLIN in carbonated beverages by Alexander and Ward, indicates that sugar-heavy carbonated beverages are more likely to have CO_2 bubbles nucleating than equivalent sugar-free beverages. Both of these results indicate that components other than just the pure solvent and solute may have an effect on the NPLIN process. It has been proposed that impurities act as areas that favour clustering, enabling the first step of crystallisation. It has also been suggested that the laser used in the NPLIN process may cause heating of these impurities, in turn leading to the formation of nano-bubbles that somehow favour the crystallisation process. A study of water cosupersaturated

with Argon gas and glycine carried out by Knott *et al.* corroborates the theory that bubble formation might play an important role in crystallisation [18]. In their work, Knott *et al.* demonstrate that glycine crystals will form in these solutions shortly after argon bubbles are induced *via* shaking. Furthermore, neither of their controls, one with no argon dissolved in the aqueous glycine solution and the other with argon dissolved only to saturated levels, showed any sign of glycine crystallisation occurring.

None of these suggested processes are observable experimentally. It is not currently possible to see a crystal being formed from its solvated components. There is, as yet, no experiment that can detect the shifts in the polarisation of a molecule in solution. It is nearly impossible to observe instantaneous localised density fluctuations in solutions. This lack of information results from the timescale and the length scales on which these processes occur. If these processes were more slow, imaging may be achievable, but microscopy is not yet able to detect some of these processes. There are theories describing how these processes occur, ranging from quantum mechanics for the electronic polarisation of molecules, to Newtonian mechanics for describing the motion of atoms and molecules. From these theories, models can be created; from these models, simulations can be run. Molecular dynamics simulations are an excellent tool for observing and describing crystallisation. Many simulations have been used to study the crystallisation of systems as varied as uncharged hard spheres [19] and partially charged water [20, 21]. It seems that this is the best method currently available to study the dynamics of a solution about to undergo NPLIN.

In the first part of this thesis, molecular dynamics simulations of systems that can undergo NPLIN are studied. In Chapter 3, the ion structures in supersaturated aqueous potassium chloride solutions are observed. Of particular interest is whether there exist long-lived amorphous ion clusters in solution. The existence of such clusters would corroborate the two-step nucleation theory necessary for the NPLIN mechanism proposed by Alexander and Camp. The creation and effects of nanobubbles in solutions are another mechanism by which NPLIN is thought to act. To this end, supersaturated aqueous sodium chloride solutions with a spherical carbon nano-impurity were modelled. The impurity was heated quickly to study whether this procedure can create nanobubbles, and whether the rapid heating of impurities has an effect on the structure of the solution or crystallisation. The results from these experiments are discussed in Chapter 4.

1.2 Ferrofluids and dipolar particles

Ferrofluids are stable suspensions of magnetic nanoparticles in a non-magnetic carrier liquid. These were patented in 1965 by Stephen Patell, of the National Aeronautics and Space Administration (NASA), who was trying to create a magnetic fluid to allow for the ejection of spent fuel from rocket engines in a zero-gravity environment [22]. They are usually comprised of ferromagnetic particles, composed of magnetic substances such as iron oxide, coated with surfactants and immersed in a carrier liquid, usually a hydrocarbon such as kerosene or paraffin [23–25]. The size of the ferromagnetic particles is in the nanometer scale, and their surfactant coating leads these particles to interact like dipolar hard spheres.

Though they are relatively new, ferrofluids have many promising features that make them useful for a wide variety of fields. Ferrofluids can be used as lubricating agents for hard drives [26] and other magnetic systems, or as heat dissipaters for the voice coils of loudspeakers [27]. In the medical field, ferrofluids can be used as contrast agents for MRI scanning [28–31], as a targeted drug-delivery mechanism [32], and, because ferrofluids can generate localised heating when placed in a rapidly oscillating magnetic field, techniques are being tested to see whether this localised heating can be used to kill tumorous cells in a less invasive and less risky way [33–38]. There is even speculation that ferromagnetic particles of high dipole strength could be used in the creation of artificial muscle [39]. It is possible to create a gel containing dipolar ferroparticles. If there is a strong external magnetic field as the gel sets, the magnetic dipoles of the particles will align with this field and will remain aligned once the gel is set. This gel would then have a different compression factor if compressed along the axis of the dipole moment than if compressed along a perpendicular axis. Furthermore, it may be able to alter its shape or mechanical properties in the presence of an external magnetic field. Lastly, ferrofluids have been used in various artistic projects [40].

For all medical uses of ferrofluids, and for hyperthermia particularly, it is important that the ferromagnetic particles are of similar size and dipole strength. Having a monodisperse ferrofluid results in all particles reacting to external magnetic fields to the same degree. This makes for a better contrast agent in MRI, easier delivery of drugs, and ensures that localised heating is as efficient as possible in hyperthermic treatments. Creating monodisperse systems of ferromagnetic particles remains extremely difficult. Figure 1.4 shows an example of the size distribution of ferromagnetic particles in a common ferrofluid [41]. Clearly, there

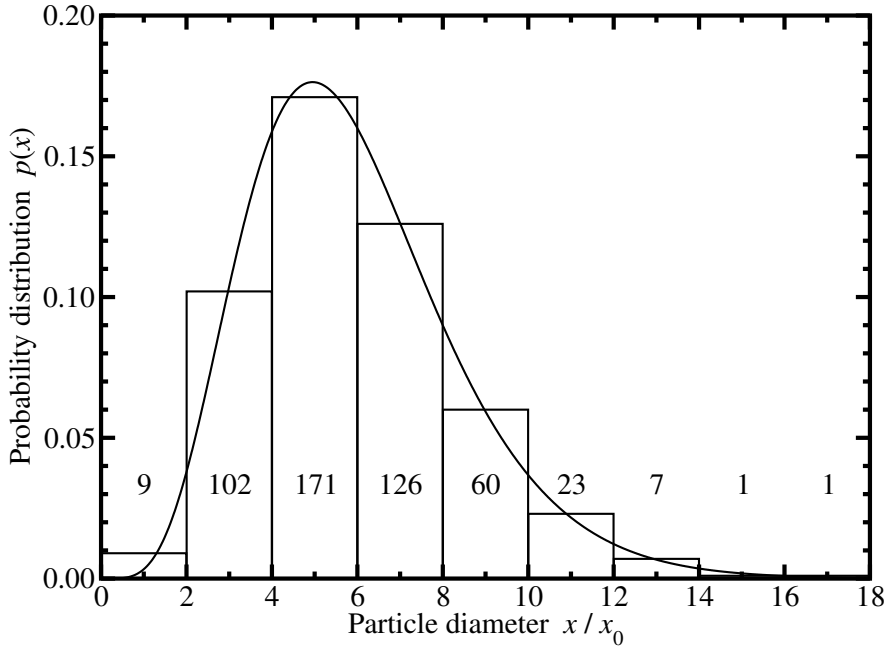

Figure 1.4: The polydispersity of particle diameter of experimentally achievable ferromagnetic particles in a ferrofluid. Figure reproduced from [41].

is large size distribution, and this is not a monodisperse system. A similar distribution can be expected for the magnetic dipole moments. Currently, research is being done to find new ways of controlling the particle-size dipole-moment distributions. One method being developed to control the particle-size distribution involves using magnetic bacteria to produce ferromagnetic particles [42, 43]. It is also possible to separate a polydisperse ferrofluid into monodisperse components by passing the ferrofluid through a constant magnetic field [44]. Neither of these techniques are able to produce a perfectly monodisperse system yet. Furthermore, neither of these techniques are cheap or able to produce monodisperse ferrofluid systems on an industrial scale yet.

Other uses of ferrofluids require the ferromagnetic particles to have large magnetic dipole moments. This is, again, a field in which experiment is only just developing the technologies needed to consistently create materials with the desired properties. Both theory and simulation have been used to look at the behaviour that arises from having a system of particles with large magnetic dipole moments (dipolar particles). There has been a long debate regarding whether such a system could undergo a vapour-liquid phase transition, started in 1970 when de Gennes and Pincus postulated that a dipolar fluid would condense similarly to a Lennard-Jones fluid (in the absence of a magnetic field) [46]. This was based on the fact that the leading-order, angle-averaged dipole-dipole interac-

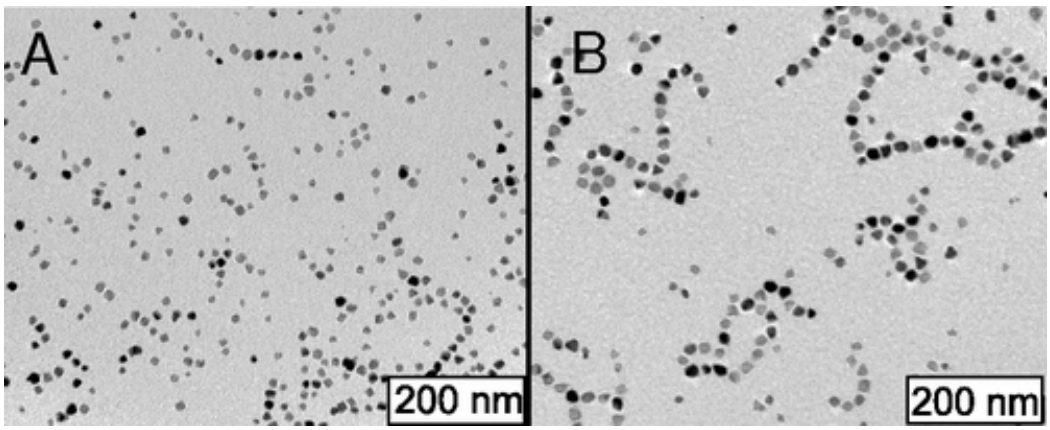

Figure 1.5: Cryogenic transmission electron microscope (TEM) images of experimentally produced ferrofluids. The ferromagnetic particles have a very large magnetic dipole moment, leading to chains of dipolar particles forming. Image reproduced from [45].

tion is proportional to the attractive van der Waals interaction between atoms and molecules. However, this statement came to be questioned when Weis and Levesque found that, when a low-density system of dipolar particles with large dipole moments were simulated, the dipolar particles form chains. The alignment of dipolar particles in a nose-to-tail parallel arrangement implies that the dipole-dipole interaction is not an isotropic attractive interaction like van der Waals attraction, and hence this brought into question whether dipolar particles could condense at all [47, 48]. Much further work has been done studying dipole particles in the chaining regime, but the vast majority of it has been done through theory or simulation. Only recently have ferrofluids been generated with particles of high enough dipole moments for chaining to be seen experimentally. Figure 1.5 shows cryogenic transmission electron microscope (TEM) images of dipolar particles in the chaining regime [45]. This is some of the first experimental evidence for chaining predicted theoretically.

The examples above illustrate the potential uses of ferrofluids in various different fields. However, it is clear that the experimental study of ferrofluids is very difficult. Theory and simulation have been able to guide experimental research into this field. They have been used to accurately predict many properties of ferrofluids, with these results being verified experimentally as ferrofluid technology improved. There are still many unanswered questions in this new field, and the use of theory and simulation is a cheap, efficient way of directing the paths that experimental research should take. Furthermore, as experiment has been improving drastically of late, theoretical and simulation results are quickly verified. For these reasons, ferrofluids are a particularly interesting set of systems to simulate.

Systems of dipolar particles are studied in the second part of this thesis. In Chapter 5, structures resulting from systems run using the long-ranged, pairwise, anisotropic, dipole-dipole potential are compared with those obtained from systems run using an equivalent short-ranged, isotropic, many-body potential. The short-ranged nature of the many-body potential greatly reduces computational costs, allowing for larger systems of dipolar particles to be run over longer time. In Chapter 6, the dynamic magnetic susceptibilities predicted by a new theory are tested against susceptibilities resulting from monodisperse systems of dipolar particles. The accurate prediction of the dynamic magnetic susceptibility is crucial in hyperthermia, and simulation provides a non-expensive method to study systems of interest.

Chapter 2

Methods

2.1 Introduction

Using computers to study atomic and molecular systems is a practice that has evolved quickly since its instigation in the mid–20^{th} century. This has resulted in a great number of techniques being developed, both to increase the speed at which certain phenomena can be simulated and to make the most efficient use of the computer power available when carrying out simulations. The recurring simulation and analysis methods used throughout this work are presented and explained in this chapter.

2.2 Molecular dynamics

Molecular dynamics (MD) simulation is a very powerful and conceptually easy method for modelling systems of interacting particles. It was first developed by Alder and Wainwright in 1957 [19, 49] and is, essentially, a brute-force method for estimating the solution to the many-body problem. The idea follows simply from Newtonian mechanics – for a system of particles with known interactions, if the positions and momenta of all particles are known at any given point in time, then it is possible to calculate the positions and momenta of all particles for all times preceding and following this point in time. An MD simulation is usually run as follows. The initial positions $\boldsymbol{r}^N(0)$ and velocities $\boldsymbol{v}^N(0)$ of all particles in the system are defined at the start of the simulation. A timestep δt is defined.

The potential energy is evaluated from the particle positions, and from this, the force and velocity of each particle is derived. The simulated system is brought forward by δt, with the motions of all particles in the system assumed to be at constant velocities from their initial positions $\boldsymbol{r}^N(0)$ to their new position $\boldsymbol{r}^N(\delta t)$. The potential energy and the force acting on each particle in its new position is calculated and the resulting velocity of each particle is derived. From this new position, all particles are assumed to move at a steady velocity to their next positions $\boldsymbol{r}^N(2\delta t)$, where the new potential energies and velocities will again be derived. This process is repeated *ad nauseam*.

Using MD simulations has certain advantages. From a computational point of view, as all particles are assumed to move at constant velocity during a timestep, the movement of one particle is independent of the movement of any other particle. This can be used to parallelise the process over multiple computer cores, resulting in faster calculations. Likewise, once the new particle positions are found following a timestep, the new potential energies and velocities can also be calculated in parallel. This leads to simulations of very large systems becoming possible to run in a reasonable timescale.

The main trick of MD is defining the timestep δt. It is important to choose a δt large enough to ensure that the process of interest occurs within a reasonable computational time, but also small enough so that no particle collisions can occur in one timestep. For molecular systems where all atoms are modelled, the timestep is usually of order 1–2 fs. This is an order of magnitude less than the fastest motion seen in atomistic systems, namely the rate of oscillation of a hydrogen atom in a hydrocarbon. Coarse-grained systems can be run with a larger timestep as the motion of the quickest components of the system are integrated out.

In this work, all MD simulations are carried out using the LAMMPS molecular simulation package [50]. The initial particle configurations are packed randomly using the Packmol software [51].

2.2.1 Verlet algorithm

A common algorithm to quickly move particles forward one timestep is the Verlet algorithm [52, 53]. This is used to update the positions of the individual particles in a system through time. It relates the position of a particle at a future time

$t + \delta t$ to its current position at time t and to the particle acceleration.

Consider the position $\boldsymbol{r}_i(t+\delta t)$ of particle i after time δt has elapsed. By a Taylor expansion about t, it is possible to show that

$$\boldsymbol{r}_i(t + \delta t) = \boldsymbol{r}_i(t) + \dot{\boldsymbol{r}}_i(t)\delta t + \frac{1}{2}\ddot{\boldsymbol{r}}_i(t)\delta t^2 + \boldsymbol{O}(\delta t^3) \tag{2.1}$$

where $\dot{A} = \mathrm{d}A/\mathrm{d}t$. Similarly, the position of particle i at the previous timestep $t - \delta t$ can be considered. The Taylor expansion of the particle position at time $t - \delta t$ about t gives

$$\boldsymbol{r}_i(t - \delta t) = \boldsymbol{r}_i(t) - \dot{\boldsymbol{r}}_i(t)\delta t + \frac{1}{2}\ddot{\boldsymbol{r}}_i(t)\delta t^2 - \boldsymbol{O}(\delta t^3). \tag{2.2}$$

As δt is very small, any terms of order δt^3 or higher can been assumed to be negligible. By considering $\boldsymbol{r}_i(t + \delta t) + \boldsymbol{r}_i(t - \delta t)$, it follows that the position of particle i after the timestep is

$$\boldsymbol{r}_i(t + \delta t) = 2\boldsymbol{r}_i(t) - \boldsymbol{r}_i(t - \delta t) + \frac{\delta t^2}{m_i}\boldsymbol{F}_i(t) \tag{2.3}$$

where $\boldsymbol{F}_i(t) = m_i\ddot{\boldsymbol{r}}_i(t)$ is the force acting on particle i at time t. A similar approach can be used to show that the velocity $\dot{\boldsymbol{r}}_i$ of particle i at time t is given by

$$\dot{\boldsymbol{r}}_{\boldsymbol{i}}(t) = \frac{1}{2\delta t}\left[\boldsymbol{r}_i(t + \delta t) - \boldsymbol{r}_i(t - \delta t)\right]. \tag{2.4}$$

Equations 2.3 and 2.4 are used to update particle position and velocity at all timesteps.

A similar algorithm is the velocity-Verlet algorithm. Rather than using the position before the previous move, the current position, the velocity, and force acting on each particle, the velocity-Verlet algorithm needs only the current particle position, velocity, and force. Consider the Taylor expansion of these three properties:

$$\boldsymbol{r}_i(t+\delta t) = \boldsymbol{r}_i(t) + \dot{\boldsymbol{r}}_i(t)\delta t + \frac{1}{2m_i}\boldsymbol{F}_i(t)\delta t^2 + \boldsymbol{O}(\delta t^3) \quad (2.5)$$

$$\dot{\boldsymbol{r}}_i(t+\delta t) = \dot{\boldsymbol{r}}_i(t) + \frac{1}{m_i}\boldsymbol{F}_i(t)\delta t + \frac{1}{2m_i}\dot{\boldsymbol{F}}_i(t)\delta t^2 + \boldsymbol{O}(\delta t^3) \quad (2.6)$$

$$\boldsymbol{F}_i(t+\delta t) = \boldsymbol{F}_i(t) + \dot{\boldsymbol{F}}_i(t)\delta t + \boldsymbol{O}(\delta t^2). \quad (2.7)$$

By substituting $\dot{\boldsymbol{F}}_i(t)$ from Eq. 2.7 into Eq. 2.6, the velocity $\dot{\boldsymbol{r}}_i(t+\delta t)$ can be written as

$$\dot{\boldsymbol{r}}_i(t+\delta t) = \dot{\boldsymbol{r}}_i(t) + \frac{\delta t}{2m_i}\left[\boldsymbol{F}_i(t) + \boldsymbol{F}_i(t+\delta t)\right] + \boldsymbol{O}(\delta t^3). \quad (2.8)$$

The velocity-Verlet algorithm propagates the system through time as follows. As before, the original positions $\boldsymbol{r}^N(0)$ and velocities $\dot{\boldsymbol{r}}^N(0)$ are defined, with the original forces $\boldsymbol{F}^N(0)$ evaluated from the particle positions. The particles are then moved to their new positions $\boldsymbol{r}^N(\delta t)$ *via* Eq. 2.5. The new forces $\boldsymbol{F}^N(\delta t)$ acting on all particles at time δt are evaluated, and the new velocities $\dot{\boldsymbol{r}}^N(\delta t)$ are found using Eq. 2.8. This process is repeated.

Both the Verlet and the velocity-Verlet algorithms have been shown to be very good at conserving energy over moves. In the Verlet algorithm, new particle positions are only dependent on prior or current positions and the force acting on them now. There is no need to calculate the velocity. Furthermore, the velocity is not dependent on the particle acceleration. The velocity-Verlet algorithm seems much more pragmatic, both in its approach to calculating new positions and velocities, and in its evaluation. As such, the velocity-Verlet algorithm is the one used to propagate all MD simulations discussed in this thesis.

2.3 The Monte Carlo method

The Monte Carlo method (MC) is another method for simulating molecular systems. It was originally developed in Los Alamos in 1947 by John von Neumann and Stanisław Ulam to predict the propagation of neutrons in nuclear fission [54, 55]. The first published article using the Monte Carlo method (MC) for molecular systems is the 1953 paper by Metropolis *et al.*, where systems of

particles interacting *via* the hard-sphere potential are studied [56]. In this paper, Metropolis *et al.* describe a simple method to allow a system to quickly reach thermal equilibrium.

The basic idea of MC is simple. Consider a system of particles with known positions and defined inter-particle interactions, known initial potential energy U_{I}, and known temperature T. One of these particles is chosen at random and displaced from its initial position to a new, randomly assigned position. The potential energy U_{F} of the system after this move is found. If the potential energy of the system after the move is less than the potential energy before the move ($U_{\mathrm{F}} < U_{\mathrm{I}}$), the move is accepted and the final configuration is taken as being the new initial configuration for subsequent move attempts. If the potential energy of the new configuration is greater than that of the initial configuration ($U_{\mathrm{F}} > U_{\mathrm{I}}$), the probability $P(U_{\mathrm{F}}|U_{\mathrm{I}})$ of the system making this jump in energy δU ($= U_{\mathrm{F}} - U_{\mathrm{I}}$) is found by using Boltzmanns law

$$P(U_{\mathrm{F}}|U_{\mathrm{I}}) = \exp\left(\frac{-\delta U}{k_{\mathrm{B}}T}\right). \tag{2.9}$$

A random number of value between zero and one is generated. If this random number is less than $P(U_{\mathrm{F}}|U_{\mathrm{I}})$, the move is accepted and the final position is taken as the new initial starting configuration for subsequent move attempts. Else, the system is brought back to the initial position and a new move is attempted from there. An increase in energy of 4.6 $k_{\mathrm{B}}T$ has a probability of occurrence of 1%. Therefore, energy jumps greater than this are highly unlikely to occur and will not occur repeatedly.

This method has many advantages. It is very quick, easy to implement, and can be easily altered for different ensembles. The 'move' can be defined as a translation move, a rotation move, a creation move (a particle is inserted into the system at a random position), an annihilation move (a particle is chosen at random and removed from the system), *et cetera*. As with all modelling techniques, though, there are drawbacks. It is very difficult for the system to escape local minima in energy. The choice of maximum move size is also important. If the attempted move results in a large distance being travelled by the particle, the acceptance probability will be very small and a lot of interesting features of the phase space will be overlooked. Conversely, if the attempted move is too small, only a small part of phase space will be studied. Finding the correct balance can be very tricky

and is usually achieved by adjusting the step size so that half of the attempted moves are accepted.

2.4 Interaction potentials

In both MD and MC simulations, it is necessary to define how molecules interact with each other. These interactions can be broken down in to two main categories: the intramolecular interactions of atoms within the same molecule, and the intermolecular interactions between atoms in separate molecules. The intramolecular interactions are greatly simplified and are represented by the stretching and twisting of bonds within a molecule. The intermolecular interactions are usually simplified as pairwise particle interactions comprising of a short-ranged part that imitates van der Waals interactions and a longer ranged electrostatic potential. All atoms undergo these intermolecular interactions with all other atoms in the system. These interactions are all briefly explained here.

2.4.1 Pair potential

The pair potential represents the van der Waals interaction between all particles. This acts over a short distance and must be repulsive when particles begin to overlap, and attractive at longer distances. Furthermore, it should tend to zero energy at large distances. The majority of the simulations here were run using the Lennard-Jones (LJ) '12-6' potential to simulate pair interactions. This potential has a strong repulsive term that dominates at very short distances but decays very quickly, and an attractive part that is much smaller than the repulsive part at short distances but decays more slowly. It is defined as

$$U_{\mathrm{LJ}}(r) = 4\epsilon \left[\left(\frac{\sigma}{r}\right)^{12} - \left(\frac{\sigma}{r}\right)^{6} \right] \tag{2.10}$$

where r is the distance between two particles, $-\epsilon$ represents the energy at the minimum point ($r_{\min} = 2^{1/6}\sigma$), and σ represents the particle diameter. Since this potential is analytic, it is easy to derive the force acting on a particle from another particle. Furthermore, as both attractive and repulsive parts decay quickly, it is possible to truncate this potential at distances greater than $2 - 3\sigma$ with

minimal effects on the simulation. To ensure that the potential curve remains continuous at the truncation distance, the curve can be shifted by the energy at the truncation distance. This is done by defining a cutoff distance r_c beyond which a particle cannot interact with another particle *via* this pair interaction. The shifting term allows the function to remain smooth and fully differentiable. This truncated/shifted potential is defined as

$$U_{\mathrm{TS}}(r) = \begin{cases} U_{\mathrm{LJ}}(r) - U_{\mathrm{LJ}}(r_c) & r \leq r_c \\ 0 & r > r_c. \end{cases} \tag{2.11}$$

Some of the results presented in this thesis were obtained using two different short-ranged pair potentials. The many-body approximation to the dipole interaction (Chapter 5) describes a system of particles interacting *via* the soft-sphere (SS) potential. This potential is the repulsive part of the LJ interaction only and is defined as

$$U_{\mathrm{SS}} = 4\epsilon \left(\frac{\sigma}{r}\right)^{12}. \tag{2.12}$$

Work on the susceptibility of ferrofluids (Chapter 6) was carried out using the Weeks-Chandler-Andersen (WCA) repulsive potential. This potential was developed in 1971 to study the effects of the attractive and repulsive parts of the LJ interaction on liquid structure [57]. The repulsive part of this potential is simply a truncated-shifted LJ curve with a cutoff $r_c = r_{\min}$. More simply, this potential is defined as

$$U_{\mathrm{WCA}}(r) = \begin{cases} U_{\mathrm{LJ}}(r) - U_{\mathrm{LJ}}(r_{\min}) & r \leq r_{\min} \\ 0 & r > r_{\min}. \end{cases} \tag{2.13}$$

These three short-ranged two-body potentials are plotted against one another in Fig. 2.1.

Lorentz-Berthelot mixing rules

LJ parameters ϵ and σ are usually defined to describe the interaction of two like particles. It is necessary to define rules for combining these interactions in systems

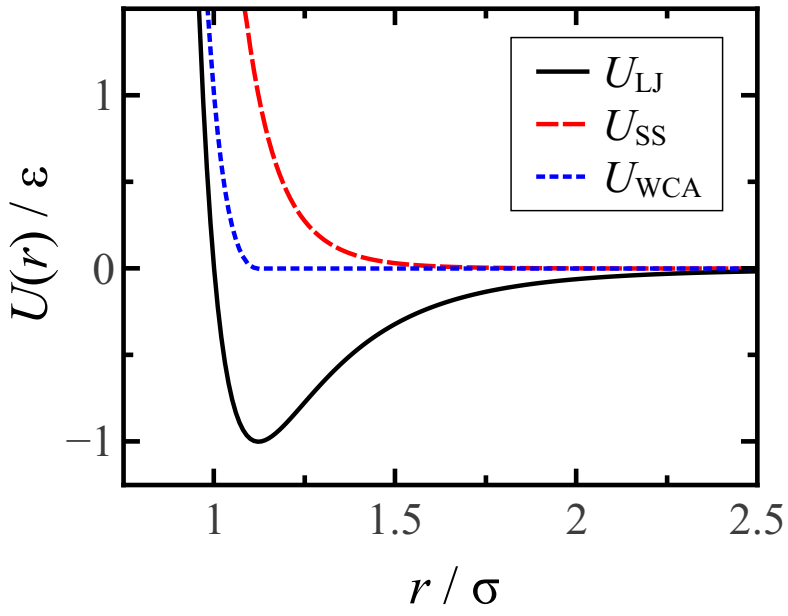

Figure 2.1: The different short-ranged two-body pair potentials used in this work. The two-body potentials shown are: the Lennard-Jones (LJ) potential (solid black line), the soft-sphere (SS) potential (dashed red line), and the Weeks-Chandler-Andersen (WCA) repulsive potential (dotted blue line).

with more than one type of particle. In this work, the Lorentz-Berthelot mixing rules are used where necessary. These are defined as follows. Consider a pair of particles i and j, where i has LJ parameters σ_{ii} and ϵ_{ii} and j has LJ parameters σ_{jj} and ϵ_{jj}. The LJ parameters σ_{ij} and ϵ_{ij} used when particle i interacts with particle j are defined as

$$\sigma_{ij} = \frac{1}{2}(\sigma_{ii} + \sigma_{jj}) \tag{2.14}$$

$$\epsilon_{ij} = \sqrt{\epsilon_{ii}\epsilon_{jj}}. \tag{2.15}$$

2.4.2 Electrostatic potential

Charged particles interact through the long-ranged Coulomb interaction. A pair of particles with charges q_i and q_j separated by a distance $r_{ij} = |\boldsymbol{r}_j - \boldsymbol{r}_i|$ has an electrostatic (ES) potential energy given by

$$U_{\mathrm{ES}}(r_{ij}) = \frac{1}{4\pi\varepsilon_0}\frac{q_i q_j}{r_{ij}} \tag{2.16}$$

where ε_0 is the vacuum dielectric permittivity. This potential decays as r^{-1} and therefore decays over a length equivalent to many simulation boxes. This can cause a problem when using periodic boundary conditions, but the problem is easily solved with the use of Ewald sums. Periodic boundary conditions are described in Section 2.6.2, and Ewald sums are explained in Section 2.6.3.

2.4.3 Dipole-dipole interactions

Some of the work presented in this thesis is focussed on systems composed of particles with dipole moments. The charge within these particles is polarised in such a way that these particles are no longer fully symmetric and can have an orientation. This charge distribution can be visualised as a vector arrow ($\rightarrow$) with one end of the arrow associated with the $\delta+$ charge and the other representing the $\delta-$ charge. The dipoles of these particles have a long-ranged interaction similar to the ES interaction. The long-ranged dipole-dipole interaction between particle i, with dipole moment $\boldsymbol{\mu}_i$, and particle j, with dipole moment $\boldsymbol{\mu}_j$, is

$$U_{\mathrm{DD}} = \frac{1}{4\pi\varepsilon_0}\left[\frac{(\boldsymbol{\mu}_i \cdot \boldsymbol{\mu}_j)}{r_{ij}^3} - \frac{3(\boldsymbol{\mu}_i \cdot \boldsymbol{r}_{ij})(\boldsymbol{\mu}_j \cdot \boldsymbol{r}_{ij})}{r_{ij}^5}\right] \tag{2.17}$$

where ε_0 is the dielectric permittivity of a vacuum.

This is an interesting potential as it favours the formation of chains. The lowest energy configuration for two and three dipolar particles is one where the the dipoles are aligned in a node-to-tail configuration ($\rightarrow\rightarrow$). When more particles are added, the preferred state of dipole particles is one where the dipole moments align in a head-to-tail ($\rightarrow\rightarrow$) configuration, with the lowest energy configuration being one where all dipoles form a ring.

2.4.4 Bond interaction potential

The bond interaction potential describes the energy resulting from one particle being chemically bound to another particle. This adds an extra energetic con-

straint on the movement of the bound particles, and makes it highly unlikely that the particles will be separated by a distance much greater than their equilibrium bond length r_0. In this work, bonds between molecules are represented as harmonic oscillators, with an equilibrium position r_0 and a spring stiffness k. The bond energy between two bound particles i and j is defined as

$$U_{\text{bond}}(r_{ij}) = k(r_{ij} - r_0)^2 \tag{2.18}$$

where $r_{ij} = |\boldsymbol{r}_{ij}|$ is the interparticle distance.

2.4.5 Angle interaction potential

The angle interaction potential describes the energy constraints of an angle bending in a simulation. In this work, this interaction is modelled as a harmonic spring. As before, if the equilibrium angle is given by θ_0 and the stiffness is given by k_θ, then the angle interaction potential is defined as

$$U_{\text{angle}}(\theta) = k_\theta(\theta - \theta_0)^2. \tag{2.19}$$

2.5 Ensembles

Molecular simulations describe microscopic motions of atoms and molecules over time. Effectively, only the particle positions (MC and MD), velocities (MD only), and interaction potentials are needed to derive macroscopic, experimentally-measurable mechanical properties such as pressure or density. At thermal equilibrium, these properties must be time-independent and can be found from the average value of the desired property over time. It is, however, imperative that certain thermodynamic values be kept fixed when studying the effect of varying other thermodynamic variables. The thermodynamic ensembles used when running both MD and MC simulations are described in this section.

In MD, the most simple ensemble to program is probably the microcanonical ensemble. In this ensemble, the number of particles in the system, the volume of the system, and the total energy of the system are kept constant (fixed NVE).

The system is effectively isolated from all external physical interference. Keeping the number of particles in the system constant is trivial; keeping the volume fixed is equivalent to defining the system box before the simulation is run and not allowing any fluctuation in box size; and the energy is kept as a result of the Newtonian equations of motion conserving energy.

The canonical ensemble models a system with a constant number of particles, a constant volume, and a constant temperature (fixed NVT). This models a system in thermal equilibrium with a heat bath. The number of particles and the volume are easily fixed. In MD the temperature is kept constant *via* the use of a thermostat, while in MC, the temperature is a pre-defined parameter. This is probably the most natural ensemble to use for MC calculations.

The isothermal-isobaric ensemble models a system at constant particle number, constant temperature, and constant pressure (fixed NPT) – as the name indicates. Here, the volume is allowed to fluctuate to ensure that the pressure and temperature are kept constant. As before, in MD the temperature is kept constant using a thermostat and the pressure is kept constant using a barostat. In MC, the temperature is a parameter and the pressure is kept constant by having additional volume moves that can be accepted and rejected. This ensemble is the most similar to normal experimental conditions, where pressure is much more easy to control than volume. The barostats and thermostats used are described in Section 2.5.1.

The grand canonical ensemble models a system in a heat and particle bath. The chemical potential, volume, and temperature of the system are kept constant (fixed μVT). This models an open system, where the total number of particles in the system varies with time. This ensemble is used to find the liquid-vapour coexistence point in Chapter 5. Similarly, the isenthalpic-isobaric ensemble is used in Chapter 4. This ensemble is run at constant particle number, constant pressure, and constant enthalpy (fixed NPH).

2.5.1 Nosé-Hoover thermostat and barostat

Certain ensembles discussed above need either a fixed pressure or temperature (or both in the case of the isothermic-isobaric ensemble). In MD simulations, the temperature is kept fixed through the use of the Nosé-Hoover thermostat or the Langevin thermostat, and pressure is kept constant *via* the Nosé-Hoover barostat.

A system modelled at constant temperature is considered to be in contact with a heat bath. The Nosé-Hoover thermostat works by adding a degree of freedom to represent this heat bath. This enables the flow of energy from the heat bath to the system and vice versa. The speed of heat transfer can be adjusted by increasing or decreasing the 'mass' of this degree of freedom in the system [58,59]. In Chapters 5 and 6, the Langevin thermostat is used. This thermostat models the particles in the system as being immersed in an implicit solvent at the desired temperature. The use of an implicit solvent results in the particles feeling a frictional drag proportional to their velocities, and undergoing random Brownian collisions with the solvent atoms. The Brownian collisions will result in cold particles gaining thermal energy, and the drag force will reduce the speed of hot particles, thereby ensuring that the system temperature equilibrates at the desired value [58,59].

Similarly, the pressure is kept constant by adding degrees of freedom that are coupled to the simulation cell dimensions that allow the cell to increase or decrease in volume, resulting in the instantaneous pressure decreasing or increasing. This results in the barostat acting as a piston on the system. The speed at which the volume can fluctuate is governed by defining the 'friction' that the piston feels [58,59].

2.6 Common simulation techniques

2.6.1 Reduced Lennard-Jones units

Most simulations are of very small systems. The average fluctuation in thermal energy is of the order of $k_{\mathrm{B}}T$, masses are measured in atomic mass units, charges are multiples of the elementary charge, and time is measured in femtoseconds. Converting these units to SI units is both time and memory consuming. A set of units has been devised to keep these values more manageable. The LJ length σ is taken as being the unit of length, and the LJ energy ϵ is taken as the unit of energy. This means that the LJ equation [Eq. 2.10] can be re-written as $U^*_{\mathrm{LJ}} = U_{\mathrm{LJ}}/\epsilon$. Below is a list showing different thermodynamic properties in their reduced form [58].

Length	$L^* = L/\sigma$
Energy	$T^* = k_\mathrm{B}T/\epsilon$
Number density	$\rho^* = N\sigma^3/V$
Pressure	$P^* = P\sigma^3/\epsilon$
Time	$t^* = t\sqrt{\epsilon/m\sigma^2}$
Force	$f^* = f\sigma/\epsilon$
Dipole moment	$\boldsymbol{\mu}^* = \boldsymbol{\mu}/\sqrt{4\pi\varepsilon_0\sigma^3\epsilon}$

2.6.2 Periodic boundary conditions

Boundary effects can be problematic in simulations. When simulating effects in a bulk fluid, it is important to consider that, unless something is done, the particles at the edge of a simulation box will be in a different condition to those in the centre of the box. The edge of the box acts as a boundary for the particles being simulated. The easiest method to work around this problem is to use periodic boundary conditions (PBCs). The simulation is prepared as a cubic cell with a certain number of particles. This cell is then replicated periodically in space to form an infinite lattice as shown in Fig. 2.2. When a particle leaves the simulation cell through one of the boundaries, an image of this particle will enter the cell at equal velocity from the opposite boundary. PBCs are useful in determining the potential energy of a single particle in the simulation box. It is possible to use PBCs to consider interactions between a particle and the periodic images of other particles but, as there are effectively an infinite number of periodic images, this drastically increases the number of calculations required. Instead, for short-ranged potentials, only interactions between particles and the closest image (original or otherwise) of other particles are taken into account. This effectively re-centres the simulation box about the particle of interest and considers only interactions with the images of other particles that fall inside this shifted box. This method is called the minimum image convention [58, 59].

There are some problems with the use of PBCs, the most obvious being finite-size effects. The use of PBCs allows for simulations of systems equivalent to experimental samples in the bulk. The way this is achieved can lead to certain complications. If the initial simulation cell is too small, it is possible for a particle to interact with its periodic image. As the motion of a particle and its images are coupled, this can have a stabilising influence on certain processes such as phase transitions or crystal formation. This can lead to 'strange' results, such as systems crystallising at lower concentrations when run in smaller simulation cells [60]. Another interesting problem that can arise results from dissipation

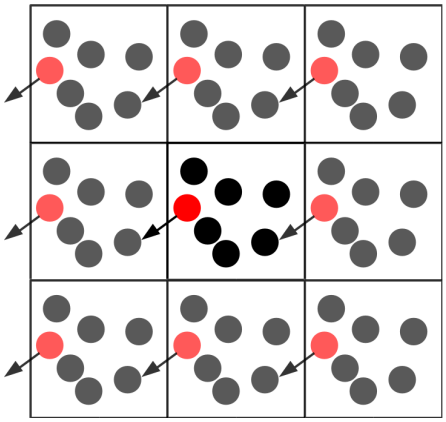

Figure 2.2: Illustration of PBC. The central simulation cell is periodically reproduced, and the positions of all atoms within it are recreated periodically. When the red particle exits the central box through the left side, an image of it re-enters the box *via* the right side.

effects. Given enough time, a particle at the origin of a shock wave in the system will eventually be acted on by the shock wave propagated from its images. This can lead to self-propagation problems. These examples highlight the fact that PBCs must be used carefully.

2.6.3 Ewald sums

As discussed previously, the pairwise ES interaction is long-ranged. It decays slowly to zero and the use of a cutoff can greatly alter the total ES energy acting on a particle. However, due to the long-ranged nature of the ES force, the lack of a cutoff results in numerous calculations, involving many periodic cell images, needing to be carried out. The total ES energy of a system run using PBCs is

$$U_{\mathrm{ES}} = \frac{1}{4\pi\varepsilon_0}\left[\sum_{i>j}^{N}\frac{q_i q_j}{|\boldsymbol{r}_{ij}|} + \sum_{\mathbf{n}\neq\mathbf{0}}^{\infty}\sum_{i\geq j}^{N}\frac{q_i q_j}{|r_{ij}+\mathbf{n}L|}\right] \tag{2.20}$$

where q_{i} is the charge on particle i, $r_{ij} = |\boldsymbol{r}_j - \boldsymbol{r}_i|$ is the vector distance between particles i and j, L is the box length, and $\boldsymbol{n} \in \mathbb{Z}^3$; $\boldsymbol{n} \neq \mathbf{0}$ is a cubic lattice vector used to represent the infinite periodic images of the simulation cell.

Evaluating Eq. 2.20 is often very computationally expensive and there are many problems with simply using a spatial cutoff to evaluate a charge-dependent potential, including the possibility that the charges within the cutoff do not cancel out.

The Ewald sum allows for a calculation of the ES potential and force efficiently and without these problems occurring. Below is a description of the principles behind Ewald sums.

Consider the central simulation cell. It is charge-neutral. Likewise, any shifted image of this central cell, with any particle as the centre, is also charge-neutral. Therefore all particles can be seen as the centre of a charge neutral cell with the same dimensions as the simulation box. One can consider that each point charge is surrounded by a charge distribution of opposite charge but of equal magnitude, acting as a screen. This distribution can be approximated as a Gaussian curve defined as

$$\rho_{i,z}(r) = \frac{z_i \kappa^3}{\pi^{3/2}} \exp(-\kappa^2 r^2) \tag{2.21}$$

where κ is an arbitrary parameter used to determine the width of the Gaussian. The addition of this screening potential acts like an ionic cloud and makes it possible to treat the screened interactions as purely short-ranged.

The addition of this screening potential results in the total charge distribution of the system being altered. This is countered by creating a potential of the same magnitude but opposite sign to the screening potential, thereby cancelling it. This cancelling potential effectively allows for the interaction to be split into two components: the first component being comprised of the original point-charge and the associated screening potential, the second comprising only of the cancelling potential.

For each charge, there will be one screening potential and one associated cancelling potential. By construction, the first of these components falls to zero at distances smaller than the size of the simulation box for all particles, leaving only the cancelling functions. The cancelling functions are long-ranged and must still be evaluated for large distances. However, as all of these functions are now smooth, it is possible to solve these interactions in reciprocal space. A Fourier transform of the cancelling distribution for each particle is calculated. All of these reciprocal-space cancelling distributions are summed, with the total being reconverted to real space and added to the original screened charge potential. In doing this, however, the charge of the original particle associated with the cancelling function is counted twice: once in the screened interaction and once in the long-ranged cancelling interaction. It is necessary to remove this self-interaction.

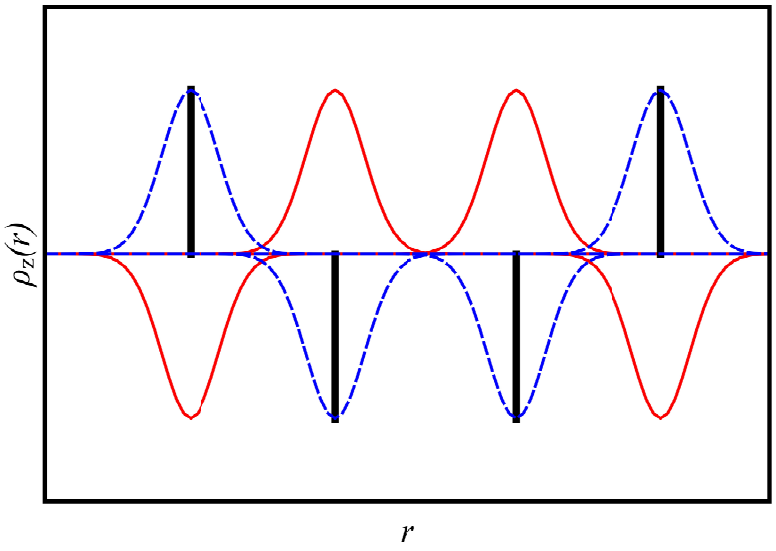

Figure 2.3: Charge screening and cancelling functions used in Ewald sums. The physical particle charges (full black peaks), screening potential [Eq. 2.21] (full red line), and the cancelling distributions (dashed blue line) are shown for a one-dimensional system.

The ES potential over PBCs can be rewritten as

$$U_{\mathrm{ES}} = U_{\mathrm{screened}} + U_{\mathrm{cancelling}} - U_{\mathrm{self}} \tag{2.22}$$

where:

$$U_{\mathrm{screened}} = \sum_{i>j} q_i q_j \frac{\mathrm{erfc}(\kappa|\boldsymbol{r}_{ij}|)}{|\boldsymbol{r}_{ij}|} + \sum_{i\geq j}\sum_{\boldsymbol{n}\neq\boldsymbol{0}} q_i q_j \frac{\mathrm{erfc}(\kappa|\boldsymbol{r}_{ij}+\boldsymbol{n}L|)}{|\boldsymbol{r}_{ij}+\boldsymbol{n}L|} \tag{2.23}$$

$$U_{\mathrm{cancelling}} = \frac{1}{L^3}\sum_{\boldsymbol{k}\neq\boldsymbol{0}} \frac{4\pi}{k^2} \exp\left(\frac{-k^2}{4\kappa^2}\right) \sum_{i>j} q_i q_j \exp\left(-i\boldsymbol{k}\cdot\boldsymbol{r}_{ij}\right) \tag{2.24}$$

$$U_{\mathrm{self}} = -\frac{\kappa}{\sqrt{\pi}}\sum_i q_i^2. \tag{2.25}$$

The function $\mathrm{erfc}(x) = 2\pi^{-1/2}\int_x^\infty \exp(-t^2)\mathrm{d}t$ is the complementary error function, and $\boldsymbol{k}$ are wavevectors given by $\boldsymbol{k} = \frac{2\pi}{L}(n_x, n_y, n_z)$ for $n_z, n_y, n_z \in \mathbb{Z}$. This function drops to zero as x is increased. It follows that the greater the value of κ, the more quickly Eq. 2.23 will tend to zero. Therefore, it is possible to choose

κ such that only the first part of Eq. 2.23, corresponding to $\boldsymbol{n} = \mathbf{0}$, is significant. This is equivalent to assuming that the charged particles are fully screened within the shifted simulation box of which they are the centre.

The cancelling potential, given in Eq. 2.24, is evaluated in reciprocal space. Though this function decays to zero much more quickly over reciprocal space than the original ES function over real space, it is still necessary to define a cut-off wavevector above which this interaction is no longer evaluated. In the work discussed here, the cutoff is defined in terms of the contribution that an image has to the ES contribution to the force acting on each particle. A reference force is defined as the force exerted by two unit point charges at a distance of 1 Å from one another. The force per particle is found at all wavevectors for which the RMS error in the force is less than $1/10000^{\text{th}}$ of this reference force [50]. This cutoff describes the number of shifted periodic cells that should be included in the Ewald sum. As each shifted cell is charge-neutral, a cutoff can be used without risking a pseudo-charge being calculated.

A result of truncating the long-ranged summation is that the system is now finite. As such, the effects that the system boundary has on the ES interaction need to be determined. Usually, it is assumed that, past the ES cutoff, there is a uniform medium with a given permittivity [58, 59]. For Ewald sums, it is common to assume that this medium is a perfect conductor ($\varepsilon_s = \infty$). However, as MD simulations are usually assumed to run in a vacuum ($\varepsilon_s = 1$), it is important to alter the contribution from the medium from being that of a vacuum to that of a perfect conductor. The contribution to the total ES energy of a perfect conductor can be linked to that of a vacuum [58, 59] by

$$U_{\text{medium}}(\varepsilon_s = \infty) = U_{\text{medium}}(\varepsilon_s = 1) - \frac{2\pi}{3L^3}\left|\sum_{\text{i}} z_{\text{i}}\boldsymbol{r}_{\text{i}}\right|^2 . \tag{2.26}$$

Therefore, the final contribution to the Ewald sums is the contribution of the medium surrounding the outermost periodic images taken into account. For a vacuum, this contribution is

$$U_{\text{medium}}(\varepsilon_s = 1) = \frac{2\pi}{3L^3}\left|\sum_{\text{i}} z_{\text{i}}\boldsymbol{r}_{\text{i}}\right|^2 \tag{2.27}$$

and for a perfect conductor, this is $U_{\text{medium}}(\varepsilon_s = \infty) = 0$.

Particle-particle particle-mesh

Though the Ewald sums method is a considerable speed boost when compared to numerically solving Eq. 2.20, there are methods to speed up the calculation further. The most obvious of these would be to use fast Fourier transforms (FFTs) when calculating the long-ranged cancelling potentials [Eq. 2.24]. In fact, it is possible to speed up this step more by first approximating the charges of the system onto a mesh. As the distance between the points of the mesh tends to zero, the representation tends towards an exact description of the simulation box. The use of such a mesh makes it more straightforward and faster to calculate the Fourier transforms and, therefore, increases the speed of calculation for the long-ranged contributions to the potential energy. This is, in turn, further sped up by use of FFTs. Lastly, it is possible to approximate the field at each mesh point by differentiating the potential. This can then be used to calculate the ES force felt by each particle in the system. This method is the particle-particle particle-mesh (PPPM) method.

2.6.4 Neighbour list

Current simulations usually model systems containing between 10^3 and 10^7 particles. The use of a cutoff distance r_{c} in determining the short-ranged pair potential acting on a particle usually means that the vast majority of the system will have no contribution to the short-ranged potential energy of this particle. However, the computationally expensive part of the short-ranged energy calculation is the calculation of the distance r_{ij} separating two particles. A lot of computational power can be spent calculating distances between particles separated by a large distance and that will have no contribution to the short-ranged energy of a particle. One method of speeding this up is to use a neighbour list. Every few timesteps, a list of all particles that fall within the neighbour cutoff $r_{\text{neigh}} > r_{\text{c}}$ is compiled for each particle. The short-ranged interactions are then only calculated between a particle and the particles in its neighbour list.

As with all techniques, it is important to be careful when using a neighbour list. Firstly, it is important to choose r_{neigh} large enough to ensure that particles

outside of the list are not able to move to a position where they would contribute to the particle energy before the neighbour list is rebuilt. A corollary to this is that the period of time between builds must be small enough to prevent this same effect. It is also important that both of these properties are large enough to ensure that there is a time gain in using the neighbour list method. Clearly, not much time is saved calculating a neighbour list if this needs to be updated every timestep.

2.7 Common analysis methods

Some methods for analysing results occur recurrently throughout this thesis. The three most used methods are the autocorrelation functions, radial distribution functions, and the structure factors. Here, these methods are briefly explained along with a quick discussion regarding errors and uncertainties.

2.7.1 Autocorrelation functions

An autocorrelation function describes how quickly a system 'forgets' a property. Suppose that a vector has a value $\boldsymbol{a}(t)$ at time t. The time autocorrelation function $ACF(t)$ at time t is defined as

$$ACF(t) = \langle \boldsymbol{a}(t) \cdot \boldsymbol{a}(0) \rangle. \tag{2.28}$$

The integral of a normalized autocorrelation function gives the average time that it takes for the system to completely forget its original orientation. This time τ is defined as

$$\tau = \int_0^\infty \frac{\langle \boldsymbol{a}(t) \cdot \boldsymbol{a}(0) \rangle}{\langle \boldsymbol{a}(0) \cdot \boldsymbol{a}(0) \rangle} dt. \tag{2.29}$$

Furthermore, some transport coefficients can be derived exactly from autocorrelation functions [58, 59, 61]. These properties are said to obey a Green-Kubo relation. A common example of this is the velocity autocorrelation function, whose integral is directly proportional to the diffusion constant of a system.

2.7.2 Radial distribution function

Consider a particle pair function $n(r)$ that measures the average number of particles whose centre of mass is found within a distance interval $[r, r + \delta r]$ from the centre of mass of any particle. The integral of this function over all space should give the total number of particles in the system. It is possible to find the average number density $\rho(r)$ at a distance r from a particle by dividing $n(r)$ by the volume of the bin of width δr. The radial distribution function (RDF) is the probability of finding a local number density $\rho(r)$ at distance r relative to the probability of finding an equivalently spaced pair at uniform distribution ρ_{ave}. It is defined mathematically as

$$g(r) = \frac{n(r)}{\frac{4\pi}{3}[(r + \delta r)^3 - r^3]\rho_{\text{ave}}}. \tag{2.30}$$

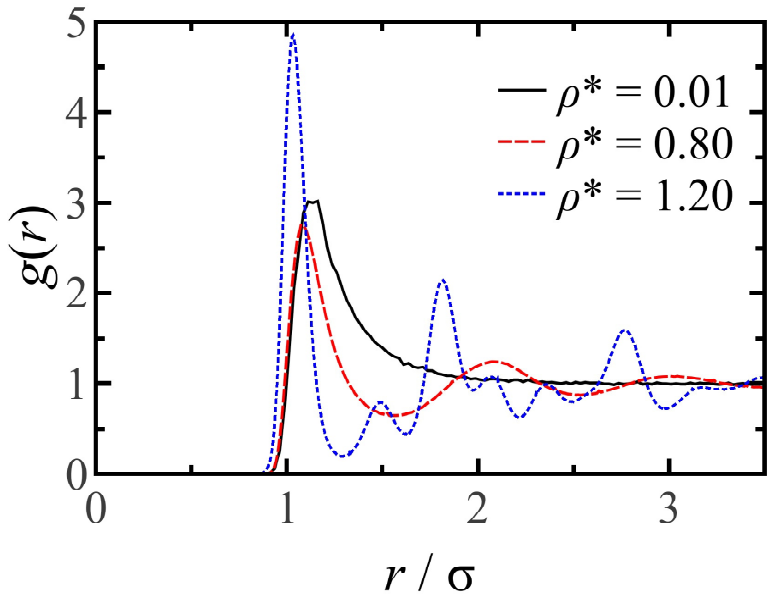

Figure 2.4: RDFs of systems of LJ spheres at temperature $T^* = 1.0$ for a range of densities. $\rho^* = 0.01$ (full, black line) shows the RDF of a system in the gas phase; $\rho^* = 0.80$ (red dashed line) shows the RDF of a system in the liquid phase; and, $\rho^* = 1.20$ (blue dotted line) shows the RDF of a system in the solid phase.

Figure 2.4 shows the RDFs of systems of LJ spheres in the gas phase ($\rho* = 0.01$), liquid phase ($\rho* = 0.80$), and solid phase ($\rho* = 1.20$). Typically, the RDF in a system in gas phase will have a peak, followed by an exponential decay tending to $g(r) = 1$. A system in the liquid state exhibits an RDF that has a peak, followed by oscillations of decreasing intensity about $g(r) = 1$. The RDF of a system in

the solid phase has repeated high peaks and troughs that are very close to zero. In general, more ordered systems will have higher first peaks, first troughs that are closer to zero, and more evident repeating patterns than less ordered systems.

2.7.3 Structure factor

The structure factor $S(k)$ describes the intensity at which particles (photons or neutrons) of wavevector $\boldsymbol{k}$ are diffracted by elastic scattering in the system being studied. Consider the spatial Fourier transform of the number density

$$\rho(\boldsymbol{k}) = \int_{-\infty}^{\infty} d\boldsymbol{r} \exp(i\boldsymbol{k}\cdot\boldsymbol{r}) \sum_{j=1}^{N} \delta(\boldsymbol{r}-\boldsymbol{r}_j) \tag{2.31}$$

$$= \sum_{j=1}^{N} \exp(i\boldsymbol{k}\cdot\boldsymbol{r}_j) \tag{2.32}$$

where N is the total number of particles in the system, $\boldsymbol{r}_j$ is the position of particle j, and $\delta(x)$ is the Dirac delta function. The structure factor is then defined as

$$S(k) = \frac{1}{N}\langle\rho(k)\rho(-k)\rangle \tag{2.33}$$

where k represents all vectors of equal magnitude $|\boldsymbol{k}| = k$.

Figure 2.5 shows the structure factors of LJ systems in different phases at temperature $T^* = 1.0$. A gaseous system ($\rho^* = 0.01$) exhibits a structure factor that fluctuates mildly about one. A system in its liquid phase ($\rho^* = 0.80$) produces a structure factor with a peak at $k \simeq \frac{2\pi}{\sigma}$, followed by fluctuations about $S(k) = 1$. The structure factor of a system in its solid state ($\rho^* = 1.20$) shows sharp Bragg peaks at certain wavevectors k corresponding to distances where there is a repeating pattern in the solid lattice, and is at $S(k) = 0$ otherwise.

The structure factor of a system is proportional to the Fourier transform of the RDF of the system. In fact, the structure factor is equivalent to

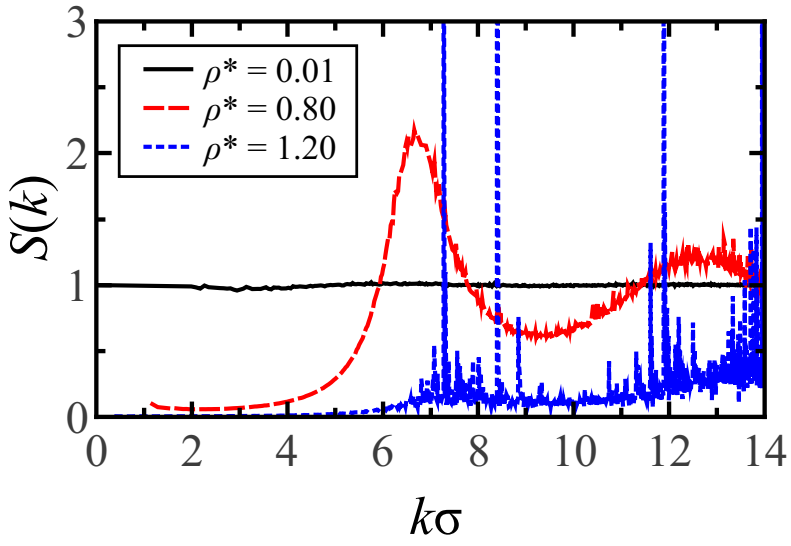

Figure 2.5: Structure factors of systems of LJ spheres at temperature $T^* = 1.0$ for a range of densities. $\rho^* = 0.01$ (full, black line) shows the structure factor of a system in the gas phase; $\rho^* = 0.80$ (red dashed line) shows the structure factor of a system in the liquid phase; and, $\rho^* = 1.20$ (blue dotted line) shows the structure factor of a system in the solid phase.

$$S(k) = 1 + 4\pi\rho \int_0^\infty r^2 \frac{\sin(kr)}{kr}[g(r) - 1]dr \tag{2.34}$$

where $g(r)$ is the RDF of the system and ρ is the average density of the system [58]. The structure factor can be determined experimentally *via* x-ray or neutron scattering. It therefore provides a useful means of directly comparing experimental and simulation results.

2.7.4 Errors and uncertainties

The results presented in this thesis are always averaged over a large number of simulation time frames. Furthermore, the frames are output with time delays such that they represent the system at statistically independent states. These conditions result in the calculated standard error being minuscule. The errors are often much smaller than the size of the points representing them and, as such, error bars are not shown. Where possible, relevant results from experiment are also given for comparison. This is probably a better illustration of the validity of the simulation results than the calculated standard error of the mean.

Chapter 3

Studying clustering and dynamics in aqueous potassium chloride solutions

3.1 Introduction

This chapter will give a detailed analysis of a series of simulations run to better understand the metastable structure and dynamics in supersaturated potassium chloride solutions. This work was carried out to try to understand the state of a solution up to and above the saturation concentration and to try to understand what a pre-critical crystal nucleus is and how it forms. Ultimately, this work is focused on structures that exist for a lifetime of the order of 1 ns to better understand the processes occurring in non-photochemical laser-induced nucleation.

Forming a crystal from a supersaturated aqueous solution is experimentally easy to do. Books teaching children how to grow their own crystals are readily available [62]. The general method described in these books is to add salt to water until no more salt will dissolve (and saturation is reached) before allowing evaporation to bring the system to supersaturation. Eventually, crystals will begin to form. The basic concepts of this experiment are used in many industries. It is therefore surprising that very little is known about the processes happening in the period of time between supersaturation being reached and crystallisation beginning. Some supersaturated solutions crystallise spontaneously, while others remain metastable for years. It is very difficult to observe minute changes in the

structure of metastable supersaturated solutions experimentally. Furthermore, as crystallisation is a stochastic process, it is nearly always impossible to define or predict the exact time and place that a crystal first appears in a supersaturated solution [20, 63–67].

Recent experimental developments have resulted in a technique that appears to allow for the creation of crystals 'on demand'. In 1996, Garetz and coworkers demonstrated that it is possible to induce crystallisation in supersaturated aqueous urea solutions by using a low-power near-infrared laser pulse of 20 ns duration passed through the system [1]. The process is not photochemical and is referred to as non-photochemical laser-induced nucleation (NPLIN). Garetz and coworkers continued developing this method and found that other systems also underwent NPLIN. Probably most interesting of these was glycine, which was found not only to undergo NPLIN but to also crystallise in a different form depending on the polarization of the laser beam: plane-polarized lasers induce the crystallisation of $\gamma-$polymorph glycine, whereas circular polarised laser beams induce the crystallisation of the $\alpha-$polymorph [2–4].

The ideas and uses of NPLIN have been greatly advanced in recent years by other groups. For instance, Alexander and coworkers have shown that NPLIN can induce the nucleation of supercooled glacial acetic acid [10], carbon dioxide in carbonated liquids (including champagne) [11], and of various simple aqueous salt solutions [7–9, 68]. Recent work has also demonstrated that the laser-pulse duration plays an important role in the process of NPLIN. Ward *et al.* have shown that a single laser pulse of duration less than 5 ps would not induce nucleation in carbonated drinks, whereas a pulse of duration greater than 100 ps would consistently induce nucleation [11]. This strongly suggests that there is some long-lived structure present in the solution on which the laser pulse acts to enhance the probability of nucleation occurring.

NPLIN of aqueous potassium chloride is of particular interest from a theoretical and computational point of view. A theory based on the idea that nucleation is induced by electronic polarisation of the ions by the electric field of the laser light has been developed and predicts the rates of NPLIN nucleation in these aqueous alkali-halide systems quite well [7]. Furthermore, the supersaturated solutions used in these experiments are metastable. Alexander and Camp report that supersaturated aqueous potassium chloride solutions can remain in a non-crystallised state for months [7].

Metastability makes aqueous potassium chloride the perfect system to use to investigate structure and dynamics prior to crystallisation. Aqueous ionic salt solutions have been studied in great depth using atomistic computational methods [69–81]. Most of this work has been carried out modelling sodium chloride or has been carried out modelling a variety of salts at low concentrations (with respect to saturation concentration). Some computational work has been carried out at high concentration, but as this has mainly been to look at the processes of homogeneous nucleation, these do not address the pre-crystallisation structure in great depth [73, 77, 78, 80].

Furthermore, while there are little simulation data on aqueous potassium chloride at near-saturation concentrations, experimental data is readily available. It is therefore possible to use this system to validate simulation forcefield parameters against experimental results. It will also be interesting to see the effect that different water models will have on the sub-saturation properties of this system. It has been shown that the four-site TIP4P water model reproduces the water phase diagram much more accurately than the three-site TIP3P water model [82–85], and it is generally acknowledged that TIP4P describes the liquid phase of water more accurately than does TIP3P. However, as some of the ion forcefield parameters that will be tested have been developed for use in TIP3P water [86], it is important to determine which of these water models will produce more accurate dynamics.

This chapter is divided as follows. First, the simulation models and methods used will be detailed. Results comparing the sub-saturation properties of each simulation model with experimental data will be presented, followed by a study of the solution structure at supersaturated concentrations. Finally, the existence of short-lived amorphous salt clusters of equivalent lifetime to an NPLIN laser pulse duration will be demonstrated before concluding with some brief remarks on the effects of water in these clusters.

3.2 Simulation details

The choice of model for this set of simulations is important. The model used must be able to reproduce certain key features seen in experiments. First among these is the criterion that the system must not crystallise when supersaturated to 'reasonable' levels. It has been reported that supersaturated aqueous potas-

sium chloride solutions can be kept in their metastable state for months without crystallising [7, 8]. It is therefore highly improbable that any long-lived crystal structures will form in the simulation timescale. Therefore, there should be no evident crystal formation at any concentration simulated, both above and below saturation. Furthermore, it is important for the model system to accurately reproduce certain static and dynamic properties measured experimentally. These properties include the mass densities, ion self-diffusion coefficients, and conductivities at concentrations up to saturation. Keeping the simulation density close to the experimental density will mean that the system remains of a realistic size and calculating the dynamic parameters (ionic self-diffusion and conductivity) will give an insight into the influence of ion association. It follows that keeping the simulation values of these dynamic parameters close to experimental values measured in equivalent systems will imply that the simulated ion association is close to the real ion association. It is very difficult to find reliable experimental values for these properties above saturation. Therefore, these parameters were studied for conditions up to experimental saturation concentration. While supersaturated structure and crystallisation has been studied in great depth for other ionic salt systems (*e.g.* NaCl), very little work has been done studying the properties of aqueous potassium chloride as the salt concentration nears experimental saturation, and most of the work reported in literature studies simulated solutions of low salt concentration.

Water was modelled using the SPC/E model [87], the TIP3P-Ewald model [88], and the TIP4P-Ewald model [89]. These are three common water models that have been optimised for use with the particle-mesh Ewald summation method. These models assume that water molecules are kept rigid, and that the bonds and angles cannot fluctuate from their equilibrium positions. K^+ and Cl^- ions were simulated using the parameters developed by Dang [86]. Joung and Cheatham have also parametrised ion potentials to closely match experimental solubility. They find that certain water models run with Dang parameters grossly underestimate the saturation molality of aqueous potassium chloride, with the simulation solubility calculated as being 0.49 mol kg^{-1} when run in TIP3P water and 0.53 mol kg^{-1} in SPC/E water, both much lower than the experimentally calculated 4.77 mol kg^{-1} [90, 91]. Therefore, one more model, comprising TIP4P-Ew water with ion parameters parametrised for TIP4P by Joung and Cheatham (JC), was used in this comparison to ensure that the effects of an experimentally accurate solubility (3.99 mol kg^{-1}) were taken into account. Since, work by Benavides and coworkers has shown that the methods used by Joung and Cheatham to determine

system solubilities greatly overestimates the accuracy of the solubility determined for their forcefield [92]. For brevity, these models shall now be referred to as the SPC/E+Dang, TIP3P-Ew+Dang, TIP4P-Ew+Dang, and TIP4P-Ew+JC models.

Atoms are modelled as charged Lennard-Jones (LJ) particles, with interactions calculated using the LJ equation and a Coulombic term:

$$U_{\mathrm{LJ}}(r_{ij}) = 4\epsilon \left[\left(\frac{\sigma}{r_{ij}} \right)^{12} - \left(\frac{\sigma}{r_{ij}} \right)^{6} \right] + \frac{q_i q_j}{4\pi\varepsilon_0 r_{ij}} \tag{3.1}$$

where q_i is the charge on particle i, r_{ij} is the distance between particles i and j, ε_0 is the electric vacuum permittivity, and the LJ parameters ϵ_{ii} and σ_{ii} are given for each species in Table 3.1. The cross LJ parameters are found using the Lorentz-Berthelot mixing rules given in Eqs. 2.14 and 2.15.

	q_i (e)	σ_{ii} (Å)	ϵ_{ii}(kcal mol^{-1})
SPC/E Water [87]			
O	−0.8476	3.166	0.1553
H	+0.4238	0.0	0.0
TIP3P-Ewald Water [88]			
O	−0.830	3.188	0.102
H	+0.415	0.0	0.0
TIP4P-Ewald Water [89]			
O	−1.0484	3.16435	0.16275
H	+0.5242	0.0	0.0
Dang Ion Parameters [86, 93]			
K^+	+1.00	3.331	0.100
Cl^-	−1.00	4.40	0.100
JC Ion Parameters [90, 91]			
K^+	+1.00	2.83306	0.0116615
Cl^-	−1.00	4.91776	0.2794651

Table 3.1: LJ and electrostatic parameters used to simulate aqueous KCl solutions. Note that e is the elementary charge.

All simulations were carried out in the isobaric-isothermic ensemble (fixed NPT) with the pressure and temperature kept constant by using the Nosé-Hoover barostat and thermostat [59]. The simulations were run at typical experimental conditions, with a pressure of 1 atm and a temperature of 293 K and 298 K. A cubic simulation box with periodic boundary conditions was used. The initial length of a side of the box was chosen to be of 40 Å. The molecules were packed into the

% by mass KCl	b (mol kg^{-1})	KCl	H_2O	s	$n_w(K^+)$	$n_w(Cl^-)$
1.03	0.139	5	1990	0.0306	7.03	6.73
2.05	0.280	10	1980	0.0615	6.97	6.67
4.05	0.566	20	1960	0.124	6.86	6.55
7.94	1.16	40	1920	0.254	6.68	6.38
12.0	1.83	62	1876	0.402	6.48	6.17
14.0	2.19	73	1854	0.479	6.41	6.10
15.9	2.55	84	1832	0.558	6.29	5.97
18.0	2.95	96	1808	0.646	6.12	5.80
20.0	3.36	108	1784	0.737	6.06	5.74
22.0	3.78	120	1760	0.830	5.93	5.61
23.9	4.22	132	1736	0.926	5.83	5.51
25.5	4.59	142	1716	1.01	5.75	5.43
26.0	4.59	145	1710	1.03	5.70	5.39
28.0	5.21	158	1684	1.14	5.53	5.20
30.1	5.77	172	1656	1.26	5.43	5.10
32.0	6.30	185	1630	1.38	5.54	5.03
34.0	6.90	199	1602	1.51	5.25	4.92
36.0	7.56	214	1572	1.66	5.09	4.75
38.1	8.24	299	1542	1.81	4.96	4.63
40.0	8.96	244	1512	1.96	4.81	4.48

Table 3.2: KCl mass percentage, molal concentration b, number of K^+ and Cl^- ions, number of water particles, degree of saturation s, and number of waters in the first hydration shell of K^+ $n_w(K^+)$ and Cl^- $n_w(Cl^-)$ for all simulations run. Note that $s = b/b_{sat.}$, where $b_{sat.} = 4.56$ mol kg^{-1} is the experimental saturation concentration at $T = 293$ K.

box using the PackMol program [51]. Time integration was performed using the Tuckerman Verlet algorithm [94]. The LJ interaction calculations were truncated at a distance of 12.0 Å. Long-ranged Coulombic interactions were calculated using the particle-particle particle-mesh (PPPM) method [58, 59, 95]. The simulations was 'relaxed' using a timestep of 0.1 fs for 1 ps before being equilibrated for 50 ps using a 1.0 fs timesteps. The systems were then simulated for a total of 1 ns with a timestep of 1 fs to obtain the results necessary for the calculations of the diffusion coefficients of the ions, the concentration, and the mass density. The TIP4P-Ew+JC model was run for a further 5 ns to allow for observation of Stillinger clustering behaviour [96–98]. Likewise, the TIP3P-Ew+Dang model was run for a further 10 ns to obtain data about the different forms of clustering occurring. Doing this ensures that the uncertainty in the results is in the regime described in Section 2.7.4.

Simulations were run using the LAMMPS software [50]. All simulations run

were composed of potassium ions, chloride ions, and water molecules only. The simulations were set up so that a total of 2000 molecules were placed in the simulation box, with the ratio in the number of potassium chloride to water molecules chosen to create a solution of a specific ionic concentration, $b = 0.14$ – 8.96 mol kg^{-1}. The exact concentrations and numbers of molecules run are shown in Table 3.2.

3.3 Results and discussions

3.3.1 Sub-saturation dynamic properties

The dynamic properties of the four models were compared against experimental results. Four quantities being compared are the solution density, the molar conductivity, and the ion self-diffusion coefficients at varying concentrations less than or equal to experimental saturation ($b_{\text{sat.}} = 4.56$ mol kg^{-1}). The conductivity was calculated using the current-current Green-Kubo relation. The current $J(t)$ at time t is defined as

$$\boldsymbol{J}(t) = \sum^{N} q_i \boldsymbol{v}_i(t) \tag{3.2}$$

where N is the total number of particles in the system, q_i is the charge of particle i, and $\boldsymbol{v}_i$ is the velocity of particle i. The conductivity Λ is then defined as

$$\Lambda = \frac{1}{3Vk_bT} \int_0^\infty \langle \boldsymbol{J}(t) \cdot \boldsymbol{J}(0) \rangle dt \tag{3.3}$$

where V is the volume of the simulation box. The ionic self-diffusion coefficients were calculated by integrating the velocity autocorrelation function defined as

$$D = \frac{1}{3} \int_0^\infty \langle \boldsymbol{v}_i(t) \cdot \boldsymbol{v}_i(0) \rangle dt. \tag{3.4}$$

The results of these comparisons are shown in Fig. 3.1.

From Fig. 3.1(b-d), it can be seen that both TIP3P-Ew+Dang and TIP4P-

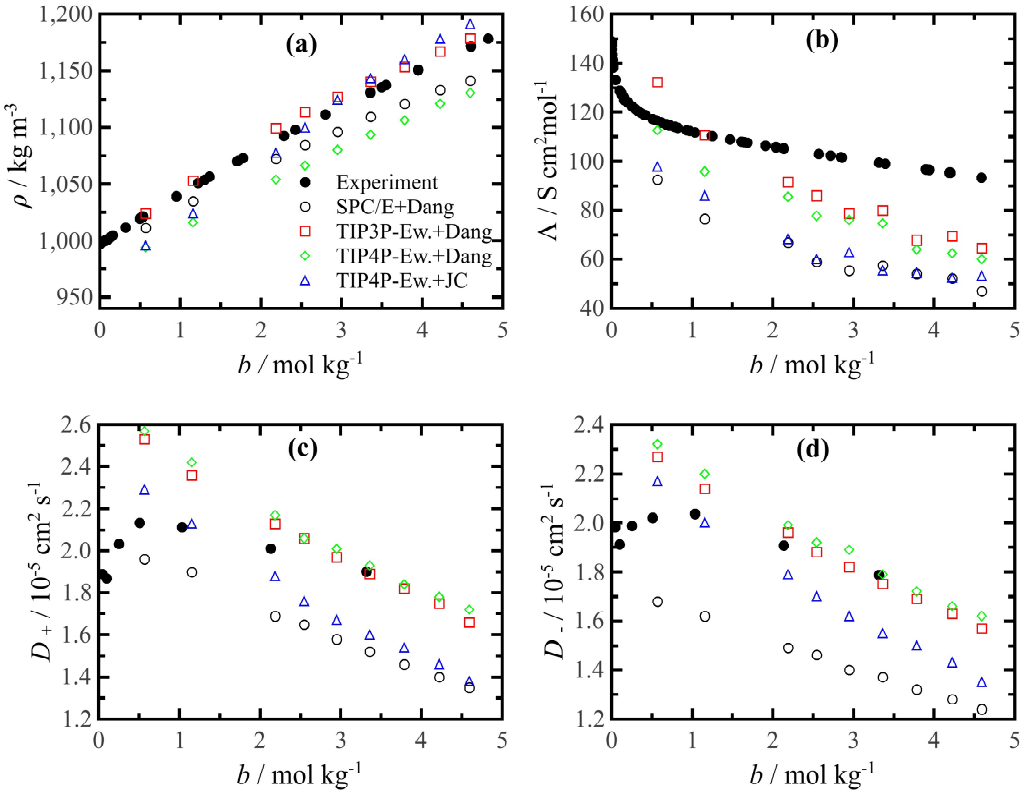

Figure 3.1: Dynamic properties of aqueous KCl solutions at $T = 298$ K obtained from experiment (filled symbols) and from simulations using different models (opened symbols) as a function of concentration: (a) mass density [99]; (b) molar conductivity [100]; (c) and (d) self-diffusion coefficients for aqueous K^+ and aqueous Cl^- respectively [101].

Ew+Dang models closely follow the experimental variations in both the conductivity and the ionic self-diffusion coefficients. Furthermore, at high concentrations they are clearly closer to experimental data than either the TIP4P-Ew+JC or SPC/E+Dang models. The TIP3P-Ew+Dang model achieves a closer fit with experimental density than any other model [Fig. 3.1(a)]. Of all models tested, the TIP3P-Ew+Dang variant gave results closest to experiment for the four properties under consideration. This is, therefore, the model that shall be used to further study the formation of pre-critical clusters in aqueous ionic solutions at high concentrations and to investigate the structure and dynamics of these clusters.

It is possible to use the Nernst-Einstein relation between conductivity and ion self-diffusion coefficients to get an idea of the proportion of ions that do not contribute to the conductivity. The Nernst-Einstein relation linking molar conductivity Λ with the total ion self-diffusion coefficient $D = D_+ + D_-$ is

$$\Lambda = \frac{F^2 D}{RT}(1 - \delta) \tag{3.5}$$

where F is the Faraday constant, R is the molar gas constant, T is the temperature, and δ is a measure of the ion association. At very low concentration, where the self-diffusion of the anion is completely uncoupled from that of the cation, $\delta = 0$. As the concentration is increased, some anion-cation pairs will begin to form. The self-diffusion of these pairs will be coupled rather than completely independent. It follows that, as concentration is increased and ion association grows, δ will also increase as a result of mass transport without a net charge transport in the system, leading to a reduction in conductivity.

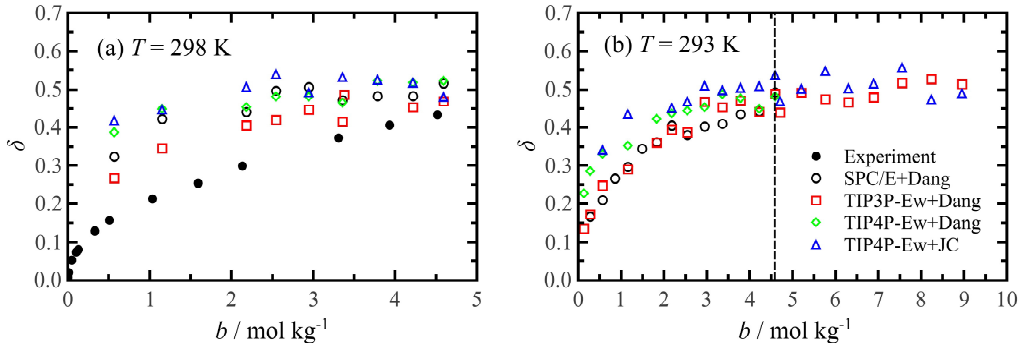

Figure 3.2: Nernst-Einstein δ [Eq. 3.5] obtained from simulation (unfilled symbols) and experiment (filled symbols) as a function of concentration for temperatures (a) $T = 298$ K, and (b) $T = 293$ K. Note that experimental results are only shown up to saturation concentration. Experimental saturation concentration is denoted by the dashed line in (b).

As can be seen in Fig. 3.2, the results from all four models follow the same trend. As the concentration is increased, δ increases and tends to approximately 0.5. While the TIP3P-Ew+Dang model is closest to the experimental curve at very low density, the δ values obtained from all four models are similar to what is experimentally found at concentrations close to saturation. Also shown is the evolution of ion coupling at concentrations past saturation concentration for the TIP3P-Ew+Dang and TIP4P-Ew+JC models to emphasise that $\delta \to 0.5$ as concentration is increased. As there is such a small difference in ionic coupling between the models and experiments, this is a poor criterion for choosing which model to study further.

The TIP4P-Ew+JC model is not as close to the experimental data as the TIP3P-Ew+Dang model for any of the properties tested. The variation of density with

concentration observed in systems run using the TIP4P-Ew+JC model follows a much steeper trend than what is seen experimentally [Fig. 3.1(a)] and increases too quickly as the ion concentration is increased; the conductivities predicted by this model are similar to those predicted for the SPC/E+Dang model and are nearly 50% lower than the experimental values of conductivity near the saturation concentration [Fig. 3.1(b)]; and, while the ionic self-diffusion coefficients are better than those predicted by the SPC/E+Dang model, they are still an underestimate and produce worse results than either the TIP3P-Ew+Dang or TIP4P-Ew+Dang models. This is understandable as this model was created to reproduce experimental salt activity coefficients and experimental solubility. In their paper [91], Joung *et al.* show that the TIP4P-Ew+JC model is able to closely reproduce experimental activities and the saturation concentration whereas the TIP3P-Ew+Dang model produces activities that are much lower than experimentally expected and has a much lower saturation concentration than seen experimentally. It therefore seems wise to look at high-concentration structure in both the TIP3P-Ew+Dang model – the model with the most experimentally accurate dynamic properties – and the TIP4P-Ew+JC model – the model with activities and a saturation concentration closest to what is measured experimentally.

3.3.2 Structure at higher concentrations

Figure 3.3 shows the anion-anion, cation-cation, and anion-cation RDFs obtained from the TIP3P-Ew+Dang and TIP4P-Ew+JC models at various concentrations. Firstly, both models possess very similar static structure at all concentrations. All peaks are at approximately the same position and of approximately the same height. It is interesting that the RDFs for these two models are so similar, given how different some of the dynamic properties are. The second point is that the first peak in the anion-anion and cation-cation RDFs (g_{--} and g_{++} respectively) increase in height as concentration is increased. The second and third peaks may also become more defined, but the associated mid- to long-ranged structure is much more easy to see in the static structure factors (discussed below).

As the RDFs produced by the TIP3P-Ew+Dang model and the TIP4P-Ew+JC model are so similar, only the static structure factors obtained from the TIP3P-Ew+Dang model are shown. Though they are not plotted here, the TIP4P-Ew+JC model produces very similar results at all concentrations tested. Figure 3.4 shows the cation-cation, anion-anion, and anion-cation structure fac-

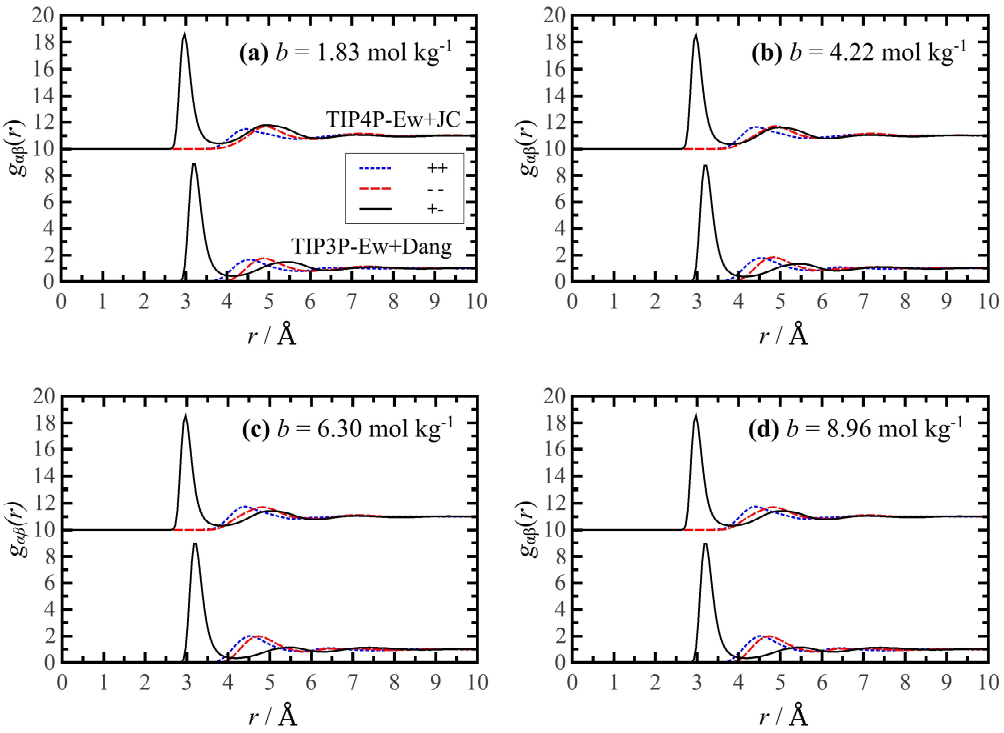

Figure 3.3: Partial RDFs $g_{\alpha\beta}$, where $\alpha, \beta = +, -$ corresponds to K^+, Cl^-, calculated using the TIP3P-Ew+Dang model and those calculated using the TIP4P-Ew+JC model at $T = 293$ K. The concentrations shown are: (a) $b = 1.83$ mol kg^{-1}; (b) $b = 4.22$ mol kg^{-1}; (c) $b = 6.30$ mol kg^{-1}; (d) $b = 8.96$ mol kg^{-1}. The TIP4P-Ew+JC partial RDFs have been shifted up by 10 units for clarity.

tors calculated as described in Section 2.7.3 for a system at experimental subsaturation concentration ($b = 1.83$ mol kg^{-1}), at experimental saturation concentration, and for two compositions above experimental saturation. The cation-cation S_{++}, anion-anion S_{--}, and anion-cation structure factors are defined, respectively, as

$$S_{++} = \frac{1}{N}\langle \rho_+(\boldsymbol{k})\rho_+(-\boldsymbol{k})\rangle \tag{3.6}$$

$$S_{--} = \frac{1}{N}\langle \rho_-(\boldsymbol{k})\rho_-(-\boldsymbol{k})\rangle \tag{3.7}$$

$$S_{+-} = \frac{1}{N}\langle \rho_+(\boldsymbol{k})\rho_-(-\boldsymbol{k})\rangle \tag{3.8}$$

where $\rho_+(\boldsymbol{k})$ and $\rho_-(\boldsymbol{k})$ are the Fourier transforms of the anion and cation densities, respectively. By these definitions, S_{++} and S_{--} should tend to 0.5 at large values of $k = |\boldsymbol{k}|$ whereas S_{+-} should tend towards zero. This is confirmed at all densities plotted in Fig. 3.4.

The most evident result here is that, as concentration is increased, the peaks in the ionic structure factors become more prominent. As expected, $S_{++}(k)$ and $S_{--}(k)$ are very similar at all concentrations. There is near perfect overlap between the two structure factors in all graphs shown here. The first peak is at $k \approx 1.45$ Å^{-1} regardless of concentration, which corresponds to a real-space distance of $R \approx 4.2$ Å – the distance at which the first peak occurs in the g_{++} and g_{--} RDFs in Fig. 3.3.

The first peak in the g_{+-} RDF is quite steep and narrow. It can therefore be approximated by a δ-function at its peak position R. From this, it is possible to approximate the Fourier-transform relation between the structure factor and the RDF. This leads to the following approximation for the anion-cation structure factor

$$S_{+-}(k) \propto \int_0^\infty r^2[g_{+-}(r) - 1] \left(\frac{\sin\, kr}{kr} \right) \mathrm{d}r \simeq \frac{C \sin\, kR}{kR} \tag{3.9}$$

where C is a fitted constant and $R = 3.30$ was defined as being equal to the peak position of the anion-cation RDF. These approximations are plotted alongside the S_{+-} obtained at the concentrations tested in Fig. 3.4. It is evident that this approximation is valid from its close match with the curves obtained from simulation.

To complete the study of the static ionic structure, the number-number, charge-charge, and number-charge structure factors are shown in Fig. 3.5. These structure factors are defined as

$$S_{NN}(k) = \frac{1}{N}\langle \rho_N(\boldsymbol{k})\rho_N(-\boldsymbol{k})\rangle = S_{++}(\boldsymbol{k}) + S_{--}(\boldsymbol{k}) + 2S_{+-}(\boldsymbol{k}) \tag{3.10}$$

$$S_{ZZ}(k) = \frac{1}{N}\langle \rho_Z(\boldsymbol{k})\rho_Z(-\boldsymbol{k})\rangle = S_{++}(\boldsymbol{k}) + S_{--}(\boldsymbol{k}) - 2S_{+-}(\boldsymbol{k}) \tag{3.11}$$

$$S_{NZ}(k) = \frac{1}{N}\langle \rho_N(\boldsymbol{k})\rho_Z(-\boldsymbol{k})\rangle = S_{++}(\boldsymbol{k}) - S_{--}(\boldsymbol{k}) \tag{3.12}$$

where $\rho_N(k) = \rho_+(k) + \rho_-(k)$ and $\rho_Z(k) = \rho_+(k) - \rho_-(k)$ are the Fourier transforms of the total number and charge densities.

There is a large increase in peak intensity in the charge-charge structure factor as concentration is increased, implying some sort of charge-dependent positional

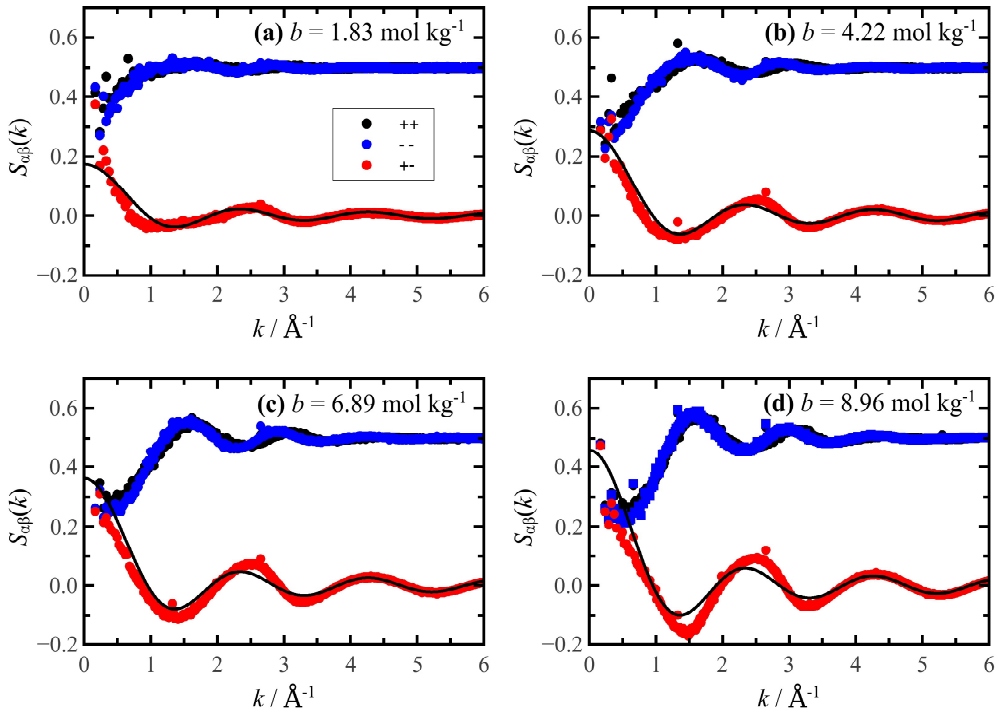

Figure 3.4: Partial structure factor $S_{\alpha\beta}(k)$, where $\alpha, \beta = +, -$ corresponds to K^+, Cl^- respectively, calculated in the TIP3P-Ew+Dang model at $T = 293$ K. The concentrations shown are: (a) $b = 1.83$ mol kg^{-1}; (b) $b = 4.22$ mol kg^{-1}; (c) $b = 6.30$ mol kg^{-1}; (d) $b = 8.96$ mol kg^{-1}.

ordering. The number-charge structure factor shows almost no change at the different concentrations, whereas the number-number structure factor shows that there is more general structure when ionic concentration is increased. As expected from the definitions, S_{NN} and S_{ZZ} tend to 1 as k is increased, and S_{NZ} tends to zero as k increases.

3.3.3 Stillinger clusters and association lifetimes

So far, there have been indications of a rise in anion-cation association as ionic concentration is increased. It seems sensible to study this anion-cation coupling in more depth. More information should be obtained by using the cluster definition proposed by Stillinger [96], as described in the review by Wedekind and Reguerra [97]. Two ions are considered to be clustered if they are of opposite charge and they are within a pre-defined cutoff distance from one another. Here, the cutoff is chosen to coincide with the first minimum in the anion-cation RDF ($r_{ij} = 4.15$ Å). It follows that a particle can be clustered to more than one particle of opposite

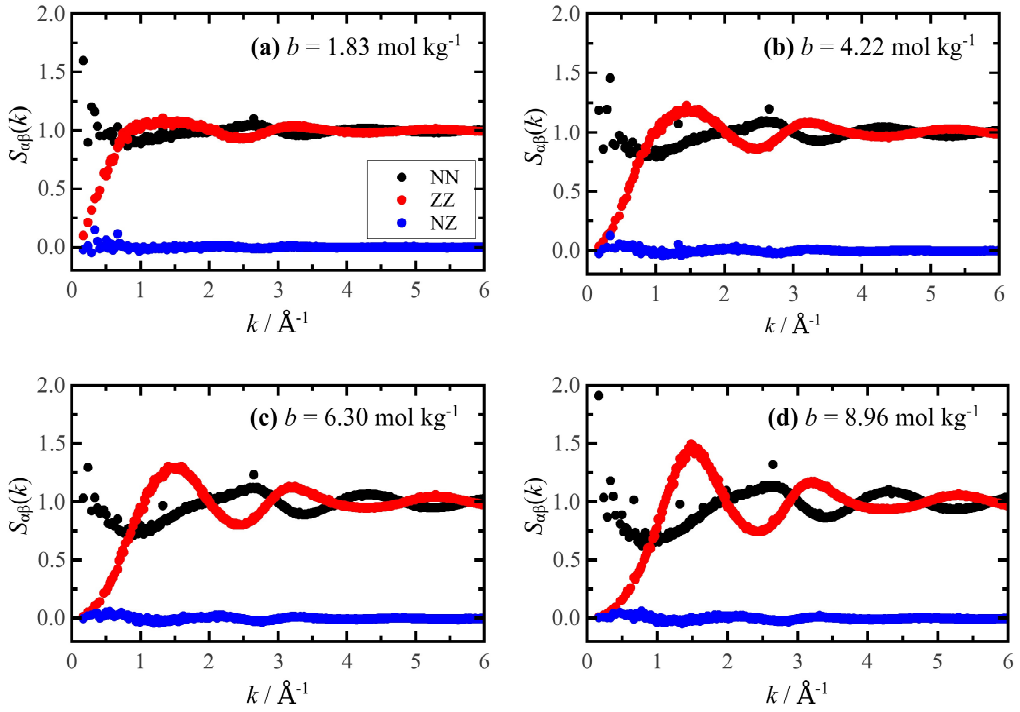

Figure 3.5: Charged/uncharged structure factor $S_{\alpha\beta}$, where $\alpha, \beta =$ N, Z corresponds to the number and charge density respectively, calculated for the TIP3P-Ew+Dang model at $T = 293$ K. The concentrations shown are: (a) $b = 1.83$ mol kg^{-1}; (b) $b = 4.22$ mol kg^{-1}; (c) $b = 6.30$ mol kg^{-1}; (d) $b = 8.96$ mol kg^{-1}.

charge, and that any particle can be part of, at most, one cluster.

As before, simulations were performed using both the TIP3P-Ew+Dang and TIP4P-Ew+JC models at varying concentrations up to $b = 8.96$ mol kg^{-1} to compare the probability of Stillinger clustering occurring in each model. Simulations were run for longer to obtain better statistics of the states of the ions. Figure 3.6 shows the probability of a randomly chosen ion being in a Stillinger cluster at a given concentration. As expected, the clustered probability increases with concentration. At the highest concentrations tested, 85–90% of ions are in a cluster at any given time. Though the TIP3P-Ew+Dang model has a slightly higher clustering probability α, there is very little difference in the dependence of α found in simulations using the TIP3P-Ew+Dang model and the TIP4P-Ew+JC model.

Also shown in Fig. 3.6 is the probability of finding a randomly chosen particle in a cluster of overall neutral charge, that is a cluster composed of exactly the same number of anions as cations, and the probability of finding a particle in a charged cluster. At low concentrations the charged-cluster probability is very

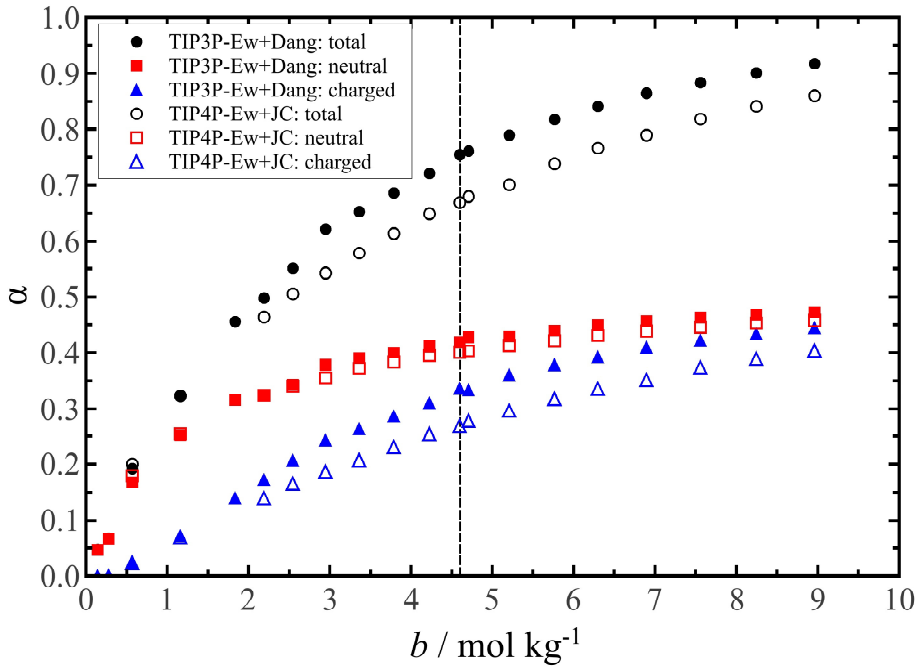

Figure 3.6: Probability α of an ion being part of a charged, neutral, or any Stillinger cluster as a function of concentration at $T = 293$ K. The filled symbols are for the TIP3P-Ew+Dang model and the unfilled symbols are for the TIP4P-Ew+JC model. The dashed line show the experimental saturation concentration $b_{\text{sat}} = 4.56$ mol kg^{-1} at $T = 293$ K

small. This implies that the clusters found at low concentration are mainly anion-cation pairs, possibly with some quartets forming. As these clusters are small, the presence of non-neutral clusters would result in areas of high charge inequality that would likely be unstable and short-lived. Increasing concentration results in the clusters increasing in size. The addition of a single ion to a large neutral-charge cluster will result in a smaller cluster charge density, leading to the cluster being in a more stable state and longer-lived. This explains why the charged and neutral probabilities tend towards the same value as concentration is increased. The probabilities of neutral clusters in both models are almost overlapping at all concentrations, whereas the charged-cluster probability for the TIP4P-Ew+JC model increases at a slower rate than for the equivalent TIP3P-Ew+Dang models. It appears that the discrepancy in the total number of clustered particles found in the two systems at high concentration is mainly a result of this difference in charged cluster probability.

Figure 3.7 shows the probability p_n of finding a cluster of size n in a TIP3P-Ew+Dang simulation at various concentrations $b = 0.556$, 1.83, 4.59, 6.30, 7.56,

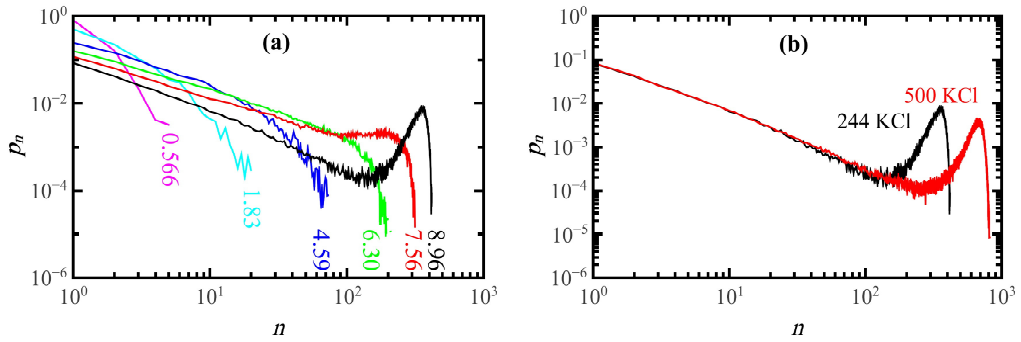

Figure 3.7: Probability p_n of finding a cluster of size n during a 10 ns simulation using the TIP3P-Ew+Dang model at $T = 293$ K. (a) p_n for varying concentrations $b = 0.566$, 1.83, 4.59, 6.30, 7.56, and 8.96 mol kg^{-1}, ascending from left to right. (b) p_n for two simulations (one with 244 KCl and one with 500 KCl) at concentration $b = 8.96$ mol kg^{-1}.

and 8.98 mol kg^{-1}. The sizes of clusters present increase as concentration is increased. This may result from the larger number of ions present in the higher concentration solutions or from the fact that clusters are more easily formed at higher concentrations. A peak at high n begins to form for solutions above a concentration of $b = 7.56$ mol kg^{-1} [Fig. 3.7(a)]. At these concentration, clusters begin to form that percolate the simulation box. Therefore, this high-n peak is likely a caused by finite size effects. Results for p_n at the highest concentration were recalculated for a simulation with a larger total number of ions run at the same concentration $b = 8.96$ mol kg^{-1}, but with 500 K^+ and 500 Cl^- ions as opposed to the original run which had 244 K^+ and 244 Cl^- ions. The peak in the resulting probability function, shown in Fig. 3.7(b), has clearly shifted to a larger corresponding cluster size n. This indicates that the peak in p_n at high concentrations is a result of finite size effects, rather than being caused by a drastic change in the clustering behaviour of ions.

The number of particles present in a cluster of average size $\langle n \rangle$ as a function of concentration b is shown in Fig. 3.8. The average cluster size increases smoothly with concentration. It is worth pointing out that the average cluster size observed in solutions with concentrations $b > 7.56$ mol kg^{-1} may be affected by the peaks resulting from finite size effects observed in the cluster size distribution [Fig. 3.7]. However, given the small probability of the peak, this should have a minimal effect on the average and the trend seen in Fig. 3.8 should be considered as being representative.

As cluster size and the proportion of ions in a cluster increase with concentration,

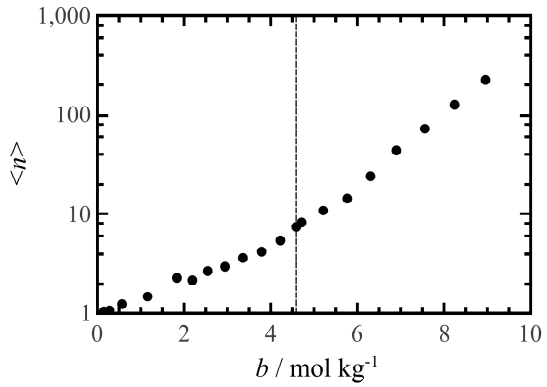

Figure 3.8: Average cluster size $\langle n \rangle$ found in a TIP3P-Ew+Dang simulation as a function of concentration. The runs were carried out at $T = 293$ K. The dashed line shows experimental saturation concentration $b_{\mathsf{sat}} = 4.56$ mol kg^{-1}

it should follow that the residence time, the amount of time that an average particle will spend in a cluster, should increase with concentration also. From the definition of a Stillinger cluster, the average particle residence time can be defined as follows. Suppose we have a function $\theta_i(t)$ defined as:

$$\theta_i(t) = \begin{cases} 1 & \text{if ion } i \text{ is clustered from } 0 \leq t' \leq t \\ 0 & \text{if ion } i \text{ is unclustered at any } t' \leq t \end{cases} \tag{3.13}$$

It is then possible to define a time-correlation function $C_\theta(t)$ as :

$$C_\theta(t) = \frac{1}{N} \sum_{i=0}^{N} \theta_i(t) \tag{3.14}$$

where N is the total number of ions in the simulation. This function reflects average proportion of particles that are clustered at a time t given that they were in a cluster at a time $t = 0$. This can be used to provide the residence time t_{res} of an ion in a cluster. This residence time is

$$t_{\text{res}} = \frac{1}{C_\theta(0)} \int_0^\infty C_\theta(t) dt. \tag{3.15}$$

The ion-association correlation functions $C_\theta(t)$ are shown in Fig. 3.9(a) for a range of concentrations ($b = 0.14$, 0.86, 1.83, 4.22, 6.30, and 8.96 mol kg^{-1}). It is clear that, as concentration is increased, $C_\theta(t)$ decays more slowly over time.

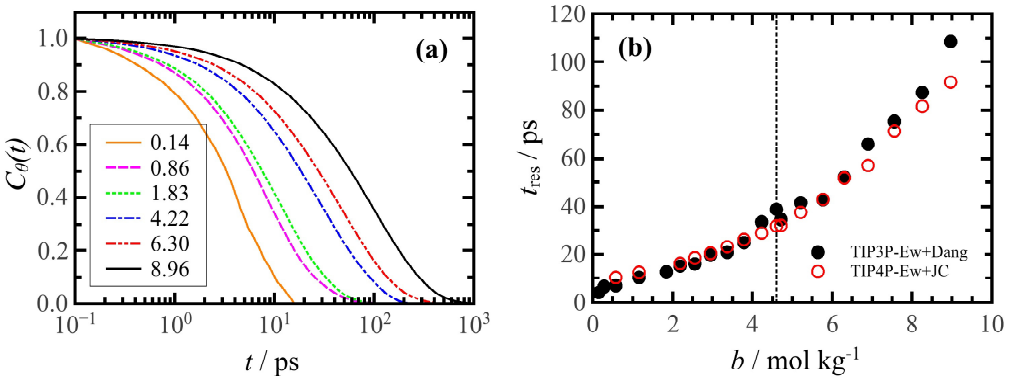

Figure 3.9: (a) Ion association correlation function C_θ given by Eq. 3.14 at different concentrations $b = 0.14$, 0.86, 1.83, 4.22, 6.30, and 8.96 mol kg^{-1} for simulations run using the TIP3P-Ew+Dang model at $T = 293$ K. (b) Residence time t_{res} as a function of concentration obtained from models using the TIP3P-Ew+Dang model (full black circles) and the TIP4P-Ew+JC model (empty red circles) at $T = 293$ K. The dashed line shows the experimental saturation concentration $b = 4.59$ mol kg^{-1}.

This shows that, on average, particles remain in a clustered state for longer times at higher concentrations. The results shown are only from the TIP3P-Ew+Dang model but the results from the TIP4P-Ew+JC model are very similar.

Figure 3.9(b) shows the residence time t_{res} as a function of ion concentration for both the TIP3P-Ew+Dang and the TIP4P-Ew+Dang models. The residence times observed in both models show very similar behaviour, with the TIP3P-Ew+Dang model having only slightly longer residence times at concentrations above experimental saturation ($b_{\text{sat}} = 4.59$ mol kg^{-1}) than the equivalent TIP4P-Ew+JC system. This is quite interesting as it further shows that these two models provide very similar results with regards to Stillinger cluster formation and lifetimes, even though one model appears to be better at predicting common dynamic properties and the other has been parametrised to give an accurate solubility. Moreover, past experimental saturation concentration, the cluster residence time is in the range 40 - 100 ps. This is of the same order of magnitude as the timescale on which the laser pulse is thought to act in the NPLIN process.

The increase in the residence time as concentration increases is most likely caused by a combination of two factors. The first reason is related to the definition of a Stillinger cluster being used. The Stillinger cutoff radius $r_c = 4.15$ Å, calculated by using the first minimum in the K^+–Cl^- RDF [Fig. 3.3], does not take into account the average number of ions within that cutoff. As the cutoff is constant at all concentrations, one would expect that at higher concentrations would lead

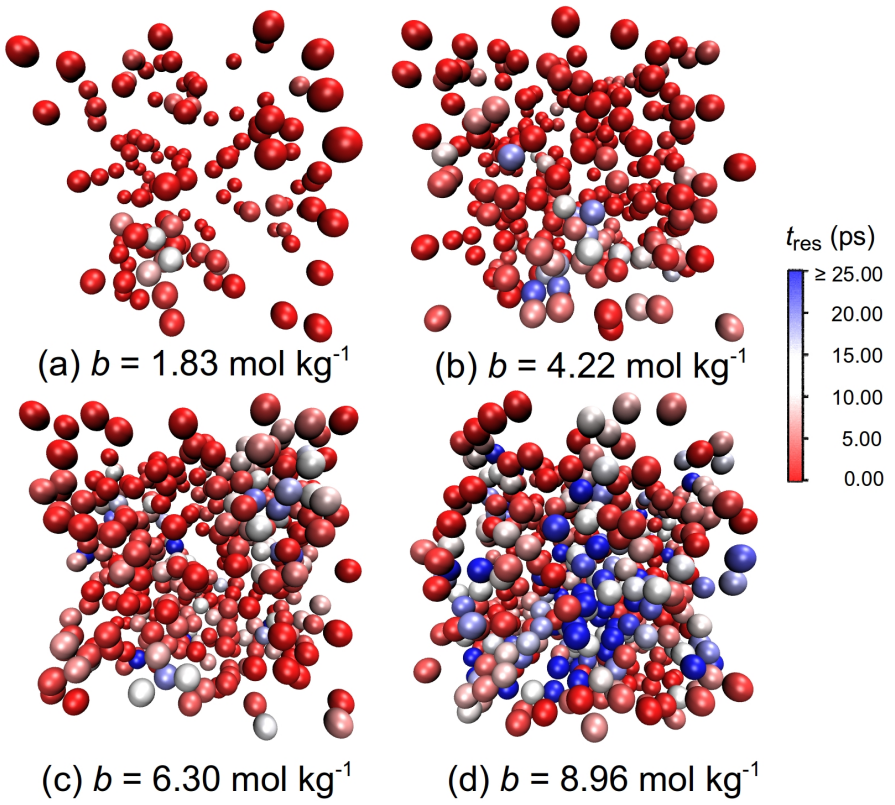

Figure 3.10: Figure showing simulation snapshots, where ions are coloured according to their cluster residence time t_{res} from this point in the simulation. Ions that are unclustered in this snapshot are assigned a $t_{\text{res}} = 0$ ps and coloured red; ions that remain clustered for a length of time greater than or equal to 25 ps are coloured blue.

to more ions falling within this cutoff. This makes it more likely for ions to be in a clustered state, as was seen in Fig. 3.6. At the highest concentrations, 80-90 % of particles are bound at any given point. Therefore, by a simple statistical argument, the residence time should increase even if the number of ions clustered at time t is completely dissociated from the number of ions clustered at time $t + \delta t$.

The second explanation for these longer lifetimes is that this results from the presence of larger clusters. The average cluster size increases with concentration [Fig. 3.7]. Figure 3.10 shows snapshots of simulations, with the particles coloured according to the time that they will remain in a cluster following this point. It can be seen that particles remaining in a clustered state for long periods of time are bunched together. It is likely that a particle found at the centre of a cluster will take longer to reach a non-clustered state. This state may be reached by the particle diffusing out of the cluster or by the cluster dissolving around it, but the conclusion is the same: the larger the cluster, the longer it takes for all particles

in it to reach a non-clustered state. Given the huge increase in residence time seen here, the second reason is a more likely candidate than the first.

3.3.4 Water and hydration shells

An important effect of crystal formation is the dehydration of the pre-nucleating crystal cluster [77, 78]. It is therefore interesting to look at the structure and residence time of the water around the ions. These are studied for the TIP3P-Ew+Dang model here.

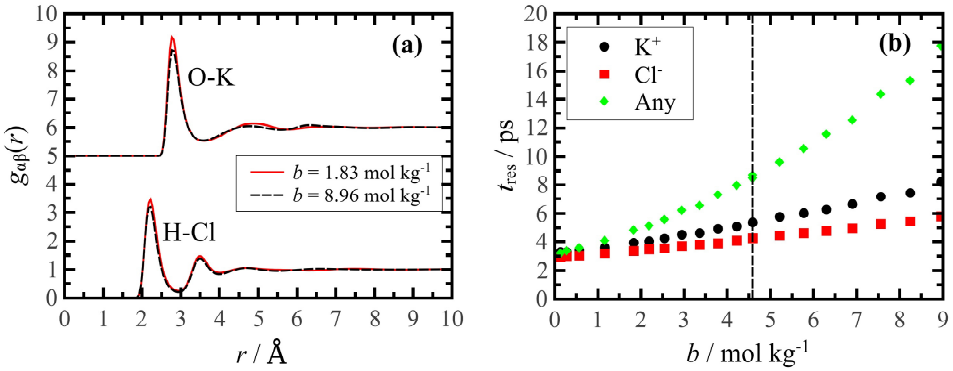

Figure 3.11: (a) O–K (top) and H–Cl (bottom) radial distribution function for the TIP3P-Ew+Dang model at $T = 293$ K. The solid red line shows results at a concentration $b = 1.83$ mol kg^{-1} and the dashed black line shows results at a concentration $b = 8.96$ mol kg^{-1}. (b) Hydration residence times for K^+ ions (black circles), Cl^- ions (red squares) and all ions (green diamonds). The vertical dashed line shows experimental saturation concentration $b_{sat} = 4.59$ mol kg^{-1}

Figure 3.11(a) shows the O–K and H–Cl RDFs calculated at concentrations of $b = 1.83$ and 8.96 mol kg^{-1}. There is very little difference between the structures observed at these concentrations. This implies that the hydration shells are, on the whole, similar for the anions and cations at both concentrations. It also strongly implies that the Stillinger clusters are unlikely to be anhydrous, and that therefore the clusters are not close to reaching a crystal forming state. The O–Cl and H–K RDFs (not shown here) show similar trends as concentration is increased.

Figure 3.11(b) shows how the water-ion residence time changes as a function of concentration. The water-K^+ and water-Cl^- residence times increase very slightly, and following similar, near linear trends as the concentration is increased. The water-all ion residence time increases faster with concentration, but does not

increase as quickly as, or by the same scale as, the K^+-Cl^- residence times shown in Fig. 3.9. It is highly likely that the increase in residence time of the water is a result of the higher number of ions present, rather than a result of an increase in the water-ion association. Note that the longest water-all ion residence time is much lower than the timescale on which NPLIN is thought to act on pre-critical crystal nuclei. Moreover, ion-ion residence time is between four and six times greater than the water-all ion residence time at all concentrations simulated. This strongly suggests that the dehydration process is not the rate-determining process when NPLIN occurs.

3.4 Conclusions

In this section, the changes in structure and dynamic properties of aqueous potassium chloride solutions as concentration is increased past the experimental saturation concentration have been studied. This work was carried out to better understand the complex structure and dynamics in supersaturated salt solutions in the hope of understanding what happens to the system when it undergoes NPLIN. Experimentally, it has been demonstrated that, if the laser pulse used is of 5 ps or less, no crystallisation occurs. If the laser pulse is of a duration longer than 100 ps, then nucleation and subsequent crystallisation is observed [8]. It is worth emphasising again that homogeneous crystallisation is not of interest in this work and that no spontaneous crystallisation was observed in these simulations. Rather, this was done to look for long-lasting structures on which the laser pulses used in NPLIN could act to begin the process of crystallisation.

First, the density, ion self-diffusion coefficients, and molar conductivity obtained for four ion-water models were compared to results obtained by experiment. From these four models, models were chosen for further analysis: the model with the closest fit to experimental results (the TIP3P-Ew water model with KCl parameters developed by Dang [86]) and a model that had been parametrised to reproduce the experimental solubility (the TIP4P-Ew water model with KCl ion parameters developed by Joung and Cheatham [90, 91]). The structure present in simulations run using these models was analysed for a set of concentrations ranging from low concentration up to about two times the experimental saturation concentration. It was shown that there is very little difference between the structures of both model at all concentrations. Furthermore, it was found

that, for all concentrations, the dominant structural features resulted from strong anion-cation association. The degree of association grows as the concentration is increased.

The strong anion-cation association was used to develop a clustering criterion from which the evolution of the average lifetime of an ion in a cluster as concentration increases was found. Again, it is worth noting that the cluster sizes and cluster lifetimes calculated from both of these models are very similar. Also of interest is that the cluster residence time at experimental saturation concentration was found to be 40 ps – a timescale of the same order of magnitude as the duration of the laser pulse used in NPLIN. The residence time of a water molecule in the first hydration shell is found to be much shorter, at roughly 10 ps at experimental saturation, and increases at a less significant rate past this point.

This work has hinted at the complexities in the motion and structure of aqueous KCl at high concentrations. Ion cluster lifetimes were of the same order of magnitude as the timescale needed for NPLIN to occur. It is possible that the laser pulse used in NPLIN acts on these clusters of higher ion density, rearranging them into a crystal nucleus that then grows in the supersaturated system. This strongly suggests that, at least for aqueous potassium chloride, crystallisation is a two-step process, with the first step being the formation and dissolution of these long-lived amorphous crystals and the second being the rearrangement of these clusters into more crystalline structures. While long-lived clusters are present, there is no real evidence of crystalline or anhydrous ion clusters forming, even for short periods of time. This is coherent with the experimental observation that supersaturated aqueous potassium chloride can remain in a metastable state for months without crystals forming.

Chapter 4

The effects of the heating of carbon nano-impurities on the structure of aqueous sodium chloride

4.1 Introduction

One proposed mechanism to explain non-photochemical laser-induced nucleation (NPLIN) is that the near-infra-red laser pulse acts on small impurities present in the solution. It is speculated that impurities of size on the nanometre scale (1 – 100 nm) exist in these solutions. These would be nearly impossible to filter out because of their small size, and could absorb energy from the laser pulse, leading to the impurities rising in temperature. Recent studies suggest that nanometre gold impurities can be heated to very high levels in water, sometimes causing localised evaporation of the water surrounding the nanoparticle and leading to the formation of a bubble [102–106]. Given the small masses of these impurities, and their presumed rarity in filtered solutions, this should have a negligible effect on the overall temperature of the system. However, the energy absorbed by the nanoparticles will diffuse into the surrounding solution, resulting in localised heating that may lead to the formation of nanobubbles as the surrounding solution locally evaporates [107, 108]. The presence of a nanobubble may facilitate the crystallisation process in supersaturated solutions *via* the creation of a shockwave

when the bubble collapses or perhaps by causing local evaporation of the solvent and leaving only the solute. This could be one potential explanation of the mechanism by which NPLIN works.

It is also possible that localised heating resulting from a highly energetic impurity has other effects on the supersaturated solution in which it is immersed. Very little research has been done on the effects that localised heating may have on an aqueous salt solution. From a statistical physics and computational point of view, studying localised heating is particularly interesting as this is a non-equilibrium situation. Furthermore, though a lot of research has been carried out on the solution–solid interface, little work has been done on the interface between a solid spherical particle with high surface curvature immersed in a liquid.

In this chapter, the effects that the instant heating of a 4 nm carbon nanoparticle has on a surrounding aqueous salt solution are studied. As this is thought to potentially cause a supersaturated system to crystallise, it is important for the solutions modelled to be near simulation saturation concentration. As shown in Chapter 3, the aqueous potassium chloride solutions simulated did not crystallise, even at concentrations near experimental saturation concentration. In this chapter, the solution modelled is aqueous sodium chloride. This system has been studied at high concentrations much more than potassium chloride solutions. Experimentally, supersaturated NaCl solutions are much more difficult to keep in a supersaturated metastable state than supersaturated KCl solutions, with supersaturated solutions of NaCl crystallising within minutes or hours. Computationally, this system presents one key advantage over equivalent aqueous KCl system, namely that MD simulations have shown that, at concentrations similar to the experimental saturation concentration, this system can crystallise within the simulation timescale [77, 78]. It should therefore be possible to find a maximum concentration at which the system does not undergo crystallisation within the simulation timescale, or 'simulation saturation concentration'. At this concentration, the system will very likely crystallise if given a much longer simulation run (of order μs or ms, rather than ns), meaning that the system is still in a metastable state. Therefore, crystallisation may be induced at this concentration by perturbing it from its current metastable condition. This is, in effect, the nanobubble mechanism proposed to explain NPLIN.

In their paper, Zimmermann *et al.* estimate the experimental nucleation rates of these systems as ranging from 10^4 – 10^{13} cm^{-3} s^{-1} [109]. A typical simulation has volume of order 10^{-21} – 10^{-18} cm and is run for 10^{-9} – 10^{-6} s. It follows

that, for a perfectly accurate model, crystallisation should not be observed. However, in their recent work, Benavides *et al.* demonstrate that forcefields used to model aqueous NaCl systems often underestimate experimental solubility, with the best model tested having a solubility nearly 40% lower than experimental solubility [92]. This explains why crystallisation can be observed in certain simulations of supersaturated aqueous NaCl solutions. As the work presented here is studying the effects of heated particle impurities on inducing crystallisation, it is not necessary for the simulation to accurately model experiment for useful conclusions to be drawn.

This chapter is divided as follows. First, the analysis used to find the 'simulation saturation concentration' of aqueous NaCl (without impurity) is described. Then, the simulation methods used for the systems composed of a carbon impurity in an aqueous NaCl solution are detailed. The results are then presented, with the 'simulation saturation concentration' derived, and the effects of heating two 4 nm impurity, one solid and one hollow, presented. These results are discussed and analysed before concluding remarks are given.

4.2 Methods

4.2.1 Interaction potentials and simulation parameters

All systems were run using the TIP3P-Ewald water model [88], with ion parameters and carbon parameters developed by Dang and co-workers [110, 111]. The TIP3P water model assumes that water molecules are kept rigid, and that the bonds and angles can not fluctuate from their equilibrium positions. The total potential energy of the system is given by

$$U = \sum_{i<j} \left(U_{ij}^{\mathrm{LJ}} + U_{ij}^{\mathrm{Coul}} \right) \tag{4.1}$$

where

$$U_{ij}^{\mathrm{LJ}} = 4\epsilon_{ij} \left[\left(\frac{\sigma_{ij}}{r_{ij}} \right)^{12} - \left(\frac{\sigma_{ij}}{r_{ij}} \right)^{6} \right] \tag{4.2}$$

is the interparticle Lennard-Jones (LJ) interaction potential between particles i and j, and

$$U_{ij}^{\text{Coul}} = \frac{1}{4\pi\varepsilon_0}\frac{q_i q_j}{r_{ij}} \tag{4.3}$$

is the interparticle Coulombic potential between particles i and j. Here, $r_{ij} = |\boldsymbol{r}_j - \boldsymbol{r}_i|$ is the interparticle distance, q_i is the charge of particle i, σ_{ii} and ϵ_{ii} are the LJ radius and energy of species i, respectively, and $\sigma_{ij} = (\sigma_{ii} + \sigma_{jj})/2$ and $\epsilon_{ij} = (\epsilon_{ii}\epsilon_{jj})^{1/2}$ are the cross-interaction parameters according to the Lorentz-Berthelot mixing rules. The potential parameters σ_{ii}, ϵ_{ii}, and q_i used in this work are summarised in Table 4.1.

	q_i (e)	σ_{ii} (Å)	ϵ_{ii}(kcal mol^{-1})	Ref.
O	−0.830	3.188	0.1020	[88]
H	+0.415	0.000	0.0000	[88]
Na^+	+1.000	2.350	0.1300	[110]
Cl^-	−1.000	4.400	0.1000	[86]
C	0.000	3.550	0.0635	[111]

Table 4.1: LJ and electrostatic parameters used to simulate aqueous NaCl solutions with and without a carbon impurity. Note that e is the elementary charge.

4.2.2 Simulation saturation concentration

As stated before, the work discussed in this chapter is about studying one potential mechanism by which NPLIN may cause crystallisation. As such, it is important to ensure that the aqueous salt systems tested are not able to crystallise within the simulation timescale, but also that the systems are as close to crystallising as possible. Here, crystalline clusters of ions are of interest, as opposed to the localised amorphous Stillinger clusters of ions discussed in Chapter 3. Two separate methods are used to decide whether a particle is in a crystalline state. The first method is a more sophisticated version of the Stillinger clustering criterion. An ion is considered in a crystalline state if it has a minimum of four Stillinger neighbours. This modification was proposed by ten Wolde and Frenkel, and shall be referred to as the TWF clustering criterion [97, 112]. As before, the neighbour cutoff distance is defined as the first minimum in the anion-cation RDF ($r_{\text{cutoff}} = 3.80$ Å). Unlike for the Stillinger cluster definition used in Chapter 3,

there is no charge criterion when defining a neighbour, meaning that an anion can have an anion as a neighbour.

The second method used to define a crystalline particle is the Steinhardt or local-order parameter. This is a commonly used parameter to define whether a single particle is in a crystalline state [113,114]. This method has been shown to work for a multitude of systems, ranging from Lennard-Jones fluids crystallising [115–118] to the study of water crystallisation [119–121]. The local-order parameter can be viewed as an extension to the TWF clustering parameter. As before, a neighbour cutoff distance is defined, and as before, a minimum number of nearest neighbours must be present for a given particle to be considered crystalline. For ease, this minimum number of Stillinger neighbours is chosen to be four, the same as for TWF clustering, meaning that ions that pass the local-order parameter criterion are a subset of those that pass the TWF clustering criterion. For all ions, a $(2l+1)$ dimensional vector is defined as

$$Q_{lm}(i) = \frac{1}{N_\mathrm{b}(i)} \sum_{j=1}^{N_\mathrm{b}} Y_{lm}(\hat{\boldsymbol{r}}_{ij}) \tag{4.4}$$

where $N_\mathrm{b}(i)$ is the list of neighbouring ions to ion i within the cutoff distance, and $Y_{lm}(\hat{\boldsymbol{r}}_{ij})$ are the spherical harmonics evaluated for the direction unit vector $\hat{\boldsymbol{r}}_{ij} = \boldsymbol{r}_{ij}/|\boldsymbol{r}_{ij}|$ [113, 114]. The direction unit vector $\hat{\boldsymbol{r}}_{ij} = (r_{ij}, \theta_{ij}, \phi_{ij})$ is given by the direction $r_{ij} = (x_{ij}^2 + y_{ij}^2 + z_{ij}^2)^{1/2}$, the polar angle $\theta_{ij} = \arccos(z_{ij}/r_{ij})$, and the azimuthal angle $\phi_{ij} = \arctan(y_{ij}/x_{ij})$. From these, a rotationally invariant local bond-order parameter can be defined for each ion as

$$Q_l(i) = \left(\frac{4\pi}{2l+1} \sum_{m=-l}^{l} |Q_{lm}(i)|^2 \right)^{1/2} . \tag{4.5}$$

In this work, the Q_4 local-order parameter will be used to differentiate a crystalline ion from a non-crystalline one, with a crystalline ion defined as one with $Q_4(i) > 0.45$.

Unlike with Stillinger clustering, both the TWF clustering and local-order parameter definitions mean that a particle can be in a clustered state while all of its neighbours are not. For consistency with the Stillinger cluster definition, all neighbours of ions that fulfil the TWF or Q_4 criteria are also considered to be in

a clustered state. This ensures that the surface ions of a crystal are retained as part of the crystal too.

Aqueous sodium chloride solutions at various concentrations were simulated. Molecular dynamics (MD) simulations were run in the isobaric-isothermic ensemble (fixed NPT), with pressure $P = 1$ atm and temperature $T = 293$ K. A cubic simulation box with periodic boundary conditions was used. The systems were run with a timestep of 1 fs for a total of 25 ns, with time integration performed using the Tuckerman-Verlet algorithm. The LJ interactions were truncated at 12.0 Å, and the long-ranged Coulombic interactions were calculated using the particle-particle particle-mesh (PPPM) method. The systems were randomly packed, with 500 Na^+ and 500 Cl^- ions. The number of water molecules was then varied to get the desired concentration, with concentrations $b = b_{sat}$, $1.1b_{sat}$, $1.2b_{sat}$, $1.3b_{sat}$, $1.4b_{sat}$, and $1.5b_{sat}$ being simulated, where $b_{sat} = 6.147$ mol kg^{-1} is the experimental saturation concentration at $T = 293$ K [122]. The compositions of the simulations run are shown in Table 4.2.

System	$N(H_2O)$	$N(Na^+)$	$N(Cl^-)$	b / mol kg^{-1}
$1.0b_{sat}$	4507	500	500	6.158
$1.1b_{sat}$	4097	500	500	6.774
$1.2b_{sat}$	3757	500	500	7.387
$1.3b_{sat}$	3468	500	500	8.003
$1.4b_{sat}$	3219	500	500	8.622
$1.5b_{sat}$	3006	500	500	9.233

Table 4.2: Compositions of simulations run to find simulation saturation concentration.

4.2.3 Carbon impurity

Once the simulation saturation point is found (described in Sec. 4.3.2), the highest-concentration, non-crystallising system will be used for further simulations to understand the effects that adding, and heating, an impurity will have on the structure of the aqueous NaCl solution. Two carbon impurities are used in this work, a solid impurity of diameter 4 nm (5851 carbon atoms) and an impurity of the same diameter but with a hollow centre (3378 carbon atoms). The impurities were created from carbon packed in a diamond structure, with only carbons with a minimum of three bonds kept at the surface. The bonds and angles were kept about their equilibrium positions ($r_0 = 1.54$ Å and $\theta_0 = 109.5°$) by using a harmonic potential. Snapshot of the impurities are shown in Figure 4.1.

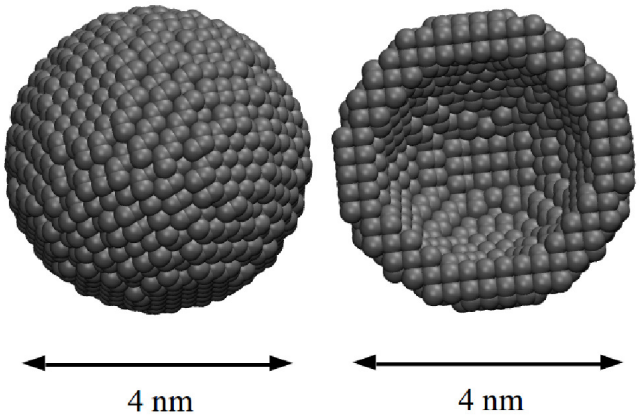

Figure 4.1: Spherical carbon impurities used in the simulations. A 4 nm impurity is shown on the left and a cross-section of the hollow impurity is shown on the right.

The compositions of the systems tested are given in Table 4.3. The simulations were run using a cubic box with periodic boundary conditions. The LJ interactions were truncated at 12.0 Å, and long-ranged Coulombic interactions were calculated using the PPPM method. Systems were run using a 1 fs timestep, with the Tuckerman-Verlet algorithm used for time integration. The systems were allowed to equilibrate under normal experimental conditions (fixed NPT with $T = 293$ K and $P = 1$ atm) for 5 ns before the impurity is heated. Once the impurity is heated, a thermostat would artificially control the flow of heat between the particle and the solution, and would prevent the solution from reaching thermal equilibrium with the hot impurity. To prevent this and to ensure that the pressure is constant at $P = 1$ atm, the system is run under the isobaric-isoenthalpic ensemble (fixed NPH) during the impurity heating and cooling process. The impurity was heated to 5293 K and 10293 K by instantly changing the velocities of the carbon atoms, with new velocities chosen at random from a Gaussian distribution about the desired temperature. The impurities were kept at this higher temperature for a total of 10 ps through use of a thermostat acting on the impurity only. The thermostat was switched off after 10 ps before the systems were run for a total of 2.4 ns, with the particle positions were output every 100 fs for the first 400 ps. Positions were then output every 100 fs between 0.9 – 1.0 ns after heating, 1.5 – 1.6 ps after heating, 1.7 – 1.8 ns after heating, and 2.3 – 2.4 ns after heating. This sampling frequency is a compromise between the need for many samples to obtain good statistics and the need for these samples to be independent from one another, and was chosen to minimise the noise observed in the results.

System	$N(\mathrm{C})$	$N(\mathrm{H_2O})$	$N(\mathrm{Na^+})$	$N(\mathrm{Cl^-})$	b / mol kg^{-1}
Solid	5851	60122	8000	8000	7.386
Hollow	3378	60122	8000	8000	7.386

Table 4.3: Compositions of simulations run with impurities. Note that all of the carbons compose the impurity, and that there are no free carbons in the solution.

4.3 Results and discussions

4.3.1 Defining crystals

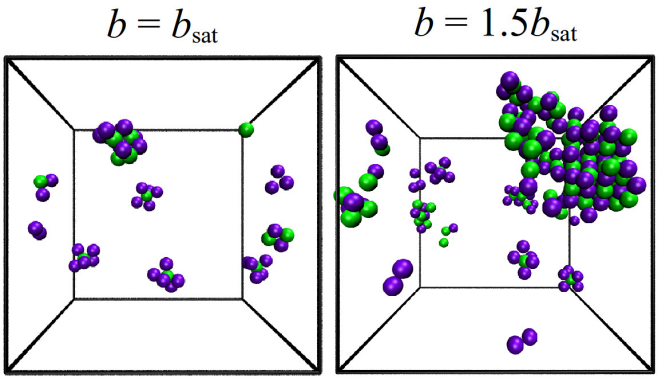

Figure 4.2: Simulation snapshots showing all sodium (purple) and chloride (green) ions in a crystalline state at concentrations $b = b_{\mathrm{sat}}$ (left) and $b = 1.5b_{\mathrm{sat}}$ (right). The local-order parameter criterion described below was used to find crystalline ions.

Simulation snapshots of the crystalline ions found in solutions of concentrations of $b = b_{\mathrm{sat}}$ and $b = 1.5b_{\mathrm{sat}}$ are shown in Fig. 4.2. As can be seen, the simulation run at $b = 1.5b_{\mathrm{sat}}$ shows evident crystalline structure. This shall be used as the model crystallised system when defining the neighbour and local-order parameter cutoff. As there is no evident crystal structure present in the simulation run with $b = b_{\mathrm{sat}}$, this shall be used as the non-crystallised model system. Figure 4.3 shows the probability distribution function that a given ion has N neighbours within a distance $r < 3.80$ Å. As there is no crystalline structure in the low-concentration system, it seems sensible that this system has no more than 10% of particles in a crystalline state. As such, the TWF cluster neighbour cutoff was chosen to be $N_{\mathrm{neigh}} = 5$. A particle is considered clustered if if has at least 5 neighbours within $r_{\mathrm{cutoff}} = 3.80$ Å of its centre of mass. Note again that all neighbours of particles that pass this criterion are also counted as part of this cluster.

From the TWF clustering criterion, it is possible to define a more stringent criterion for crystallisation based on the three-dimensional positioning of the TWF

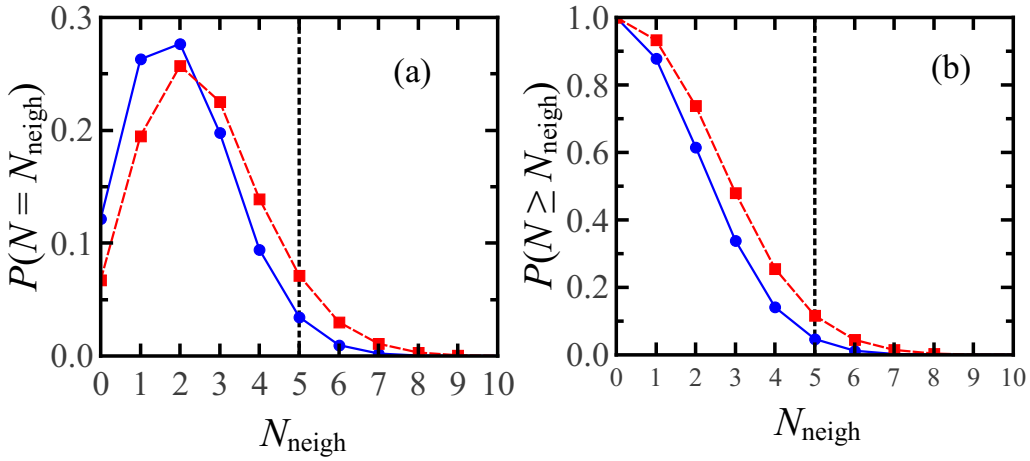

Figure 4.3: Probability distribution of the number of Stillinger neighbours within the cutoff distance $r_{\text{cutoff}} = 3.80$ Å for a simulation run at $b = b_{\text{sat}}$ (full blue line) and $b = 1.5b_{\text{sat}}$ (dashed red line). (a) Probability of a given ion having N neighbours. (b) Probability of a given ion having at least N neighbours. The dotted line at $N = 5$ is to indicate the cutoff at which a particle is considered to be in a TWF clustered state.

neighbours relative to the clustered particle and to one another. The probability distribution of the local-order parameter was calculated for the crystallised and non-crystallised systems, and the results are plotted in Fig. 4.4. The peak in the probability distribution remains at the same position for both concentrations tested, however, there is a more pronounced deviation from a Gaussian-like distribution at the higher concentration of $b = 1.5b_{\text{sat}}$. This deviation from the non-crystallised result occurs for values of $Q_4 \geq 0.45$. This is therefore used as the cutoff value, and particles with a local-order parameter $Q_4(i) < 0.45$ are classed as being in a non-crystallised state, whereas particles with $Q_4(i) \geq 0.45$ are considered to be in a crystalline state. Note that, as with the TWF cluster criterion, the TWF neighbours of particles in a crystalline state are also assumed to be a part of the crystal structure and are therefore also counted as bound.

Figure 4.5 shows a series of simulation snapshots illustrating which ions are selected under the TWF and local-order parameter criteria. Both the TWF and local-order parameter criteria are able to select all of the ions composing the large crystal present in the system. It appears that, while the TWF clustering criterion is able to identify all ions that form a crystalline structure, a significant number of ions in localised high-density regions, but with no crystal-like structure, also satisfy this criterion. The local-order parameter criterion appears to pick out crystalline ions, but some of the small clusters that pass the TWF criterion and appear crystalline to the human eye do not pass the local-order parameter criterion. It appears that the TWF criterion overestimates the total

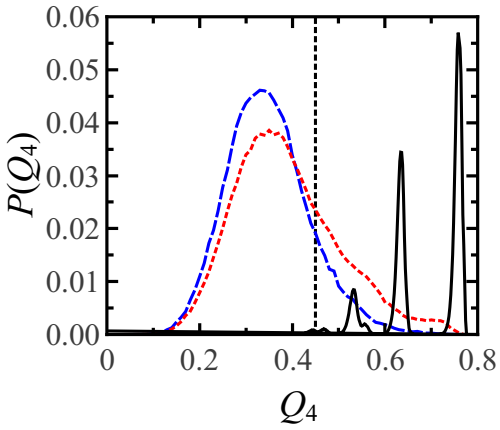

Figure 4.4: Probability distribution function of the Steinhardt or local-order parameter Q_4 for a system at concentration $b = b_{\text{sat}}$ (dashed blue line), one at concentration $b = 1.5b_{\text{sat}}$ (dotted red line), and for crystal NaCl in bulk at $T = 293$ K (black solid line). The dotted black line at $Q_4 = 0.45$ is to indicate the cutoff at which a particle is considered to be in a crystalline state.

number of crystalline ions in the system whereas the Steinhardt order parameter probably underestimates the total number of crystalline ions by disregarding smaller clusters.

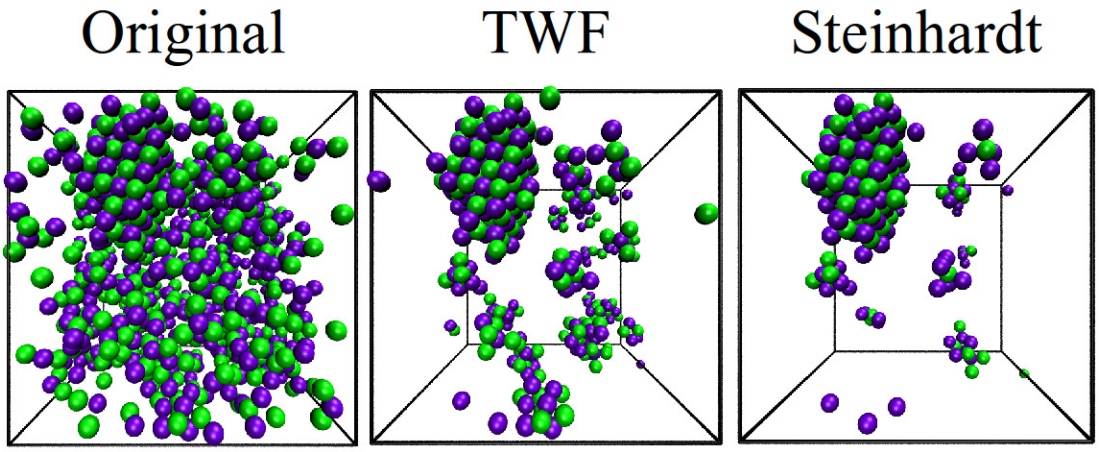

Figure 4.5: Simulation snapshots showing the sodium (purple) and chloride (green) ions. The snapshots show all of the ions in the solution (left), the ions that are bound according to the TWF binding criterion (middle), and the ions that are crystalline according to the local-order parameter criterion (right). These snapshots were generated from the same timestep in a simulation run at $b = 1.4b_{\text{sat}}$.

4.3.2 Simulation saturation concentration

It is possible to calculate the average time that a particle remains in a clustered state. By defining a binary function as

$$\theta_i(t) = \begin{cases} 1 & \text{if ion } i \text{ is clustered from } 0 \leq t' \leq t \\ 0 & \text{if ion } i \text{ is unclustered at any } t' \leq t \end{cases} \tag{4.6}$$

one can define an ion-association time correlation function as

$$C_\theta(t) = \frac{1}{N} \sum_{i=1}^{N} \langle \theta_i(t)\theta_i(0) \rangle \tag{4.7}$$

where N is the total number of ions in the system. $\langle C_\theta(0) \rangle$ will give the average proportion of crystalline ions present in the system at any given time. The time correlation function can be used to obtain the residence time of an ion in a crystalline state:

$$t_{\text{res}} = \frac{1}{C_\theta(0)} \int_0^\infty C_\theta(t) dt. \tag{4.8}$$

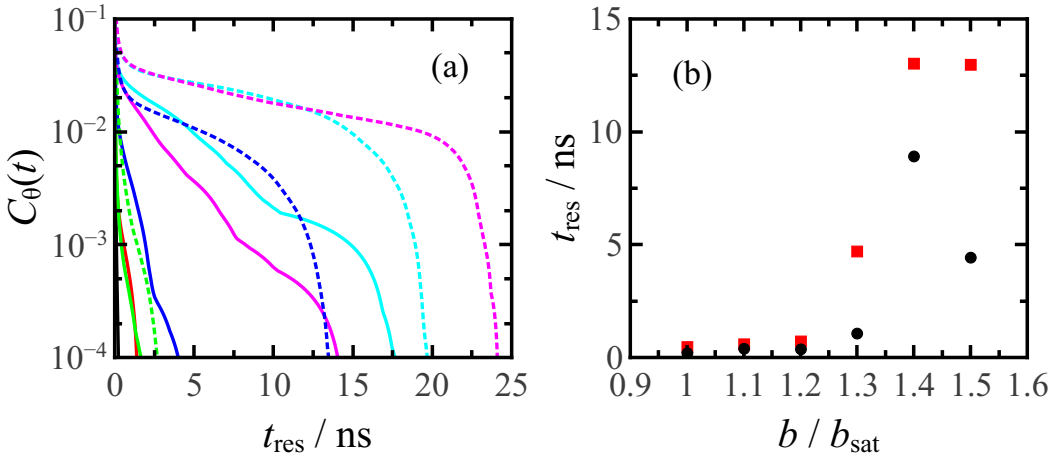

Figure 4.6: (a) Ion-association correlation function as defined in Eq. 4.7 obtained using the TWF criterion (dotted lines) and the local-order criterion (full lines) for system run at concentrations of b_{sat} (black lines), $1.1b_{\text{sat}}$ (red lines), $1.2b_{\text{sat}}$ (green lines), $1.3b_{\text{sat}}$ (blue lines), $1.4b_{\text{sat}}$ (cyan lines), and $1.5b_{\text{sat}}$ (purple lines). (b) Average cluster residence times t_{res} obtained using the TWF criterion (red squares) and the local-order criterion (black circles) at varying concentrations.

The ion-association correlation function C_θ and associated residence times t_{res} are shown in Fig. 4.6. For both the TWF and the local-order parameter criteria, the average residence time is 1 ns or less for concentrations $b \leq 1.2b_{\text{sat}}$, and more than 5 ns for $b \geq 1.4b_{\text{sat}}$. This seems to indicate that systems run with concentrations $b \leq 1.2b_{\text{sat}}$ are below simulation saturation, whereas systems run at concentrations higher than $b \geq 1.4b_{\text{sat}}$ are above the simulation saturation point. There is an evident increase between the TWF residence time at $b = 1.2b_{\text{sat}}$ ($t_{\text{res}} \simeq 0.6$ ns) and that at $b = 1.3b_{\text{sat}}$ ($t_{\text{res}} \simeq 4.7$ ns). The difference is less obvious but still present for the local-order residence time, where the residence time is $t_{\text{res}} \simeq 0.4$ ns for $b = 1.2b_{\text{sat}}$ and $t_{\text{res}} \simeq 1.1$ ns for $b = 1.3b_{\text{sat}}$. As there is a noticeable increase in the cluster residence time of ions at $b = 1.3b_{\text{sat}}$, this concentration is also assumed to be above saturation concentration. Using $b = 1.2b_{\text{sat}}$ as the maximum concentration non-crystallised system further ensures that crystals will not form spontaneously when a spherical impurity is added, and that any crystallisation witnessed is a result of the presence of the impurity or the heating thereof. Therefore, all systems run with the spherical impurities are run such that the concentration of ions in water is at $b = 1.2b_{\text{sat}}$.

4.3.3 Effects of hot impurities on the structure of aqueous sodium chloride

Solid impurity at 5293 K

Figure 4.7 shows the time evolution of the radial temperature profiles measured from the centre of mass of the carbon impurity prior to heating, and after the solid impurity has been heated to (and maintained for 10 ps at) 5293 K. The temperature $T_i(r)$ was found from the translational kinetic energy of species i at a distance r from the centre-of-mass of the impurity. First, note that a very high peak in temperature is sometimes present close to the surface of the impurity. This peak results from the small number of particles of the given species at that distance from the impurity, leading to poor statistics when calculating the translational kinetic energy. There is an evident temperature gradient in the radial temperature profiles of both ions at times $t \leq 0.4$ ns, with ions closer to the impurity having a higher temperature than those further away. This gradient is a lot less noticeable at 1.0 ns after heating, and, by that time, the temperatures of all ions are very close to the final temperature of the system. Similarly, there

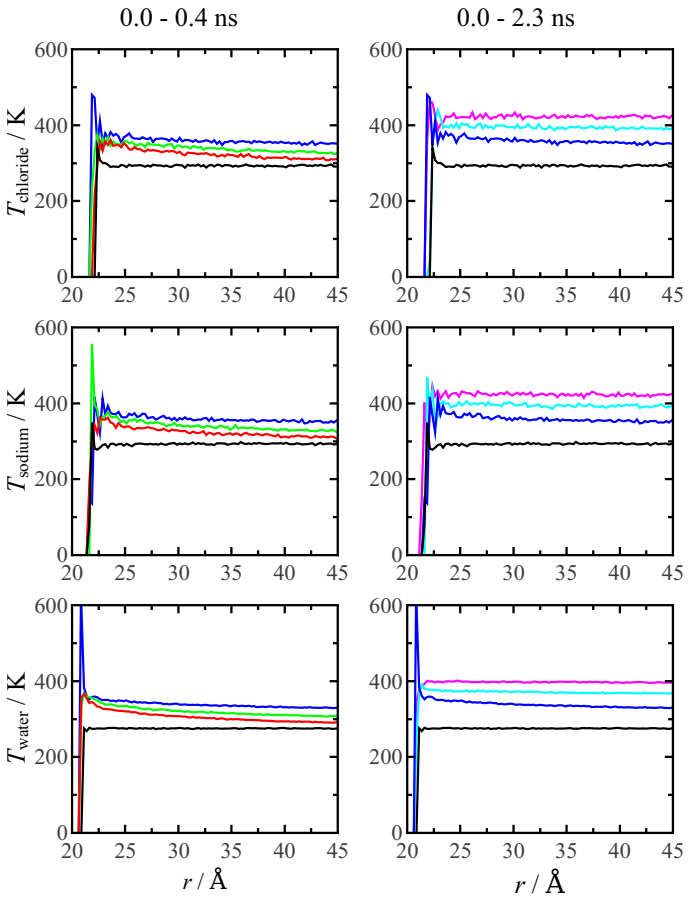

Figure 4.7: Temperature profiles of chloride ions (top), sodium ions (middle), and water (bottom) at a radial distance r from the centre of mass of the solid impurity at times after the impurity was heated to 5293 K. The temperature was derived from the translational kinetic energy. The temperature profiles are output before the impurity is heated (black line), $0.0-0.1$ ns post heating (red line), $0.1-0.2$ ns post heating (green line), $0.3-0.4$ ns post heating (blue line), $0.9-1.0$ ns post heating (cyan line), and $2.3-2.4$ ns post heating (purple line). For comparison, the profile taken $0.0-0.1$ ns and $0.3-0.4$ ns post heating are shown in both set of graphs.

exists a temperature gradient for water, with the molecules near the impurity being hotter than those further removed. The gradient is still present 1.0 ns after heating ceases, indicating that water temperature is not equilibrated. The water temperature has definitely equilibrated within 2.4 ns. Note that, while the final equilibrated temperature of the water is near 400 K, there is no sign of evaporation and the system remains in its liquid phase throughout the simulation. Furthermore, at all times shown the temperature of the ions post heating is always slightly higher than that of the water at an equivalent distance from the centre of mass of the impurity. This may indicate that the ions are better conductors of the heat generated by the impurity.

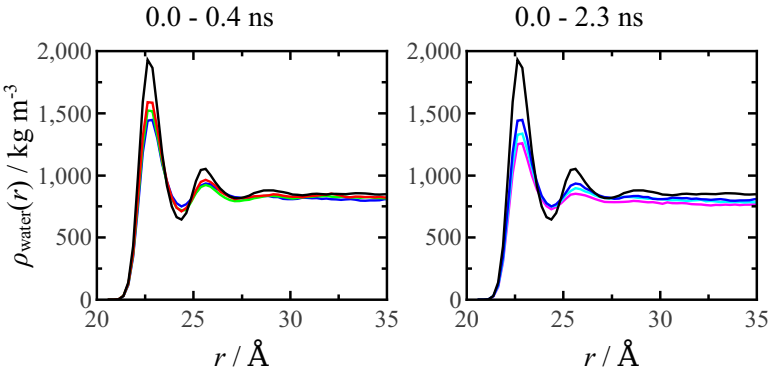

Figure 4.8: Density profiles of water at a radial distance r from the centre of mass of the solid impurity after the impurity was heated to 5293 K. The density profiles are output before the impurity is heated (black line), $0.0 - 0.1$ ns post heating (red line), $0.1 - 0.2$ ns post heating (green line), $0.3 - 0.4$ ns post heating (blue line), $0.9 - 1.0$ ns post heating (cyan line), and $2.3 - 2.4$ ns post heating (purple line).

The radial density profiles of water measured from the centre of mass of the impurity for the system prior to heating, and at given times after the solid impurity is heated to 5293 K, are shown in Fig. 4.8. Note that the radial density profiles change very little over time. There are small reductions in the heights of the first and second peaks in the radial density profiles of the water, implying that there is a reduction in the number of water molecules present in the first and second hydration shells of the carbon impurity. There are only small differences in the density profiles past the second hydration shell ($r \simeq 28$ Å), with a small decrease in long-distance density resulting from an expansion of the simulation box as the system is heated.

The ion concentration profiles measured radially from the centre of mass of the impurity are shown in Fig. 4.9. The changes in these are much more pronounced than those in the water radial density profile. Shortly after heating is finished ($t \leq 0.2$ ns), there is little change in the short-ranged ion concentration, though there is a decrease in the long-ranged concentration. For times $t \geq 0.4$ ns post heating, there is a reduction in the concentration of ions around the impurity, implying that the heat from the impurity pushes the ion particles away from the surface of the impurity, while the water molecules remain. For times $t \geq 1.0$ ns, the concentration of the ions near the impurity is much lower than it was prior to impurity-heating, while the long-distance concentration tends towards the system concentration ($b = 7.386$ mol kg^{-1}).

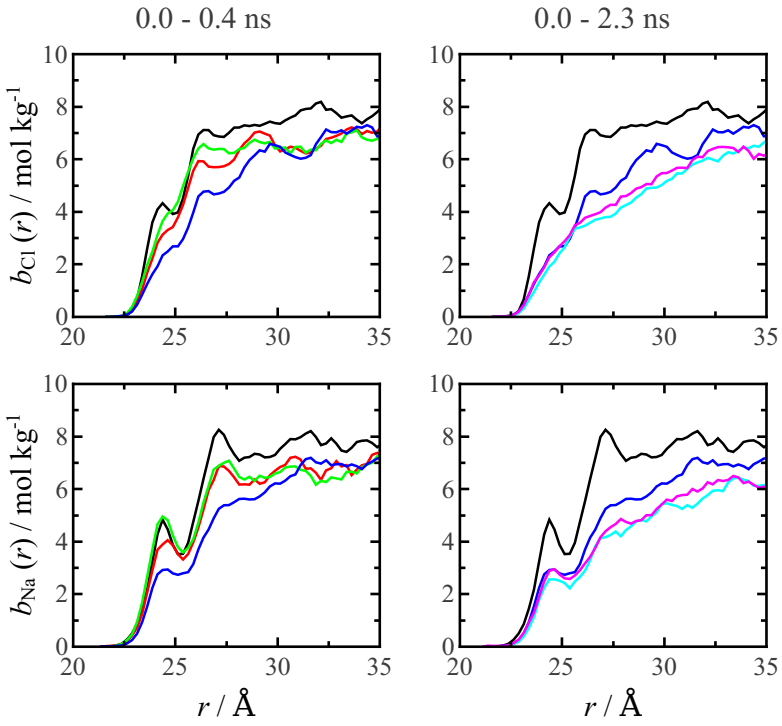

Figure 4.9: Concentration profiles of chloride (top) and sodium (bottom) ions at a radial distance r from the centre of mass of the solid impurity after the impurity was heated to 5293 K. The concentration profiles are output before the impurity is heated (black line), $0.0-0.1$ ns post heating (red line), $0.1-0.2$ ns post heating (green line), $0.3-0.4$ ns post heating (blue line), $0.9-1.0$ ns post heating (cyan line), and $2.3-2.4$ ns post heating (purple line).

Hollow impurity at 10293 K

A system containing a hollow impurity particle was simulated to discover whether heating a less massive particle of similar shape and size would have a similar effect on the system. To ensure that the systems compared are as similar as possible, the total thermal energy added to the system must be similar. The hollow impurity has nearly half the number of carbons as the solid impurity (3378 carbon particles to 5851 carbon particles) and must therefore be heated to a higher temperature. For this simulation, the impurity was heated to 10293 K and kept at this temperature for 10 ps as before.

Figure 4.10 shows the radial temperature profiles obtained from this system at times prior to and post heating. As with the solid impurity particle, there is a short-lived temperature gradient for the ions that disappears after $0.5-1.0$ ns. This feature is also present in the temperature profiles of the water molecules. Interestingly, the system seems to reach temperature equilibrium faster, with

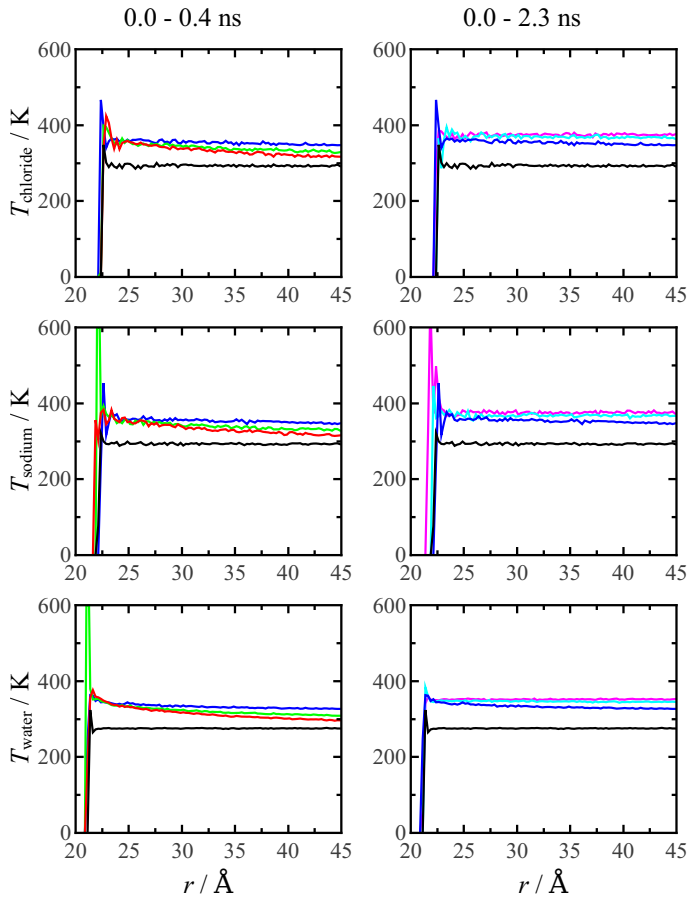

Figure 4.10: Temperature profiles of chloride ions (top), sodium ions (middle), and water (bottom) at a radial distance r from the centre of mass of the hollow impurity at various times after the particle was heated to 10293 K. The temperature was derived from the translational kinetic energy. The temperature profiles are output before the impurity is heated (black line), $0.0 - 0.1$ ns post heating (red line), $0.1 - 0.2$ ns post heating (green line), $0.3 - 0.4$ ns post heating (blue line), $0.9 - 1.0$ ns post heating (cyan line), and $2.3 - 2.4$ ns post heating (purple line).

the temperature profiles between $0.9 - 1.0$ ns being much closer in value to that calculated at $2.3 - 2.4$ ns than was seen in the system run using the solid impurity. Moreover, the final temperature to which the system equilibrates is lower than that reached with the solid impurity, even though slightly more thermal energy was given to the carbon impurity during the heating phase.

The time evolution of the radial density profiles of water is shown in Fig. 4.11. The changes in the density profiles of the water are more minor than with the solid impurity. There is a slighter reduction in the peak heights associated with the first and second hydration shell, and there is no change in the water density at long distances. This strongly suggests that heating an impurity results in a repulsion of the ions from the surroundings of the impurity, with very minor

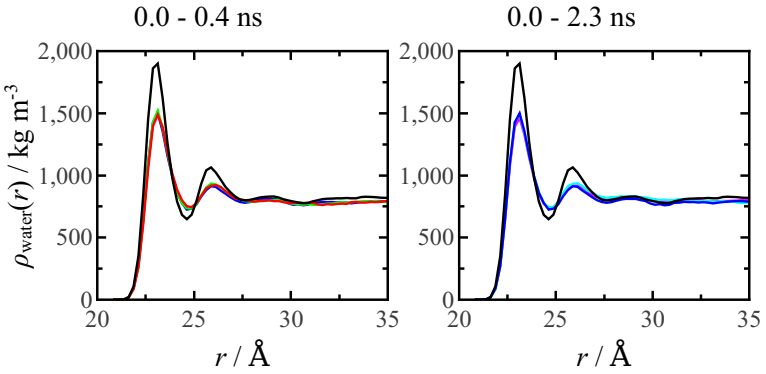

Figure 4.11: Density profiles of water at a radial distance r from the centre of mass of the hollow impurity at times after the impurity was heated to 10293 K. The density profiles are output before the impurity is heated (black line), $0.0 - 0.1$ ns post heating (red line), $0.1 - 0.2$ ns post heating (green line), $0.3 - 0.4$ ns post heating (blue line), $0.9 - 1.0$ ns post heating (cyan line), and $2.3 - 2.4$ ns post heating (purple line).

effects on the water surrounding the impurity.

The radial ion concentration profiles are shown in Fig. 4.12. These are very different from the results obtained by heating the solid impurity (Fig. 4.9). Unlike with the solid impurity, there is very little noticeable change in the concentration profile of the ions at times $t \leq 0.4$ ns post heating. For times $t \geq 0.9$ ns post heating, there is an evident reduction in concentration at all distances, with a particularly large decrease in ion concentration at a distance 25 Å $\leq r \leq$ 35 Å. This strongly suggests that the ions have, again, been displaced away from the impurity though, interestingly, the ion concentration near the impurity changes less than what was observed with the solid impurity.

This rapid expulsion of ions may explain the NPLIN process. The supersaturated system is allowed to equilibrate, with large, amorphous, pre-crystallised clusters forming randomly in solution (as discussed in Chapter 3). Some of these may form near an impurity. The laser beam acts on this impurity, causing the ions in this amorphous cluster to move quickly away from the impurity. This quick movement may cause a collision with another amorphous cluster, thereby increasing the likelihood that a crystal will form. It is even possible that this small change in ion concentration near the impurity results in a local ion concentration that is of critical size to undergo the rearrangement step of two-step nucleation, leading to a crystal forming.

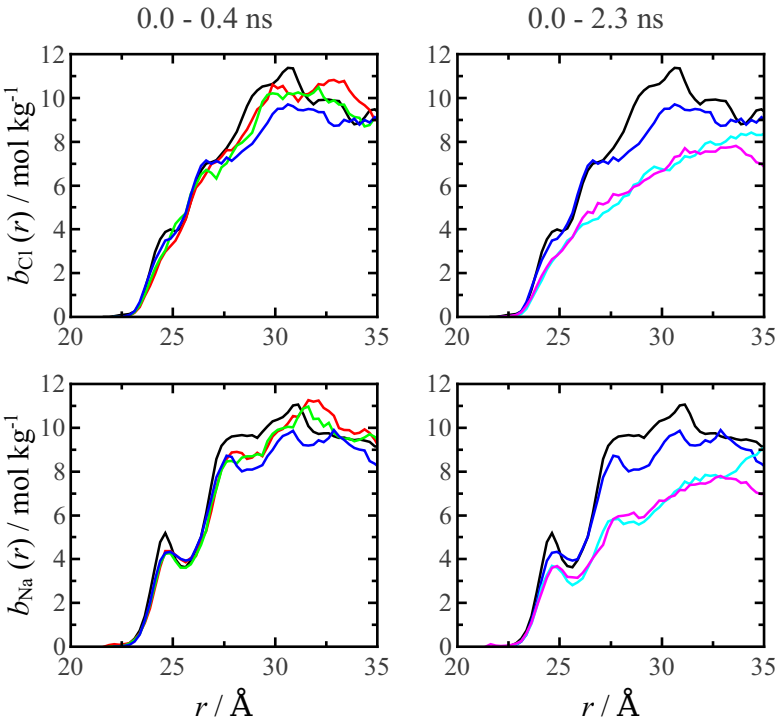

Figure 4.12: Concentration profiles of chloride (top) and sodium (bottom) ions at a radial distance r from the centre of mass of the hollow impurity at times after the impurity was heated to 10293 K. The concentration profiles are output before the impurity is heated (black line), $0.0 - 0.1$ ns post heating (red line), $0.1 - 0.2$ ns post heating (green line), $0.3 - 0.4$ ns post heating (blue line), $0.9 - 1.0$ ns post heating (cyan line), and $2.3 - 2.4$ ns post heating (purple line).

Solid impurity at 10293 K

The two systems tested so far have not had much effect on the density profiles of the water. It remains interesting to see whether the heating of an impurity could result in the formation of a nanobubble in the solution though, as the water is relatively unperturbed by the high heat of the impurity, this seems to be an unlikely mechanism for NPLIN. It does, however, remain interesting to see how the water evaporates from the surface of a spherical nanoparticle. The system run with the solid impurity heated to 5293 K was very close to reaching experimental evaporation conditions, with the system equilibrating at $T \simeq 400$ K. Therefore, by heating the impurity to 10293 K, the water should reach evaporation temperature.

Figure 4.13 shows the time evolution of the radial temperature profiles for this system. As seen before, there is a gradient in temperature for the ions at times $t \leq 0.4$ ns, though the gradient is less linear in nature and more like an exponential decay. Interestingly, the ion temperature seems to equilibrate at a similar rate

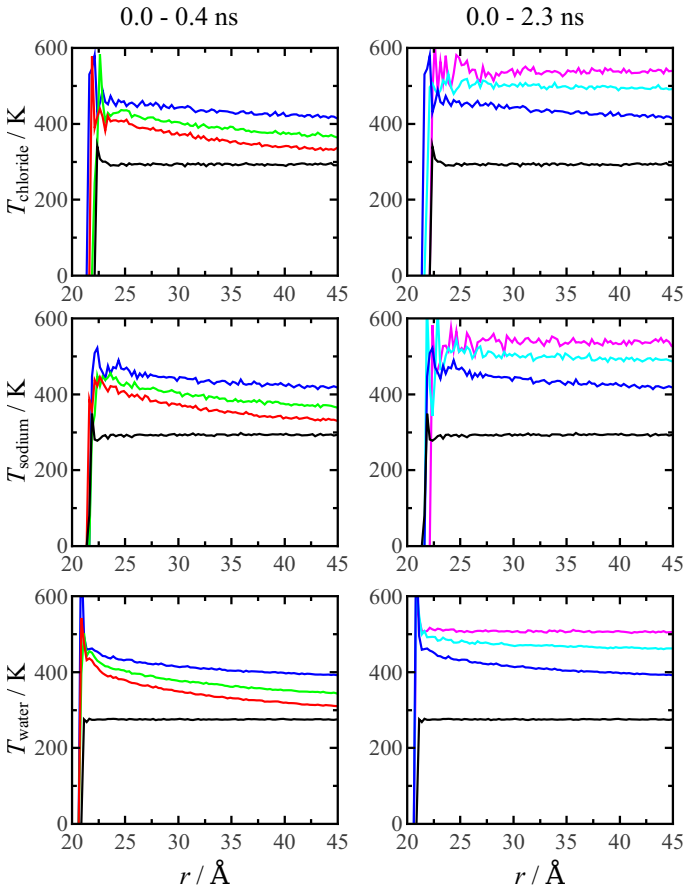

Figure 4.13: Temperature profiles of chloride ions (top), sodium ions (middle), and water (bottom) at a radial distance r from the centre of mass of the solid impurity at times after the impurity was heated to 10293 K. The temperature was derived from the translational kinetic energy. The temperature profiles are output before the impurity is heated (black line), $0.0-0.1$ ns post heating (red line), $0.1-0.2$ ns post heating (green line), $0.3-0.4$ ns post heating (blue line), $0.9-1.0$ ns post heating (cyan line), and $2.3-2.4$ ns post heating (purple line).

as seen before, with no noticeable gradient in the curves at $0.9-1.0$ ns and $2.3-2.4$ ns post heating. The equilibration temperature is, of course, higher and, as expected, the change in temperature is double that achieved with the solid impurity heated to 5293 K. The water takes longer to equilibrate than previously. Unlike with the two previous systems, there is a definite temperature gradient present $0.9-1.0$ ns post heating. The final temperature at $T \simeq 500$ K is one at which the system is expected to evaporate.

The time evolution of the radial density profiles of water is shown in Fig. 4.14. The density profile at $0.0-0.1$ ns post heating is similar in shape to the one at $2.3-2.4$ ns post heating seen in Fig. 4.14, a result of the higher thermal energy of the impurity heating the solution more quickly. For times $t \leq 0.4$ ns post heating,

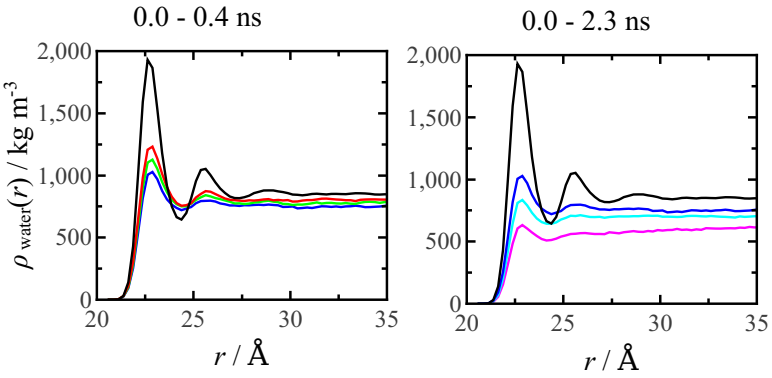

Figure 4.14: Density profiles of water at a radial distance r from the centre of mass of the solid impurity at times after the impurity was heated to 10293 K. The density profiles are output before the impurity is heated (black line), $0.0 - 0.1$ ns post heating (red line), $0.1 - 0.2$ ns post heating (green line), $0.3 - 0.4$ ns post heating (blue line), $0.9 - 1.0$ ns post heating (cyan line), and $2.3 - 2.4$ ns post heating (purple line).

there are few changes in the radial density profile. For times $t \geq 0.9$ ns, the water density found at all distances is greatly reduced. The first peak in the density profiles becomes much smaller, and the second peak disappears completely. The long-ranged density drops drastically from $\rho \simeq 800$ kg m^{-3} to $\rho \simeq 600$ kg m^{-3}. This seems indicative of water evaporation beginning to occur.

The radial ion concentration profiles are shown in Fig. 4.15. Both the first and second peaks in the concentration of ions near the impurity disappear very rapidly, with only a small first peak and no secondary peak in the sodium concentration profile and both peaks having disappeared in the chloride concentration profile by $t = 0.4$ ns. Interestingly, the ion concentrations at distances $r \geq 30$ Å remain steady for longer periods of time ($t \leq 0.4$ ns) than with the solid impurity heated to 5293 K. As the water density profile has decreased for this distance, this implies that, at this distance, ions are pushed from the vicinity of the impurity at a rate similar to water molecules. For times $t \geq 0.9$ ns, the ion concentration is drastically decreased, with the concentration at $r = 35$ Å decreased from $b(35$ Å$) \simeq 7.5$ mol kg^{-1}to $b(35$ Å$) \simeq 4.0$ mol kg^{-1}. The ion concentration decreases even with the water density having lowered. This, again, implies that the area surrounding the impurity becomes depleted of ions faster than of water.

4.3.4 Water orientation

As seen above, the first hydration shell of the impurity takes a lot of energy to disrupt. This is likely to result from the structure of the water molecules at the

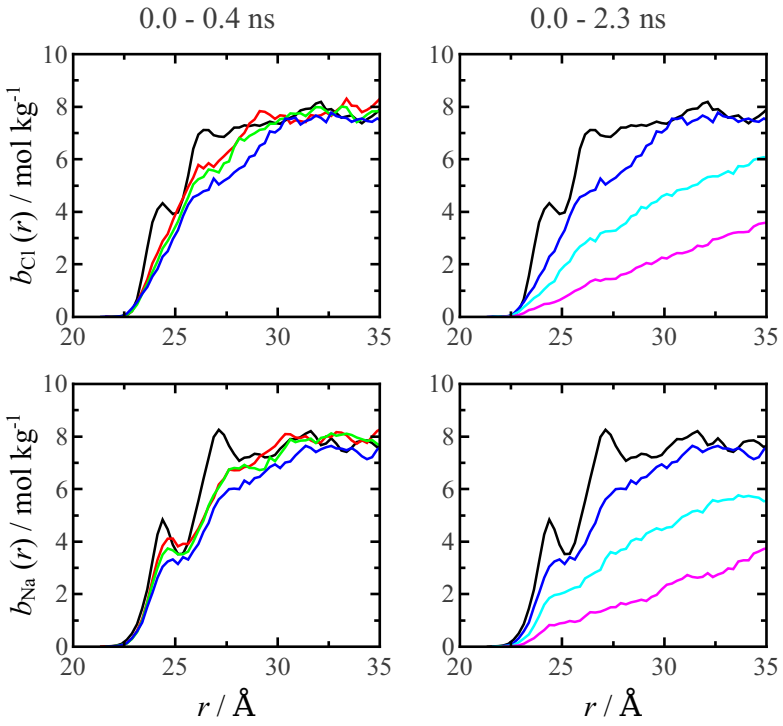

Figure 4.15: Concentration profiles of chloride (top) and sodium (bottom) ions at a radial distance r from the centre of mass of the solid impurity at times after the impurity was heated to 10293 K. The concentration profiles are output before the impurity is heated (black line), $0.0 - 0.1$ ns post heating (red line), $0.1 - 0.2$ ns post heating (green line), $0.3 - 0.4$ ns post heating (blue line), $0.9 - 1.0$ ns post heating (cyan line), and $2.3 - 2.4$ ns post heating (purple line).

liquid-impurity interface. For this size of impurity, it is possible for water to form a structure of hydrogen-bound molecules with dipole orientations perpendicular to the direction vector pointing towards the centre of mass of the impurity. This 'net' of water around the impurity would be very energetically stable. To test this theory, two order parameters are used. For a given water molecule i, both parameters are derived from the angle between the direction vector of the water dipole $\hat{\boldsymbol{\mu}}_i$ and the direction vector from the centre of mass of the impurity to the centre of mass of the oxygen $\hat{\boldsymbol{e}}_i$. The first parameter is simply obtained from the dot product of these two vectors

$$\langle \cos(\theta) \rangle = \langle \hat{\boldsymbol{\mu}}_i \cdot \hat{\boldsymbol{e}}_i \rangle. \tag{4.9}$$

where $\langle \cdots \rangle$ represents an average over molecules. If all of the dipole direction vectors are perpendicular to the water-impurity orientation vector then $\langle \cos(\theta) \rangle = 0$. This is also true when dipole orientations are completely uncorrelated with

water-impurity orientations, or when dipole orientations are arranged such that half of the dipoles are facing in one direction and half are facing the opposite direction. To differentiate between these three possible scenarios, the nematic order parameter is also used [123, 124]. This parameter is defined as

$$S = \frac{1}{2}\langle 3(\hat{\boldsymbol{\mu}}_i \cdot \hat{\boldsymbol{e}}_i)^2 - 1\rangle. \tag{4.10}$$

The order parameter $S = 1$ if the water dipoles are aligned with the water-impurity orientation vector, $S = 0$ if there is no correlation between the water-impurity orientation vector and the dipole moment orientation, and $S = -1/2$ if the dipole moment orientation is perpendicular to the water-impurity orientation.

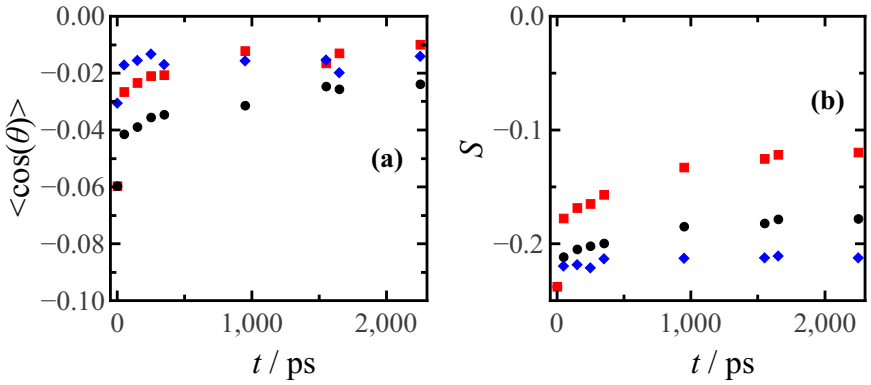

Figure 4.16: Evolution of the water orientation order parameters over time. (a) Average angle distribution, and (b) nematic order parameter calculated at the position of the first peak in the water density profiles ($r \simeq 22.5$ Å). Parameters were obtained using the solid impurity heated to 5293 K (black circles), the hollow impurity heated to 10293 K (blue diamonds), and the solid impurity heated to 10293 K (red squares). Time $t = 0$ gives the orientation obtained from the equilibration run, with all other times taken from the point at which impurity heating ceases.

Figure 4.16 shows the values of both parameters calculated at the first peak position in the water density profiles prior to heating ($t = 0$) and at times t post heating. From Fig. 4.16(a), it is evident that all systems tested have $\langle\cos(\theta)\rangle \simeq 0$ at all times. Likewise, the nematic order parameter $S < 0$ at all times tested. This strongly indicates that the water dipole orientation is perpendicular to the water-impurity orientation vector. $\langle\cos(\theta)\rangle$ is slightly more negative prior to heating than at any point post-heating, but the difference is minute and represents an average change in angle of approximately 4 °. This slight change is observed for all systems simulated. More interesting is the change in the nematic order parameter. There is almost no change in the value of S for the system run using the hollow

impurity heated to 10293 K, with there only being a small linear rise in the equivalent system run using the solid particle heated to 5293 K. The nematic order parameter for the solid impurity heated to 10293 K, however, changes drastically over time, with S increasing from $S \simeq -0.24$ prior to heating to $S \simeq -0.12$ at the end of the simulation. This increase indicates a decrease of waters with dipole orientations aligned to the water-impurity orientation vector implying that, when the water is heated to high enough temperatures, the hydrogen bonding present in the 'net' of water surrounding the impurity is broken and the water molecules can rotate more freely in space. This loss of strong structure may be one of the first signs of localised evaporation.

4.4 Conclusions

In this chapter, the effects that adding and heating a spherical carbon impurity have on the structure of a saturated aqueous sodium chloride solution were studied. To begin, two methods for finding the simulation saturation point of aqueous sodium chloride solutions were discussed. It was demonstrated that the TWF clustering criterion and the Steinhardt local-order parameter method can both accurately determine the presence of crystalline particles in solution, though the former overestimates the number of crystalline ions whereas the latter seems to underestimate them. From these clustering criteria, it is possible to calculate the residence time of ions forming a crystal. It was found that there is a noticeable increase in the ion residence time of TWF clusters when crystals form, with a less sizeable increase seen in the local-order parameter residence time. Furthermore, when using ionic parameters developed by Dang and co-workers and the TIP3P-Ewald water model, the simulation saturation point of aqueous sodium chloride appears to be 1.2 times greater than experimental saturation concentration.

The effects that adding a spherical impurity of 4 nm diameter have on structures of aqueous sodium chloride systems at saturation concentration were then studied. Water molecules were found to be closest to the surface of the impurity, with ions present only after the first hydration shell. Furthermore, heating the impurity has a stronger short- and long-ranged effect on the radial concentration profiles of the ions than on the radial density profile of the water molecules. This implies that the energy from the impurity is more easily absorbed by the ions, resulting in an increase in ion velocity and temperature. This is also evident in the temperature

profiles. In 2.4 ns, there is very little changes in the long-ranged density profiles of water when the impurity is heated to a point where it will not cause evaporation (solid impurity at 5293 K and hollow impurity at 10293 K), though there is a reduction in the occupancy of the first hydration shell of the impurity. When the impurity is heated to the point that it may cause water evaporation, the water density profiles reduces significantly but over a longer time-scale than ion evaporation. The stability of the water around the hot impurity is likely a result of the strong hydrogen bonding present at the water-impurity interface.

For all systems tested, the radial ion concentration decreased at all distances over time. This decrease must result from the heated impurity repulsing ions faster than water. It is likely that more energy is needed to break the strong intermolecular hydrogen-bonding of water than to move free ions. It is postulated that the ions pushed from the vicinity of the nano-impurity may move into randomly-occurring areas of high local ion density some distance from the impurity. The addition of ions to already highly-concentrated parts of the solution may cause crystallisation to occur. This could be the method by which NPLIN acts to induce crystallisation in aqueous salt solutions.

Chapter 5

Approximating the dipole-dipole interaction with an effective many-body interaction

5.1 Introduction

In this chapter, an attempt to model the anisotropic, long-range, dipole-dipole interaction by using an equivalent short-range, isotropic, many-body interaction is discussed. The many-body potential is derived, and a comparison of the static structure and internal energy produced by systems interacting *via* both potentials is carried out at a range of dipolar coupling strengths. To conclude, the effects that adding a three-body, chain-inducing perturbation to the Lennard-Jones potential has on the vapour-liquid phase transition are discussed.

A dipolar system is defined here as a system of particles, each of which has an electric or magnetic dipole moment. These are used to describe computationally the behaviour of systems such as ferrofluids. Ferrofluids are colloidal suspensions of magnetised nanoparticles in an inert carrier liquid. They were first patented in 1965 by Stephen Patell of the National Aeronautics and Space Administration (NASA) when he was attempting to create a magnetic fluid that would ease the ejection of spent fuel from the engines of rockets in a zero-gravity environment [22]. Ferrofluids are usually made of ferromagnetic particles composed of magnetic substances, such as iron oxide, coated with surfactants and immersed in a liquid, usually a hydrocarbon such as kerosene or paraffin [45, 125]. Their size is in the

nanometer scale. Ferrofluids are used in a wide variety of industries ranging from computer hard drive manufacture to developments of better speakers [26,126,127]. There is some speculation about the potential for using ferrofluids in developing artificial muscle tissues and hearts [39].

Theoretical and computational models of systems interacting *via* dipolar interactions have been studied in great depth for some time [26]. This is partially a result of the many unusual properties and numerous potential uses of ferrofluids, but also because of the many strange and interesting behaviours associated with them. One of the important debates surrounding the dipolar interaction is the question of whether a gas-liquid transition can arise from dipolar interactions alone. Large amounts of simulation time have been spent attempting to answer this question [128–144]. De Gennes and Pincus showed that, in the dilute limit, dipolar particles experience an attractive interaction which, when averaged over all spherical orientations, goes as $-r^{-6}$. This is exactly the form of the attractive part of the Lennard-Jones (LJ) potential [46]. De Gennes and Pincus concluded that, in the absence of a magnetic field and regardless of the strength of the dipolar interaction, a system of dipolar hard spheres (DHSs) will undergo a gas-liquid phase transition similar to the one observed in a system composed of LJ particles. Work by Weis and Levesque, however, showed that, by increasing the dipolar coupling constant of a dipolar soft sphere system, ordered structures such as chains will form, even in the absence of a magnetic field. This phenomenon is not observed in LJ systems [47, 48]. The formation of chains in dipolar gases is thought to pre-empt and prevent condensation [142–144], but this is still being debated and it remains unclear whether the chain-forming ability of a system precludes the existence of a condensation phase transition.

In the 1970s, Stell and co-workers showed that there is a one-to-one mapping between the partition function of a fluid with anisotropic, long-range, dipole-dipole interactions and that of a hypothetical fluid with isotropic, many-body interactions [145–147]. It is very likely that simulating a dipolar fluid as a fluid with many-body interactions could significantly reduce computational time for large systems. This speed up would result from only needing to simulate short-ranged, many-body interactions rather than long-ranged dipolar interactions. It would be possible to truncate these many-body interactions and to produce neighbour lists that would further speed up the force and energy calculations. Both of these methods are commonly used in molecular dynamics (MD) and Monte Carlo (MC) algorithms.

The first order, two-body expansion of the dipole-dipole interaction discussed by de Gennes and Pincus is likely to be a very good approximation for weakly interacting dipolar systems and these systems will condense in much the same way as a LJ system [46]. As the strength of the dipolar interaction is increased, however, this approximation breaks down. The formation of structures such as chains and rings in the dilute gas phase may impede the condensation driven by the LJ-type interaction. Expanding the dipole-dipole interaction beyond the two-body contribution may result in the recovery of the terms favouring the formation of chains and rings when the strength of the dipolar interaction is large with respect to the thermal energy. Furthermore, by separating the terms contributing to the formation of chains from the terms favouring condensation, it becomes possible to alter the relative importance of the chain-forming terms, thereby making it possible to form chains 'on demand' and to study the effects of increasing the strength of chaining on a vapour-liquid phase transition. The degree of chaining would become an easily varied simulation parameter, like the strength of the LJ interaction or the temperature of the system, and the effects of chain formation on a system would be as easy to study as any other such variable.

In this chapter the structures resulting from a fluid composed of dipolar soft spheres (DSSs) will be compared with those in an equivalent hypothetical fluid with only the leading-order two- and three-body interactions. It is demonstrated by very simple arguments that the leading-order three-body interaction favours chain formation, whereas the two-body interaction favours condensation in the form of liquid-like compact clusters. From this, the static structures of the two systems are compared as the density and coupling constant are varied. Then, it is shown that the structures observed using the many-body system are very similar to those observed in DSS systems run at the same temperature. To conclude, the effects that varying the three-body coefficient have on the evolution of the gas-liquid phase diagram of the many-body fluid are discussed.

5.2 Model

The two-body anisotropic dipole-dipole interaction is defined as

$$u_{ij}(\boldsymbol{r}_i, \boldsymbol{r}_j, \boldsymbol{\mu}_i, \boldsymbol{\mu}_j) = \frac{(\boldsymbol{\mu}_i \cdot \boldsymbol{\mu}_j)}{r_{ij}^3} - \frac{3(\boldsymbol{\mu}_i \cdot \boldsymbol{r}_{ij})(\boldsymbol{\mu}_j \cdot \boldsymbol{r}_{ij})}{r_{ij}^5} \tag{5.1}$$

where $\boldsymbol{\mu}_i$ is the dipole moment on particle i, $\boldsymbol{r}_{ij} = \boldsymbol{r}_j - \boldsymbol{r}_i$ is the interparticle separation vector, and $r_{ij} = |\boldsymbol{r}_{ij}|$ is the interparticle distance. The total dipolar energy is given by $U = \sum_{i<j}^{N} u_{ij}$. It has been shown that there is a one-to-one map between the partition function of this potential and that of an isotropic, many-body potential [145]. The many-body potential is found by integrating out the dipole orientations at inverse temperature $\beta = 1/k_{\mathrm{B}}T$. The resulting interaction energy takes the form

$$\Psi = \sum_{i<j}^{N} \psi_2(\boldsymbol{r}_i, \boldsymbol{r}_j) + \sum_{i<j<k}^{N} \psi_3(\boldsymbol{r}_i, \boldsymbol{r}_j, \boldsymbol{r}_k) + \ldots \tag{5.2}$$

For a one-component fluid in which $\mu = |\boldsymbol{\mu}|$ for each particle, the leading-order terms in the two-body and three-body interactions from Eq. 5.2 are

$$\beta\psi_2(\boldsymbol{r}_i, \boldsymbol{r}_j) = -\frac{(\beta\mu^2)^2}{3r_{ij}^6} \tag{5.3}$$

$$\beta\psi_3(\boldsymbol{r}_i, \boldsymbol{r}_j, \boldsymbol{r}_k) = \frac{(\beta\mu^2)^3}{9}\left[\frac{1}{r_{ij}^3 r_{jk}^3 r_{ki}^3} + \frac{3(\boldsymbol{r}_{ij}\cdot\boldsymbol{r}_{ik})(\boldsymbol{r}_{ji}\cdot\boldsymbol{r}_{jk})(\boldsymbol{r}_{ki}\cdot\boldsymbol{r}_{kj})}{r_{ij}^5 r_{jk}^5 r_{ki}^5}\right]. \tag{5.4}$$

Further terms in this expansion will be of shorter range and will be ignored. By substituting the dipole moment with the dipolar coupling constant $\lambda = \beta\mu^2/\sigma^3$, where σ is the particle diameter, Eqs. 5.3 and 5.4 can be rewritten in the form

$$\beta\psi_2(\boldsymbol{r}_i, \boldsymbol{r}_j) = -\frac{\lambda^2}{3}\left(\frac{\sigma}{r_{ij}}\right)^6 \tag{5.5}$$

$$\beta\psi_3(\boldsymbol{r}_i, \boldsymbol{r}_j, \boldsymbol{r}_k) = \frac{\lambda^3}{9} f_3(\boldsymbol{r}_i, \boldsymbol{r}_j, \boldsymbol{r}_k) \tag{5.6}$$

$$f_3(\boldsymbol{r}_i, \boldsymbol{r}_j, \boldsymbol{r}_k) = \frac{\sigma^9}{r_{ij}^3 r_{jk}^3 r_{ki}^3}\left[1 + \frac{3(\boldsymbol{r}_{ij}\cdot\boldsymbol{r}_{ik})(\boldsymbol{r}_{ji}\cdot\boldsymbol{r}_{jk})(\boldsymbol{r}_{ki}\cdot\boldsymbol{r}_{kj})}{r_{ij}^2 r_{jk}^2 r_{ki}^2}\right]. \tag{5.7}$$

This substitution results in the two-body interaction resembling the attractive part of the LJ interaction and the three-body interaction resembling the Axilrod-Teller (AT) interaction [148]. Furthermore, it emphasises that the three-body potential acts like a perturbation on the two-body term. This is the equivalent to taking all perturbations λ of order 3 or less. It seems natural to define $\lambda^2/3 = 4\beta\epsilon$ as this will result in Eq. 5.5 reproducing the attractive part of the LJ potential (in units $k_{\mathrm{B}}T$). A short-range repulsion of the form $4\beta\epsilon(\sigma/r_{ij})^{12}$ can be introduced, making it possible to rewrite the total two-body interaction as a LJ interaction. It follows that the equivalent dipolar system would be a system of dipolar soft spheres, for which the energy of two interacting particles will be the sum of

the short-ranged repulsion $4\epsilon(\sigma/r_{ij})^{12}$ and the dipole-dipole interaction given by Eq. 5.1.

Similarly, the three-body prefactor can be rewritten as $\beta\nu = \lambda^3/9$. In reduced units, the temperature can be written as $T^* = k_{\mathrm{B}}T/\epsilon$. As shown above, $\epsilon = \lambda^2/12\beta$, therefore by substitution, $T^* = 12/\lambda^2$. With this, it is possible to define the three-body energy solely in terms of a reduced temperature. Eqs. 5.5 and 5.6 can be rewritten as:

$$\beta w_2(\boldsymbol{r}_i, \boldsymbol{r}_j) = \frac{4}{T^*}\left[\left(\frac{\sigma}{r_{ij}}\right)^{12} - \left(\frac{\sigma}{r_{ij}}\right)^{6}\right] \tag{5.8}$$

$$\beta w_3(\boldsymbol{r}_i, \boldsymbol{r}_j, \boldsymbol{r}_k) = \beta\nu f_3(\boldsymbol{r}_i, \boldsymbol{r}_j, \boldsymbol{r}_k) \tag{5.9}$$

$$\beta\nu = \frac{1}{9}\left(\frac{12}{T^*}\right)^{3/2} = \left(\frac{a}{T^*}\right)^{3/2}. \tag{5.10}$$

where $a = 4/\sqrt[3]{3}$.

Thus, the two systems that will be compared are the DSS system with total potential energy $U = \sum_{i<j}^{N} u_{ij}$, where

$$u_{ij}(\boldsymbol{r}_i, \boldsymbol{r}_j, \boldsymbol{\mu}_i, \boldsymbol{\mu}_j) = 4\epsilon\left(\frac{\sigma}{r_{ij}}\right)^{12} + \frac{(\boldsymbol{\mu}_i \cdot \boldsymbol{\mu}_j)}{r_{ij}^3} - \frac{3(\boldsymbol{\mu}_i \cdot \boldsymbol{r}_{ij})(\boldsymbol{\mu}_j \cdot \boldsymbol{r}_{ij})}{r_{ij}^5} \tag{5.11}$$

and an effective many-body (EMB) system whose potential energy is defined as

$$U = \sum_{i<j}^{N} w_2(\boldsymbol{r}_i, \boldsymbol{r}_j) + \sum_{i<j<k}^{N} w_3(\boldsymbol{r}_i, \boldsymbol{r}_j, \boldsymbol{r}_k). \tag{5.12}$$

When $a = 0$, the EMB potential is simply the LJ potential. The three-body AT potential has a temperature dependent prefactor ($\nu = \epsilon a^{3/2}/T^{*1/2}$). This is fundamentally different from other work using the AT potential, where this potential was used to simulate the three-body interaction arising from the atomic polarisablity in rare-gas environments, and was therefore independent of temperature [149–151].

Fig. 5.1(a) shows that the two-body LJ part of the potential energy favours the formation of compact liquid-like clusters whereas the three-body interaction favours the formation of chains. Decreasing the temperature while keeping a constant leads to the three-body prefactor increasing. The chaining effect of the AT potential eventually becomes the dominant term and it results in chain

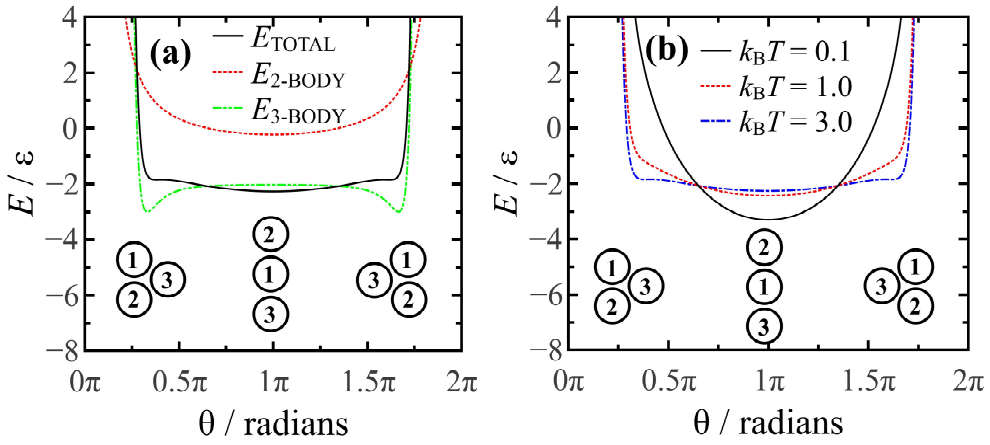

Figure 5.1: Evolution of the potential energy of a system of three particles where two of the particles are fixed at a distance $r = 2^{1/6}\sigma$ from a central particle. One of the outer particles is allowed to rotate circularly about the centre particle, while the third particle remains fixed. The energy is calculated at varying internal angle θ. (a) shows the two-body (red dashed line) and three-body (green dotted line) contribution to the total potential energy and the total potential energy (black full line) at $T^* = 3.0$ with $a = 4/\sqrt[3]{3}$. (b) shows the total EMB potential as the temperature is varied with $a = 4/\sqrt[3]{3}$. The configurations of the three particles at internal angles $\theta = \frac{\pi}{3}, \pi, \frac{5\pi}{3}$ are shown below each graph.

formation being favoured [Fig. 5.1(b)]. Likewise, it is possible to increase the importance of the chain forming part of the potential by increasing the value of a at fixed temperature.

It is worth emphasising that, when defining the two-body prefactor, the dipolar coupling constant was defined as $\lambda = \mu^{*2}/T^*$ and $\lambda^2 = 12/T^*$. These coupled equations allow us to define equivalent DSS and EMB systems by choosing the coupling constant at which both systems are simulated.

5.3 Simulation methods

Molecular dynamics (MD) simulations of DSS systems were carried out using the LAMMPS package [50]. $N = 512$ particles interacting *via* pairwise interactions given by Eq. 5.11 were simulated inside a cubic box with periodic boundary conditions (PBCs) at densities $\rho^* = \rho\sigma^3 = 0.007$, 0.100, and 0.450. The reduced temperature T^* and dipole moments μ^* are both determined from the dipolar coupling constant λ, with $T^* = 12/\lambda^2$ and $\mu^{*2} = \lambda/T^*$. The simulations were run

in the canonical ensemble (constant NVT) and time integration was performed using the velocity-Verlet algorithm. The soft-sphere interactions were truncated and shifted at a distance of $L/2$, where L is the length of the sides of the box, and the dipole-dipole interactions were calculated *via* the Ewald summation method with conducting boundary conditions. The time step used varied in the range $0.0001 \leq \delta t^* \leq 0.01$ depending on the density of the system and the strength of the dipolar coupling. An equilibration run of $t^* = 10000$ was performed. This was followed by a production run in which particle positions and dipole orientations were output at intervals $\Delta t^* = 10$, with a total of 1000 outputs per run to determine the static structure of the system. Doing this ensured that the errors associated with the results were kept small, and that errors and uncertainties fell in the regime described in Section 2.7.4.

The EMB systems were simulated using canonical-ensemble Monte Carlo (CMC) methods. $N = 512$ particles interacting *via* the EMB potential described in Eq. 5.12 were placed in a box with PBCs at densities $\rho^* = 0.007$, 0.100, and 0.450. The two-body potential was truncated and shifted at a distance of $L/2$. The three-body potential was calculated with a fixed three-body coefficient $a = 4/\sqrt[3]{3}$ and was truncated at a distance of $L/2$. No long-ranged corrections were applied. One MC sweep consisted of attempted moves equal to the number of particles, with the particle moved chosen at random. 50 blocks of 1000 sweeps were run. The maximum displacement was chosen such that the acceptance rate was as close to 50% as possible for a displacement in the range $\sigma/2 \leq \delta r^* \leq L/2$. It should be noted that at low values of λ, the low-density acceptance rate was very high regardless of the maximum displacement allowed. Similarly, at very high values of λ, the acceptance rate would tend to zero once arrested structures had started forming. The systems were allowed to equilibrate for 25 blocks, though the energy of the system had plateaued before this. Particle positions were output every 50 sweeps post-equilibration for a total of 500 outputs. Doing this ensured that the errors associated with the results were kept small, and that errors and uncertainties fell in the regime described in Section 2.7.4.

The gas-liquid phase diagram for the EMB potential was found by using grand canonical Monte Carlo (GCMC) methods. Histogram reweighing was used to find the gas and liquid coexistence densities at given values of the three-body coefficient a and temperature T^* [152, 153]. Particles were placed in a cubic box with PBCs. The length of the sides of the box varied in the range $7.0 \leq L^* \leq 12.0$. This allowed for more accurate coexistence results to be obtained

as chaining became more prevalent. The two-body and three-body contributions were truncated at a cutoff $r_c = 2.5\sigma$. Only insertion and deletion moves were allowed. The number of attempted moves per sweep was equal to the number of particles that would be in the box at $\rho^* = 0.3$, a density close to the critical density of the LJ fluid. 10000 MC sweeps were made per block, and 100 blocks were run. Each block, the density probability distribution function was calculated. From this function, a biasing potential was created to bias subsequent blocks to sample different densities. Eventually, the contribution of the biasing potentials will push the system into a gas-liquid coexistence state. When the system had equal probability of being in the gas phase as in the liquid phase, coexistence had been reached. The gas and liquid densities at coexistence were found from the average density of the respective peak in the bimodal probability distribution. The critical density ρ_c and temperature T_c were obtained by fitting the coexistence densities to the equations:

$$\rho_{\pm} = \rho_c + At \pm Bt^{\beta} \tag{5.13}$$

$$t = \frac{|T - T_c|}{T_c} \tag{5.14}$$

where $\beta = 0.326$ is the three-dimensional Ising order-parameter exponent which Stell showed to be appropriate for this system due to the interactions being long ranged [145].

5.4 Results and discussions

5.4.1 Comparison of the structure of the EMB and DSS systems

To begin, the effects of increasing the dipolar coupling constant λ on the structure obtained in the DSS system are studied. Figure 5.2 shows simulation snapshots of the DSS and EMB systems at fixed density $\rho^* = 0.007$ and $\lambda = 1.0$, 2.0, 5.0, 10.0, and 20.0. Previous work has suggested that chaining should be observed in DHS systems with a coupling constant $\lambda \geq 4.0$ for $\rho^* \leq 0.05$ [154]. It follows that there should be evident chaining in the DSS systems with $\lambda = 10.0$ and $\rho^* = 0.007$. This is clearly not the case. The fact that very little chaining is observed for the DSS systems when $\lambda = 10.0$ results from the use of soft-spheres rather than hard-

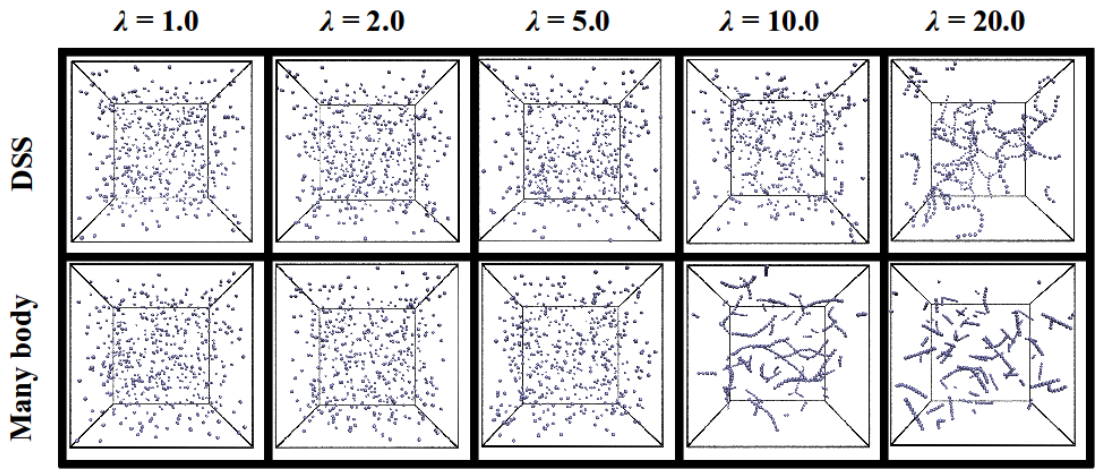

Figure 5.2: Simulation snapshots of DSS systems and the equivalent EMB systems at $\rho^* = 0.007$ as the dipolar coupling constant λ is increased.

spheres. The effective dipolar coupling constant for soft-spheres will, in general, be less than the parameter λ because the lowest-energy distance between a pair of particles will be greater than σ due to the soft-sphere repulsion. Two ways of correcting for this are the Barker-Henderson scheme [61] and a method based on the minimum of the dipolar pair potential.

In the Barker-Henderson scheme, the effective hard-sphere diameter d for the soft-sphere repulsion $4\epsilon(\sigma/r)^{12}$ is given by

$$d = \sigma \left(\frac{4}{T^*}\right)^{1/12} \Gamma\left(\frac{11}{12}\right). \tag{5.15}$$

where $\Gamma(11/12) = 1.0555$. The effective dipolar coupling constant is therefore given by

$$\lambda_{\mathrm{BH}} = \frac{\mu^2}{k_{\mathrm{B}} T d^3} = \lambda \left(\frac{\sigma}{d}\right)^3. \tag{5.16}$$

Alternatively, the minimum energy u_0 in the DSS pair potential [Eq. 5.11] can be associated with the nose-to-tail parallel arrangement of dipolar hard spheres. The lowest-energy conformation of a pair of DSSs, with the dipoles aligned parallel nose-to-tail ($\rightarrow\rightarrow$), is given by

$$\frac{u_0}{k_{\mathrm{B}} T} = \frac{4}{T^*}\left(\frac{\sigma}{r_0}\right)^{12} - 2\lambda\left(\frac{\sigma}{r_0}\right)^3 = -\frac{3}{4}\lambda^{4/3}(T^*)^{1/3} \tag{5.17}$$

with

$$r_0 = \sigma\left(\frac{8}{\lambda T^*}\right)^{1/9}. \tag{5.18}$$

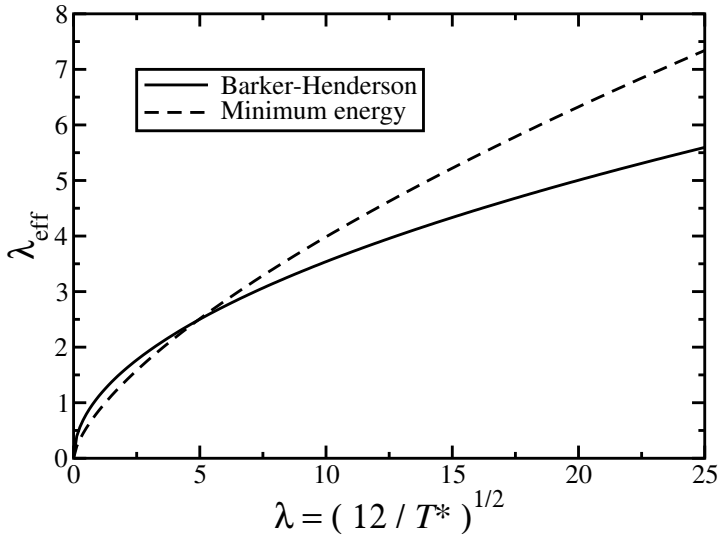

Figure 5.3: Effective dipolar coupling constant $\lambda_{\rm eff}$ of the DSS fluid as a function of $\lambda = \sqrt{12/T^*}$, using the Barker-Henderson route [Eq. 5.16] (solid line) and a minimum-energy criterion [Eq. 5.19] (dashed line).

This would lead to the effective coupling constant being

$$\lambda_\mu = -\frac{u_0}{2k_{\rm B}T} = \frac{3}{8}\lambda^{4/3}(T^*)^{1/3}. \tag{5.19}$$

The two formulations of the effective dipolar coupling constant are compared in Fig. 5.3 as a function of $\lambda = \sqrt{12/T^*}$. Using these as the effective coupling constant for this DSS system, it follows that when $\lambda = 10.0$, $\lambda_{\rm BH} = 3.53$ and $\lambda_\mu = 3.98$. Both of these are below the threshold $\lambda > 4.0$, above which chaining is expected to be evident.

For values of $\lambda \leq 5.0$, there is no evident difference in the simulation snapshots produced from the DSS systems and the equivalent EMB systems. This can be observed in the low-density snapshots in Fig. 5.2 and is confirmed for all densities tested by the near overlap in the radial distribution functions (RDFs) [Fig. 5.4] and the structure factors [Fig. 5.5] obtained from the two systems. There is no difference in the RDFs of DSS systems at $\lambda = 1.0, 2.0$ with $\rho^* = 0.007$, 0.100, 0.450, and the RDFs from the equivalent MB systems. As λ is increased to 5.0, differences in the RDFs and structure factors become apparent, but these are quite small and should not result in any great discrepancies between the structures observed in equivalent systems run using either potential. Given the definition of λ, this is equivalent to saying that, when the dipolar coupling strength is no more than one order of magnitude greater than the thermal energy, the EMB system is able to reproduce the structure observed in a DSS system quite well for

all densities tested. It is worth noting that the vast majority of experimentally created ferrofluids have a dipolar strength constant $\lambda \lesssim 2.0$ (with some work published using ferrofluids with $\lambda \simeq 10.0$ [45,125]). The EMB fluid is therefore a very good model for experimentally achievable systems.

Increasing λ to higher values ($\lambda = 10.0,\ 20.0$) leads to noticeable differences between the structures of DSS particles and those of EMB particles. At $\rho^* = 0.007$, $\lambda = 10.0$, long chains are observed in the simulation snapshots of the system of EMB particles whereas, in the equivalent system of DSS particles, it is rare to find more than four particles aligned [Fig. 5.2]. As the dipolar coupling constant is increased to $\lambda = 20.0$, long chains can be observed in the simulation snapshot of the DSS system at $\rho^* = 0.007$, but these chains appear much less rigid than those observed in the equivalent EMB system [Fig. 5.2]. This implies that chain-forming interactions are stronger in the EMB systems than they are in the DSS systems. Differences in the structures of systems run using different interaction potentials are observable in the RDFs [Fig. 5.4] and structure factors [Fig. 5.5] as well. This is a general effect seen across all densities tested at these high values of λ. It can also be seen that the peaks in the RDFs of the EMB systems at high values of coupling constants are sharper and of greater magnitude than the peaks occurring in the RDFs of equivalent DSS systems [Fig. 5.4]. The centres of these peaks are consistently at smaller distances in the EMB systems than those in the DSS systems. This indicates that, with high values of λ, the EMB interaction results in particles having smaller effective radii than particles interacting *via* the equivalent DSS potentials. Furthermore, there is more long-ranged order apparent in the RDFs of the EMB systems than in those of the DSS systems at all densities and concentrations tested, with the exception of the DSS system run at $\rho^* = 0.450$, $\lambda = 20.0$ [Fig. 5.5].

The systems at $\rho^* = 0.450$, $\lambda = 20.0$ exhibit some interesting structures. It is clear from the RDF and structure factor that the DSS system is crystalline. The RDF shows the distinctive repeating features [Fig. 5.4] and the presence of Bragg peaks is evident in the structure factor [Fig. 5.5]. Though crystallisation is unusual at such a low number density, it is simple to show that this arises from the use of the dipolar soft-sphere interaction. As shown in Eq. 5.18, the lowest-energy conformation for a pair of dipoles occurs at a distance $r_0 = \sigma(8/\lambda T^*)^{1/9}$. This distance can be used to approximate the effective particle diameter of the DSS particles. It follows that, at $\lambda = 20.0$ and $T^* = 0.03$, the effective particle diameter $r_0 = 1.33\sigma$, meaning that the effective density of the system is $\rho r_0^3 =$

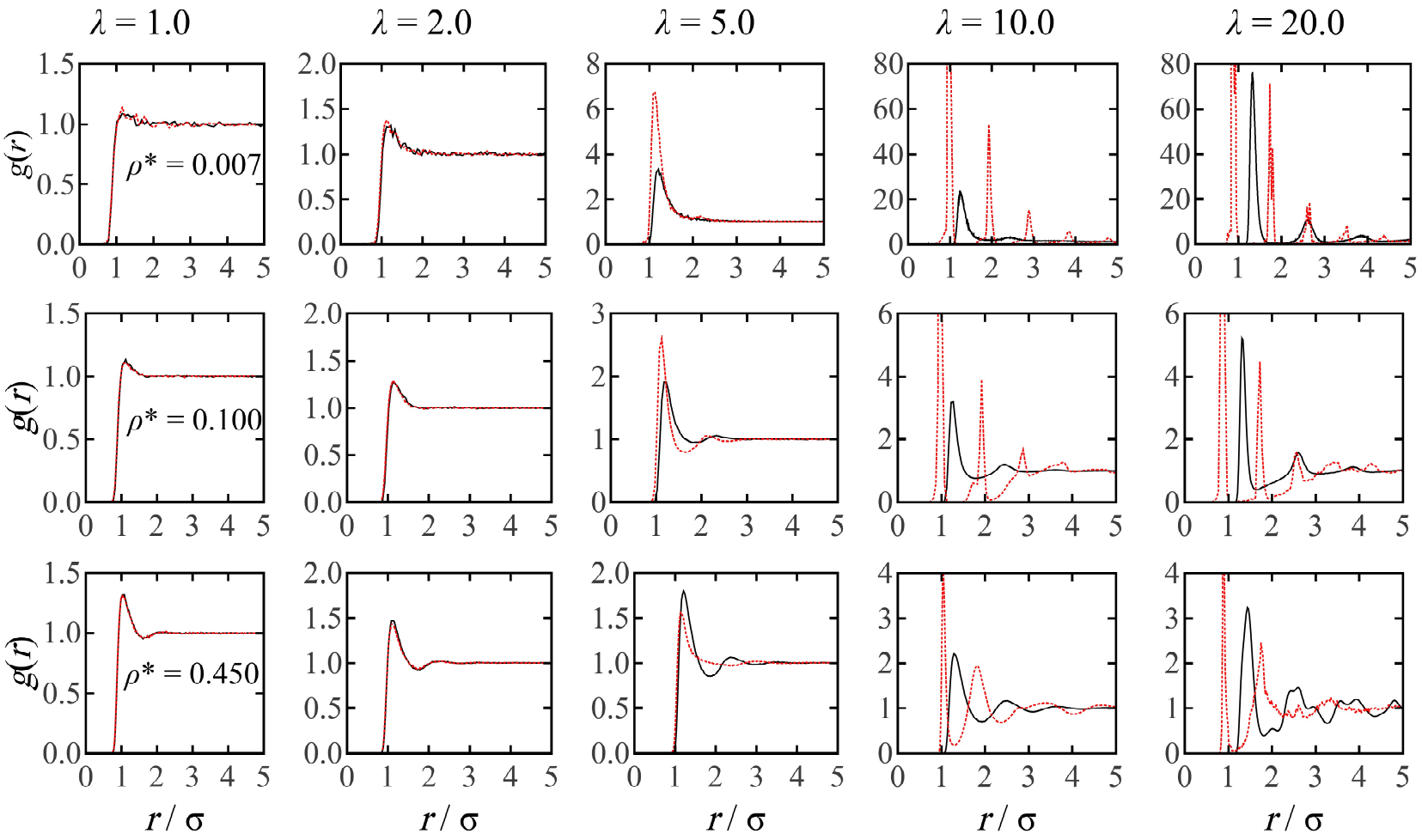

Figure 5.4: Radial distribution functions $g(r)$ of systems with DSS (black full line) and EMB (red dashed line) potentials at $\lambda = 1.0$, 2.0, 5.0, 10.0, and 20.0 at densities $\rho^* = 0.007$, 0.100, and 0.450.

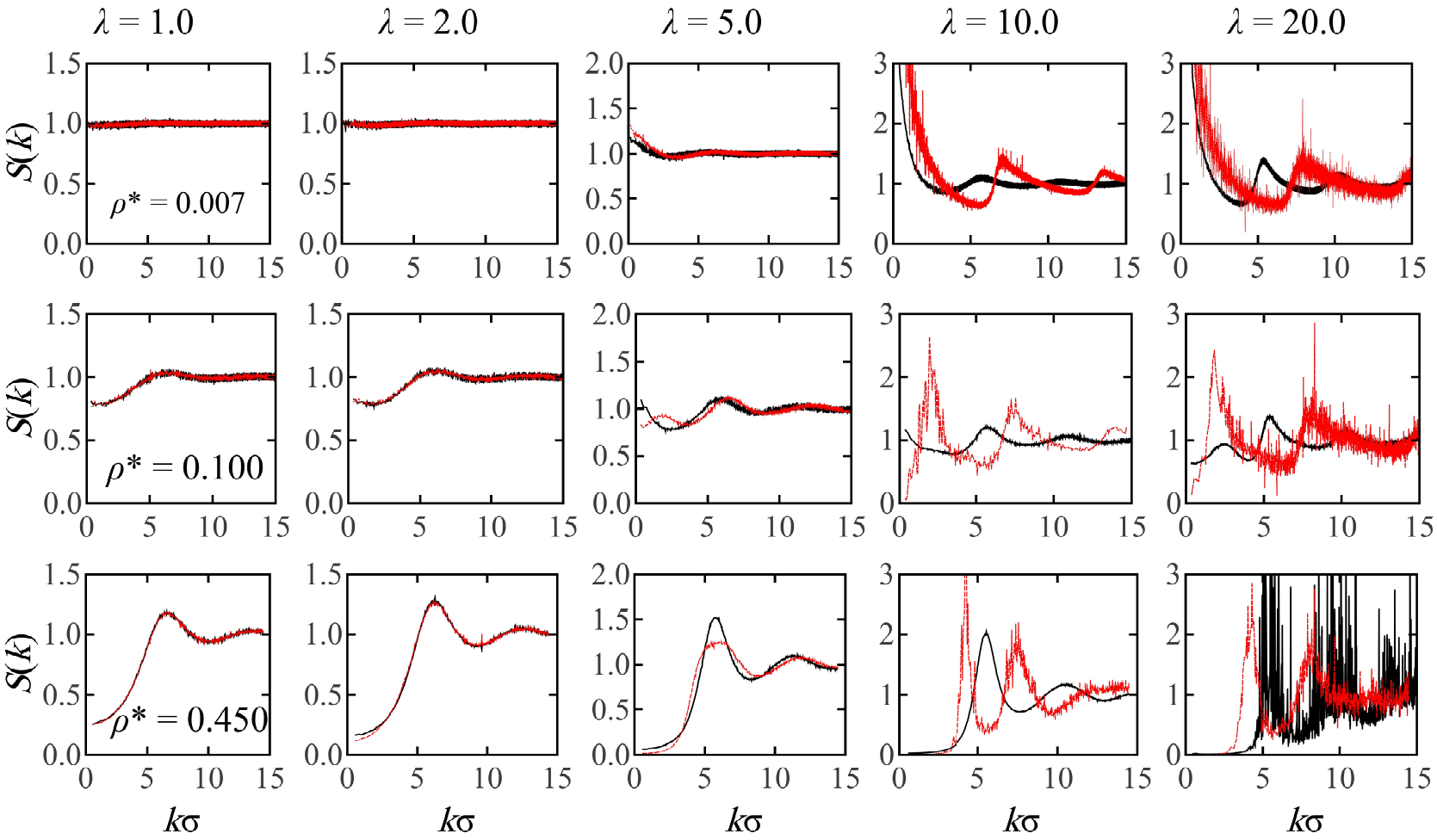

Figure 5.5: Structure factors $S(k)$ of DSS systems (black solid line) and equivalent EMB systems (red dashed line) at $\lambda = 1.0$, 2.0, 5.0, 10.0, and 20.0 at densities $\rho^* = 0.007$, 0.100, and 0.450.

1.06, above the reduced density at which hard spheres freeze ($\rho\sigma^3 = 0.94$) and melt ($\rho\sigma = 1.04$) [61]. An equivalent effect is not seen with the EMB system as the effective particle diameters, and the effective system density, remain constant at $r_0 \simeq \sigma$.

5.4.2 Internal energy

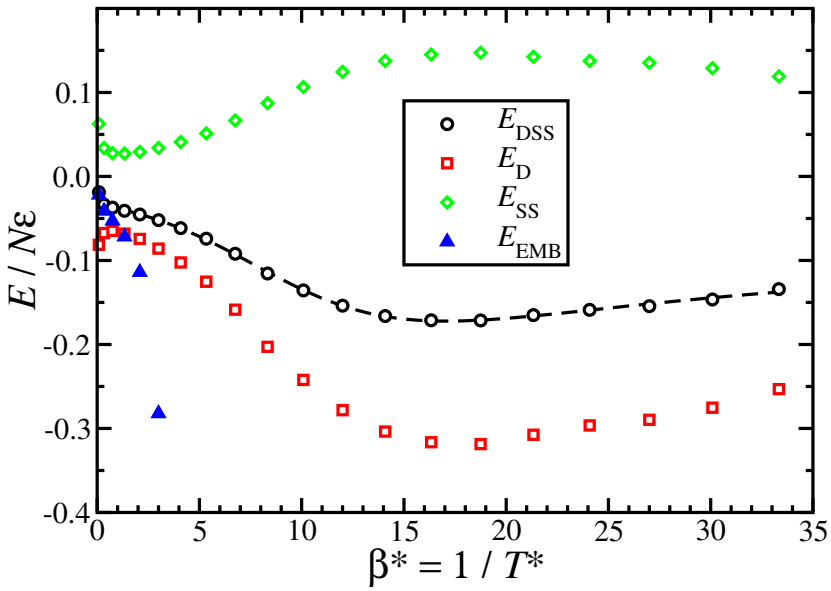

Figure 5.6: Configurational part of the internal energy E of the DSS and EMB systems plotted against the inverse reduced temperature β^*. The soft-sphere (SS) and dipolar (D) contributions to the DSS configurational free energy are also shown. The black dashed line is a fit to the DSS internal energy using a [2/2] Padé approximant of β. All data shown are for $\rho^* = 0.007$.

Given that the EMB potential is an approximate many-body expansion of the DSS potential with respect to λ, it should follow that the internal energies in both systems are similar only for low values of λ. The systems under consideration here have λ defined as being a function of T^*. This leads to T^* and μ^* no longer being independent of one another, effectively making the DSS potential equation [Eq. 5.1] temperature dependent. This potential energy should therefore be viewed as an effective free energy rather than as an internal energy, with the entropic part resulting from having integrated out the orientations. The internal energy is defined as

$$E = \left\langle \frac{\partial(\beta U)}{\partial \beta} \right\rangle_{N,V} \tag{5.20}$$

where $\beta = 1/k_{\mathrm{B}}T$ is the inverse temperature and U is the system potential energy. It follows that the internal energy of the DSS system is

$$\frac{\beta E_{\mathrm{DSS}}}{N} = \frac{1}{N}\left\langle \sum_{i<j}\left[4\beta\epsilon\left(\frac{\sigma}{r_{ij}}\right)^{12} + \frac{\beta}{2}\left(\frac{(\boldsymbol{\mu}_i\cdot\boldsymbol{\mu}_j)}{r_{ij}^3} - \frac{3(\boldsymbol{\mu}_i\cdot\boldsymbol{r}_{ij})(\boldsymbol{\mu}_j\cdot\boldsymbol{r}_{ij})}{r_{ij}^5}\right)\right]\right\rangle. \tag{5.21}$$

By a similar argument, the internal energy of the EMB system is

$$\frac{\beta E_{\mathrm{EMB}}}{N} = \frac{1}{N}\left\langle \beta\sum_{i<j} w_2(\boldsymbol{r}_i,\boldsymbol{r}_j) + \frac{3\beta}{2}\sum_{i<j<k} w_3(\boldsymbol{r}_i,\boldsymbol{r}_j,\boldsymbol{r}_k)\right\rangle. \tag{5.22}$$

The internal energies calculated for both systems at $\rho^* = 0.007$ are shown as a function of $\beta^* = 1/T^*$ in Fig. 5.6. As expected, E_{DSS} and E_{EMB} produce similar results for values of $\beta^* \lesssim 1.0$ ($\lambda \lesssim 5.0$). As λ is increased past this point, E_{EMB} decreases at a very fast rate. As β is increased, E_{DSS} drops to a minimum before increasing slowly. This, along with the resulting peak in heat capacity, is a common feature of particle association. By fitting the simulation data with a [2/2] Padé approximant (shown in Fig. 5.6), it is possible to approximate the constant-volume heat capacity $C_V = -k_{\mathrm{B}}\beta^2(\partial E/\partial\beta)_{N,V}$. This function shows a peak at $\beta \simeq 11.1$ which correspond to $\lambda \simeq 11.5$, a coupling constant close to the first value at which chains begin to appear in the DSS system [Fig. 5.2].

5.4.3 Matching EMB and DSS structure at high values of dipolar constant

A system of particles interacting *via* the EMB potential appears to reproduce the structure observed in an equivalent system of DSS particles very well at low values of λ, where the distinctive chain-like structure of a dipolar system is not present, but seems to overestimate the chain formation that occurs in a DSS system at higher values of λ. This is problematic as this would mean that the EMB system can only be used to approximate a DSS system when the dipolar coupling energy is not greater than the thermal energy by more than one order of magnitude. For the EMB system to be a useful approximation, it is imperative that it provides a close match to the high-λ structure as well. Chain formation does not occur

in a LJ system. Therefore the chain-inducing part of the EMB potential must be the three-body AT interaction. As chain formation is overemphasised in the EMB system, it may be possible to match the structure formed in a system of DSS particles at a high value of λ by reducing the strength of the chain-forming, three-body part of the EMB potential. In other words, the three-body interaction would act as a perturbation to the two-body interaction, with the three-body coefficient a no longer treated as a constant of value $4/\sqrt[3]{3}$ but as a variable of value $0 < a < 4/\sqrt[3]{3}$.

The structures of systems of DSS particles run with $\lambda = 15.0$, $\rho^* = 0.007$ and 0.100 were determined. The equivalent systems of EMB particles were run at $T^* = 12.0/\lambda^2 = 0.0533$ and $a = 4/\sqrt[3]{3}$, and as expected it was found that the degree of chaining, the chain rigidity, and the long-ranged, repetitive peaks seen in the RDF were all greater than in the equivalent system of DSS particles. The value of a was then lowered progressively in the hope that a match between systems run with the two interaction potentials could be reached. As the strength of the three-body coefficient is decreased, the relative strength of the chain-forming, three-body part of the many-body potential decreases and the two-body LJ interaction becomes the dominant term in the EMB interaction. Decreasing the three-body term reduced the degree of chaining that had prevented the system from condensing into a liquid-like state at at low temperatures. Furthermore, a reduction in the chaining parameter a alone does not have any great effects on the positions of the peaks in the RDFs. This implies that it is not possible to reproduce the increase in nearest neighbour distance observed in the DSS system simply by making chain formation less favoured.

To prevent the EMB system from condensing, it is also necessary to decrease the effective LJ energy and range parameters. By rewriting the two-body and three-body contributions to the EMB interaction as

$$\beta w_2(\boldsymbol{r}_i, \boldsymbol{r}_j) = \frac{4}{T^*}\left(\frac{\overline{\epsilon}}{\epsilon}\right)\left[\left(\frac{\overline{\sigma}}{r_{ij}}\right)^{12} - \left(\frac{\overline{\sigma}}{r_{ij}}\right)^{6}\right] \tag{5.23}$$

$$w_3(\boldsymbol{r}_i, \boldsymbol{r}_j, \boldsymbol{r}_k) = \frac{\epsilon a^{3/2}}{T^{*1/2}}\left(\frac{\overline{\sigma}}{\sigma}\right)^{9} f_3(\boldsymbol{r}_i, \boldsymbol{r}_j, \boldsymbol{r}_k), \tag{5.24}$$

where $\overline{\epsilon}$ and $\overline{\sigma}$ act as the effective LJ parameters to the system, it is now possible to lower the three-body chain-inducing perturbation to much lower levels while keeping the system from condensing into a liquid state. It is worth emphasising that these factors were changed in such a way as to ensure that the EMB systems

were run at the same reduced density as the DSS systems that are being matched, and that this is only a change of scale. After multiple attempts at finding a simple theory to govern the choice of parameters $\overline{\epsilon}$, $\overline{\sigma}$, and a, it is found that the best approach to match the EMB structure with that of the DSS systems was repetitive trial and error.

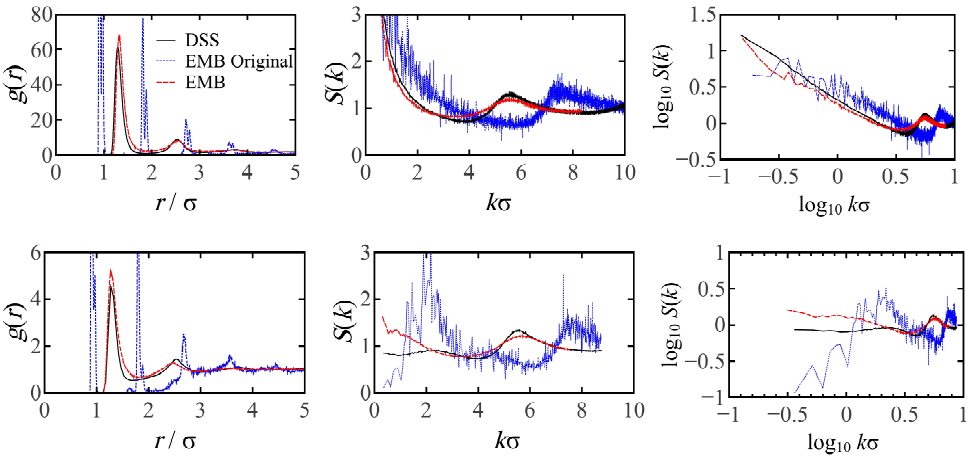

Figure 5.7: Comparison of the structural functions seen in a simulation run using the DSS potential (solid black line) at $\lambda = 15.0$, $\rho^* = 0.007$ and 0.100, $T^* = 0.0533$ with the structure observed in simulations run using the equivalent EMB potential (blue dotted line) and the structure observed in a EMB system (red dashed line) run at the same temperature but different values of $\overline{\epsilon}$, $\overline{\sigma}$, and a.

Figure 5.7 shows the RDFs, structure factors, and log-log plots of the structure factors obtained from the original DSS system, the original EMB system, and the matched EMB system at densities $\rho^* = 0.007$ and 0.100. The match at $\rho^* = 0.007$ was obtained with parameters $\overline{\epsilon} = 0.25\epsilon$, $\overline{\sigma} = 1.20\sigma$, and $a = 0.42$. Likewise, the match at $\rho^* = 0.100$ was found with parameters $\overline{\epsilon} = 0.19\epsilon$, $\overline{\sigma} = 1.16\sigma$, and $a = 0.37$. At both densities, the initial peaks of the RDFs of the matched EMB systems coincide with those of the DSS RDFs very well. Furthermore, the smaller peaks at longer range are also accurately reproduced by the matched EMB potential. At $\rho^* = 0.007$, the matched structure factor is very close to overlapping the original DSS structure factor. The first peak at $k\sigma \simeq 5.5$ in the original DSS system is matched both in height and position. Furthermore, the linear decrease in the log-log plot of the structure factor, indicative of the presence of chaining in the system [126], is also well matched. At $\rho^* = 0.100$, the structure factor of the new EMB system does not match that of the DSS system in the range $k\sigma \lesssim 3.0$. Above this wavevector, the structures seen in the two systems are very similar. The difference in the structure factors at low wavevectors is indicative of the system of EMB particles having a lower compressibility than the

DSS systems. This is probably a result of the DSS particles having a very definite 'soft' close-ranged interaction that decays more slowly than the sharp repulsive part of the LJ interaction.

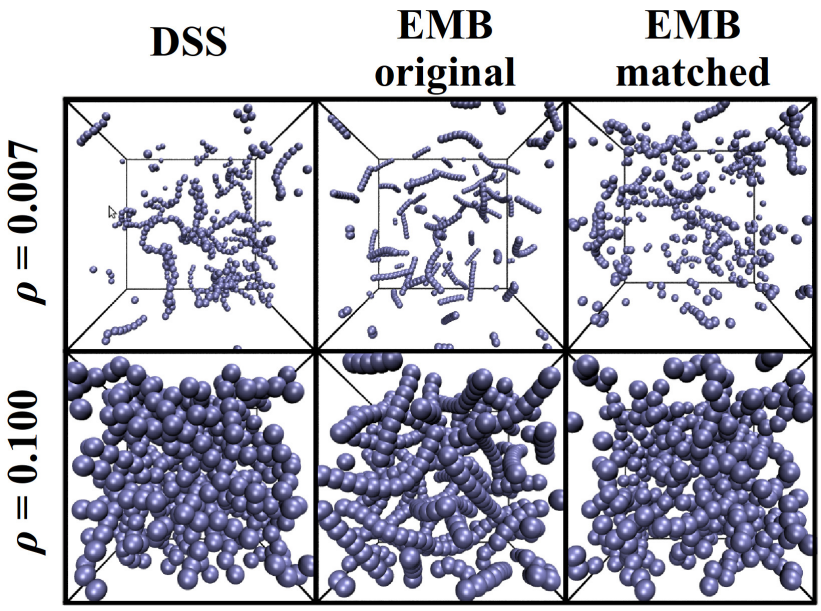

Figure 5.8: Simulation snapshots of systems with the DSS potential, the original unmatched EMB potential, and the matched EMB potential at densities $\rho^* = 0.007$ and 0.100 and $\lambda = 15.0$.

Simulation snapshots of the DSS system, the original EMB system, and the matched EMB system at densities $\rho^* = 0.007$ and 0.100 are shown in Fig. 5.8. As stated previously, chaining is much more prevalent in the original EMB systems compared to the DSS systems. In fact, at $\rho^* = 0.100$, the EMB system produces definite chains whereas the equivalent DSS system is still in a dissociated 'normal' liquid state. The DSS system shows clear chain formation at $\rho^* = 0.007$, as predicted with the internal energy calculations. As seen previously for the systems at $\lambda = 10.0$ and 20.0, the original EMB system exhibits more rigid chains than the equivalent DSS system at $\rho^* = 0.007$.

The snapshots for the matched EMB system are very similar to those for the DSS system. At $\rho^* = 0.007$, the chains seen in the matched EMB system are less rigid and of similar length to those in the DSS system. The liquid state formed by the matched EMB system at $\rho^* = 0.100$ shows the same chain-like liquid structure as seen in the DSS system. This seems to show that the effective LJ parameters $\overline{\epsilon}$ and $\overline{\sigma}$, and the chain-inducing parameter a have been successfully adjusted to reproduce the structure observed in a DSS system at high values of λ. Though no method was found to predict what these parameters will be for a given system, it

was possible to optimise the matching parameters after preliminary calculations with a small number of particles ($N \simeq 100$) before increasing the system size ($N = 512$) to obtain the final results.

5.4.4 The effects of chain formation on the vapour-liquid phase transition

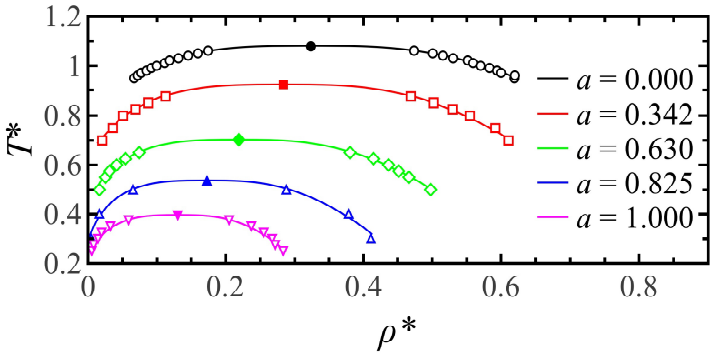

Figure 5.9: Vapour-liquid coexistence curves for the EMB system (open symbols) with varying three-body coefficients a. The critical points (filled symbols) were predicted by using Eq. 5.13 and 5.14.

When $a = 0$, there is no three-body interaction and the EMB system is equivalent to a LJ system. It is well known that LJ systems undergo vapour-liquid phase transitions. The formation of chains is thought to have an effect on the vapour-liquid phase transition, with some studies of dipole particles showing strong evidence that, when chaining is present, the vapour-liquid phase transition disappears completely [142–144]. The three-body potential can be used as a chain-forming perturbation to the LJ potential, and the three-body coefficient a of the EMB potential is used to control the amount of chain formation to discover the effects of chain formation on the vapour-liquid phase transition.

Figure 5.9 shows the vapour-liquid coexistence curves obtained from the EMB potential with varying a. First, note that when $a = 0$, the system clearly undergoes a vapour-liquid phase transition with the critical temperature and critical density found to be $T_c^* = 1.0790$ and $\rho_c^* = 0.3236$, respectively. For an equivalent system of LJ spheres, Shi and Johnson have shown that the critical parameters are $T_c^* = 1.0795(2)$ at $\rho_c^* = 0.3211(5)$ [152], and Smit found them to be $T_c^* = 1.085(5)$ at $\rho_c^* = 0.317(6)$ [155]. Both are in good agreement with the results here. Next, note that minor three-body perturbations to the LJ system lead to drastic changes

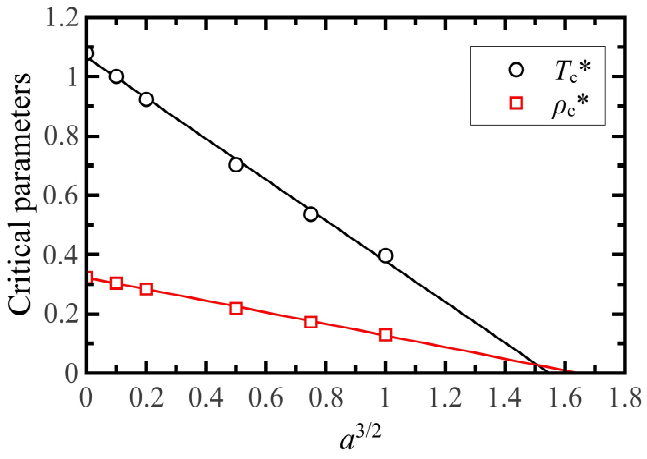

Figure 5.10: The critical density ρ_C^* and critical temperature T_C^* as a function of the three-body coefficient $a^{(3/2)}$. The linear best fit is to emphasise the point at which the phase transition is expected to disappear.

in the vapour-liquid phase diagram of the system. As a is increased, the area of the vapour-liquid coexistence region shrinks. Furthermore, there is an evident reduction in the critical parameters. The evolution of critical density and the critical temperature have been plotted in Fig. 5.10 against $a^{3/2}$ – the strength of the AT potential compared with thermal energy. It appears that both critical parameters decrease linearly with $a^{3/2}$. With this assumption, the critical density and temperature would reach both zero when $a^{3/2} \simeq 1.6$ ($a \simeq 1.4$). For values of $a \gtrsim 1.4$, it is expected that the chain-forming effects of the three-body potential prevent the occurrence of two coexisting fluid phases. This indicates that there exists a threshold 'chaining strength' above which the chain-forming perturbation to the LJ potential will causes the disappearance of the vapour-liquid phase transition.

5.5 Conclusions

In this chapter, the anisotropic, long-ranged, dipole-dipole interaction was modelled by using the leading-order two- and three-body terms of an equivalent isotropic, short-ranged, many-body interaction. The structures of systems interacting *via* the many-body EMB potential were compared with those of equivalent DSS systems, with the two being in good agreement for the experimentally relevant dipole coupling constants $\lambda \leq 2.0$ across all densities tested. At higher

dipole coupling constants, the structures observed in EMB systems differed from those observed in equivalent DSS systems. This difference results from the EMB potential overestimating the chain formation observed in DSS systems. It is possible to reduce the strength of the chain-forming, three-body part of the EMB potential to obtain a better match with the equivalent DSS system. This chapter concludes with a study of the effects that increasing the strength of the chain-forming three-body term of the EMB potential has on the vapour-liquid phase transition. It was found that, as the chaining coefficient is increased, the area of the vapour-liquid coexistence region and the critical parameters decrease. It is speculated that there exists a threshold chaining coefficient above which the vapour-liquid phase transition disappears completely. As the EMB potential is a model for the DSS potential, this work implies that there is a dipole coupling strength at which chain formation will result in systems of dipole particles no longer being able to condense into liquids.

There are still some characteristic features of DSS systems that are not yet reproduced by using the EMB potential. For instance, there is, as yet, no evidence that the EMB potential will facilitate the formation of rings, the lowest energy configuration of DSS systems. The EMB potential can easily be improved, with the addition of second-order and third-order terms to the two- and three-body potentials, or even the addition of four-body terms, likely to increase the accuracy of this many-body potential. The addition of more terms will make it more computationally expensive to use this potential. However, the time spent resolving these equations should be much less than the time gained resolving only short-ranged interactions. For this reason, EMB potentials have great prospects as models for the DSS potential.

Chapter 6

The dynamic magnetic susceptibility of a ferrofluid

6.1 Introduction

One field where the use of dipolar particles has been particularly promising is that of medical physics. The properties of magnetic dipolar particles, in particular their response to external magnetic fields, make them ideal in the medical profession. Dipolar particles may be used as contrast agents in magnetic resonance imaging (MRI) [35, 156–159]. Their magnetic properties can be used to enable targeted drug delivery [35]. Furthermore, dipolar particles can be made to generate localised heat when under an alternating field, a technique known as hyperthermia [33, 35, 36]. This technique has huge potential as a non-invasive, highly accurate method for destroying tumorous cells in patients. Clinical trials have begun on patients with brain and prostate cancers [34, 37, 38].

The dynamic magnetic susceptibility (DMS) of dipolar particles governs the response of the magnetisation of a system to an applied oscillating magnetic field. It is of critical importance in determining the frequency of field oscillation needed to be applied to generate localised heating [160, 161]. Analogously to the microwave heating of water, the frequency of oscillation at which optimum heating occurs for dipoles is determined from the peak frequency of the imaginary part of the DMS. The accurate prediction of the DMS of a system of dipolar particles underpins the development of hyperthermia techniques. The prediction of the DMS of dipolar systems has been poorly researched, with the current prevailing method

being the use of Debye-theory predictions. This method is exact for systems of non-interacting dipolar particles and therefore gives accurate predictions for systems of weakly-interacting dipolar particles and systems of particles at very low concentrations. However, this theory fails to accurately predict the DMS of systems of dipolar particles that may be used for hyperthermia treatment.

A dynamic theory based on the modified mean-field (MMF) approach has been developed to provide more precise predictions of the DMS of experimentally relevant systems of dipolar particles[1]. Originally, the MMF theory describes the response of the magnetisation of a ferrofluid (a system of dipole particles in a carrier fluid) to a static external magnetic field. It considers both the magnetic field being applied to the system and the magnetic field resulting from the dipole particles [163]. The work done by Ivanov *et al.* extends this theory to consider the effects of a dynamic external magnetic field. Results obtained from the MMF theory have been tested against experimental results for polydisperse systems of dipolar particles and have been found to provide a more accurate prediction of the DMS than previously achievable using Debye theory [162]. Ivanov *et al.* note that it is difficult to predict the range of dipolar coupling strengths in which the MMF theory provides more accurate predictions. Furthermore, it is expected that the results for a monodisperse dipolar system should accentuate the differences between the Debye theory and the MMF-theory predictions. Particles with different diameters and dipole moments would have different dipolar relaxation times. This results in the DMS of a polydisperse system being 'smeared out'. This effect would not be seen in a monodisperse system. In this chapter, the DMSs predicted by Debye theory and MMF theory for systems of monodisperse dipolar particles are compared with results from Brownian dynamics simulations.

This chapter is organised as follows. The derivation of the MMF predictions for the DMS will be described. The simulation methods are then defined, as is the method used to derive the DMS from the magnetisation autocorrelation function. The results are then presented and discussed. A comparison of the Debye-theory predictions for the DMS and those obtained from simulated systems of non-interacting dipolar particles is carried out to validate the methods used. Debye theory and MMF-theory predictions for the DMS are compared with the susceptibilities obtained from systems of interacting dipolar particles. The

[1]The work presented in this chapter is a collaborative project done in conjuncture with A. O. Ivanov and E. A. Elfimova of the Ural Federal University (Russia), who kindly provided and explained the modified mean-field theory. The modified mean-field theory described in Section 6.2 was developed by the authors of [162].

differences between the DMSs predicted by the theories and those obtained from simulations are then analysed through the comparison of a set of characteristic parameters. These parameters are the initial slopes of the real and imaginary part of the DMS, the peak position in the imaginary part of the susceptibility, and the characteristic relaxation lifetime of the magnetisation autocorrelation function. Finally, all of the results are drawn together to provide an assessment of the accuracy of both Debye theory and MMF theory in predicting the DMS of systems of interacting dipolar particles over broad ranges of particle concentration and interaction strength.

6.2 Theory

Consider a system of dipolar particles immersed in a carrier fluid, each with dipole moment of the same magnitude μ and diameter σ but different orientation $\boldsymbol{\Omega}_i(t)$ that interact *via* the dipole-dipole interaction (Section 2.4.3). From linear response theory, the magnetisation of the system of N particles at time t can be defined as $\boldsymbol{M}(t) = \mu \sum_{i=1}^{N} \boldsymbol{\Omega}_i(t)$. The DMS $\chi(\omega)$ of a system of dipolar particles at temperature T and of volume V is given by

$$\chi(\omega) = \frac{\mu_0}{3Vk_{\mathrm{B}}T}\left[\langle \boldsymbol{M}(0)\cdot\boldsymbol{M}(0)\rangle + i\omega\int_0^\infty \langle \boldsymbol{M}(t)\cdot\boldsymbol{M}(0)\rangle \exp(i\omega t)\mathrm{d}t\right] \tag{6.1}$$

$$= \chi(0)\left[1 + i\omega\int_0^\infty \frac{\langle \boldsymbol{M}(t)\cdot\boldsymbol{M}(0)\rangle}{\langle \boldsymbol{M}(0)\cdot\boldsymbol{M}(0)\rangle}\exp(i\omega t)\mathrm{d}t\right] \tag{6.2}$$

where ω is the frequency, k_{B} is the Boltzmann constant, and $\chi(0)$ is the static susceptibility. For a system of non-interacting dipolar particles, the particle orientations are uncorrelated so that $\langle \boldsymbol{\Omega}_i(t)\cdot\boldsymbol{\Omega}_j(0)\rangle = 0$ and $\langle \boldsymbol{\Omega}_i(t)\cdot\boldsymbol{\Omega}_i(0)\rangle = \exp(-t/\tau_{\mathrm{B}})$, where τ_{B} is the Brownian rotational relaxation time associated with the carrier liquid of the ferrofluid. Therefore

$$\langle \boldsymbol{M}(t)\cdot\boldsymbol{M}(0)\rangle = \mu^2\sum_{i=1}^{N}\sum_{j=1}^{N}\langle \boldsymbol{\Omega}_i(t)\cdot\boldsymbol{\Omega}_j(0)\rangle = N\mu^2\exp\left(-\frac{t}{\tau_{\mathrm{B}}}\right). \tag{6.3}$$

The static susceptibility is given by

$$\chi(0) = \frac{\mu_0}{3Vk_{\mathrm{B}}T}\langle \boldsymbol{M}(0) \cdot \boldsymbol{M}(0)\rangle. \tag{6.4}$$

For systems with no interparticle interactions, the static susceptibility is that of the Langevin theory [164] given by

$$\chi(0) = \chi_{\mathrm{L}} = \frac{4\pi\rho^*\lambda}{3} \tag{6.5}$$

where $\rho^* = \rho\sigma^3 = N/V$ is the reduced number density of the system, and $\lambda = \mu_0\mu^2/4\pi k_{\mathrm{B}}T\sigma^3$ is the dipolar coupling constant. Inserting Eq. 6.3 into Eq. 6.1 gives the Debye-theory susceptibility

$$\chi_{\mathrm{D}}(\omega) = \frac{\chi_{\mathrm{L}}}{1 - i\omega\tau_{\mathrm{B}}} = \chi_{\mathrm{L}}\left(\frac{1}{1+\omega^2\tau_{\mathrm{B}}^2} + \frac{i\omega\tau_{\mathrm{B}}}{1+\omega^2\tau_{\mathrm{B}}^2}\right). \tag{6.6}$$

This result is exact for systems of non-interacting dipolar particles with dipoles rotating in a diffusive manner. However, pair interactions are not taken into account in the Debye theory and it is therefore only applicable for very dilute systems with very weakly interacting dipolar particles. Recently, Ivanov *et al.* used a MMF approach to consider the effects of pairwise correlations resulting from dipole-dipole interactions [162]. They found that, by including the lowest-order terms in ρ^* and λ, the real part $\chi^{'}_{\mathrm{MMF}}(\omega)$ and imaginary part $\chi^{''}_{\mathrm{MMF}}(\omega)$ of the DMS of systems of interacting dipolar particles can be expressed in terms of the real and imaginary parts of the Debye susceptibility ($\chi^{'}_{\mathrm{D}}(\omega)$ and $\chi^{''}_{\mathrm{D}}(\omega)$, respectively), and take the form:

$$\chi^{'}_{\mathrm{MMF}}(\omega) = \chi^{'}_{\mathrm{D}}(\omega) + \frac{1}{3}\left[\chi^{'}_{\mathrm{D}}(\omega)^2 - \chi^{''}_{\mathrm{D}}(\omega)^2\right] \tag{6.7}$$

$$\chi^{''}_{\mathrm{MMF}}(\omega) = \chi^{''}_{\mathrm{D}}(\omega)\left[1 + \frac{2}{3}\chi^{'}_{\mathrm{D}}(\omega)\right] \tag{6.8}$$

From this, it is easy to derive the MMF prediction for the static susceptibility. It is clear from Eq. 6.8 that $\chi^{''}_{\mathrm{MMF}}(0) = 0$. It therefore follows that

$$\chi_{\mathrm{MMF}}(0) = \chi^{'}_{\mathrm{MMF}}(0) = \chi_{\mathrm{L}}\left(1 + \frac{\chi_{\mathrm{L}}}{3}\right). \tag{6.9}$$

Equation 6.9 provides the first order MMF prediction for the static susceptibility of interacting systems.

6.3 Simulation methods

Canonical (NVT) Brownian dynamics (BD) simulations were carried out using the LAMMPS package [50]. $N = 216$ dipolar particles were simulated in a cubic box with periodic boundary conditions applied. Particles interacted by the pair potential $U = U_{\mathrm{WCA}} + U_{\mathrm{DD}}$ composed of the repulsive Weeks-Chandler-Andersen and the dipole-dipole interactions. These are given by

$$U_{\mathrm{WCA}}(\boldsymbol{r}_i, \boldsymbol{r}_j) = \begin{cases} 4\epsilon \left[\left(\dfrac{\sigma}{r_{ij}} \right)^{12} - \left(\dfrac{\sigma}{r_{ij}} \right)^{6} \right] + \epsilon & r \leq r_{\mathrm{min}} \\ 0 & r > r_{\mathrm{min}} \end{cases} \tag{6.10}$$

$$U_{\mathrm{DD}}(\boldsymbol{r}_i, \boldsymbol{r}_j, \boldsymbol{\mu}_i, \boldsymbol{\mu}_j) = \frac{(\boldsymbol{\mu}_i \cdot \boldsymbol{\mu}_j)}{r_{ij}^3} - \frac{3(\boldsymbol{\mu}_i \cdot \boldsymbol{r}_{ij})(\boldsymbol{\mu}_j \cdot \boldsymbol{r}_{ij})}{r_{ij}^5} \tag{6.11}$$

where $r_{ij} = |\boldsymbol{r}_j - \boldsymbol{r}_i|$ is the interparticle distance, μ_i is the dipole moment of particle i, σ is the particle radius, ϵ is the LJ energy, and $r_{\mathrm{min}} = 2^{1/6}\sigma$ is the position of the minimum of the LJ potential. Particles were simulated in reduced units with $\sigma = \epsilon = 1$ and with mass $m = 1$. Long-ranged dipole interactions were computed using Ewald summation with conducting boundary conditions. The temperature was kept constant at $T^* = 1.0$ for all runs using the Langevin thermostat with a damping parameter $\tau^*_{\mathrm{damp}} = 0.05$ and associated Langevin friction coefficient $\gamma^* = 1/\tau^*_{\mathrm{damp}} = 20$. This results in a simulation Brownian rotational relaxation time of $\tau^*_{\mathrm{B}} = (6T^*\tau^*_{\mathrm{damp}})^{-1} = 10/3$. A timestep of $\delta t^* = 0.002$ was used, meaning that the Brownian relaxation time corresponds to 1667 timesteps. This ensures that the overdamped Brownian dynamics conditions appropriate for Debye and MMF theories (and real ferrofluids) are met. This results in dipoles orientations changing as if the particles were in a very viscous fluid, and ensures that dipole reorientation is in the diffusive regime. A typical run consisted of an equilibration stage lasting 2×10^6 timesteps, followed by a production stage lasting 2×10^7 timesteps for systems of non-interacting particles or 4×10^7 timesteps for system of interacting particles. Averages were calculated from measurements taken at intervals of 5 timesteps. This certifies that there is

little fluctuation in the magnetic autocorrelation function at long times, thereby ensuring that the errors associated with the results are in the regime described in Section 2.7.4.

One set of simulations was run at fixed density $\rho^* = 0.2$ with varying dipolar coupling constant $\lambda = 0.25$, 0.50, 0.75, 1.00, 1.25, 1.50, 1.75, 2.00, 2.50, 3.00, and 3.50, while another set of simulations was run at fixed dipolar coupling constant $\lambda = 1.0$ with varying density $\rho^* = 0.1$, 0.2, 0.3, 0.4, 0.5, 0.6, and 0.7. These systems were each run twice – once with the dipole-dipole interaction switched off to allow for comparison with Debye-theory predictions, and once with the normal long-ranged dipole-dipole interactions to assess the effects of these interactions.

6.4 Results and discussions

6.4.1 Static susceptibility

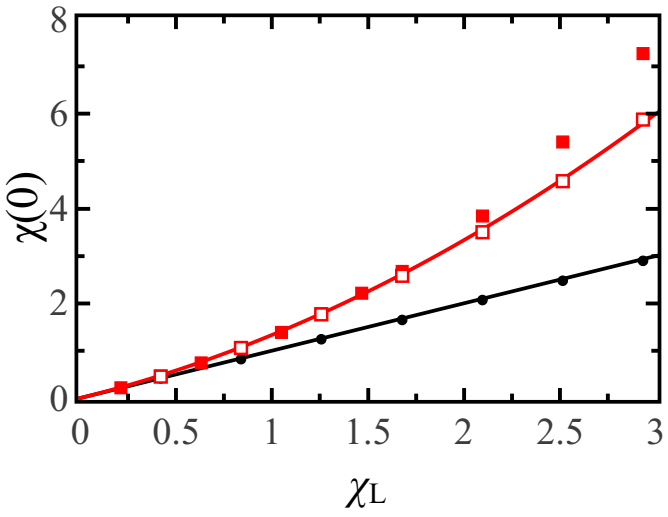

Figure 6.1: Static susceptibility $\chi(0)$ as a function of the Langevin susceptibility χ_L. Debye (Langevin) theory (black line) and MMF theory (red line) are shown alongside simulation results for systems of non-interacting dipolar particles (filled black circles), systems of interacting particles at constant density $\rho^* = 0.2$ (filled red squares), and systems of interacting particles at constant dipolar coupling constant $\lambda = 1.0$ (open red squares).

The static susceptibility $\chi(0)$ determines the response of the system to a static magnetic field. Here, it provides an easy parameter that can be derived for both theories and can be compared with simulation results. As shown previously,

Debye theory predicts that the static susceptibility is equal to the Langevin susceptibility [Eq. 6.5]. Figure 6.1 compares the static susceptibilities predicted by Debye theory and MMF theory with the static susceptibility obtained from systems simulated without dipole interactions and systems simulated at low values of χ_L. First, it is worth noting that the non-interacting simulated systems and Debye-theory results are in perfect agreement. At low values $\chi_L < 0.5$, both the Debye theory and the MMF theory provide similar results in good agreement with the simulation results for interacting particles. In the range $0.5 < \chi_L \leq 3.0$, MMF theory provides a much better fit to simulation than does the Debye theory. Also note that the systems run at constant dipolar coupling constant $\lambda = 1.0$ are accurately described by the MMF theory for all densities tested. Systems simulated at constant density $\rho^* = 0.2$ are matched by the MMF results for values of $\chi_L \leq 2.0$. Above this point, the MMF predictions of static susceptibility begins to diverge from the simulated results.

6.4.2 DMS of non-interacting systems

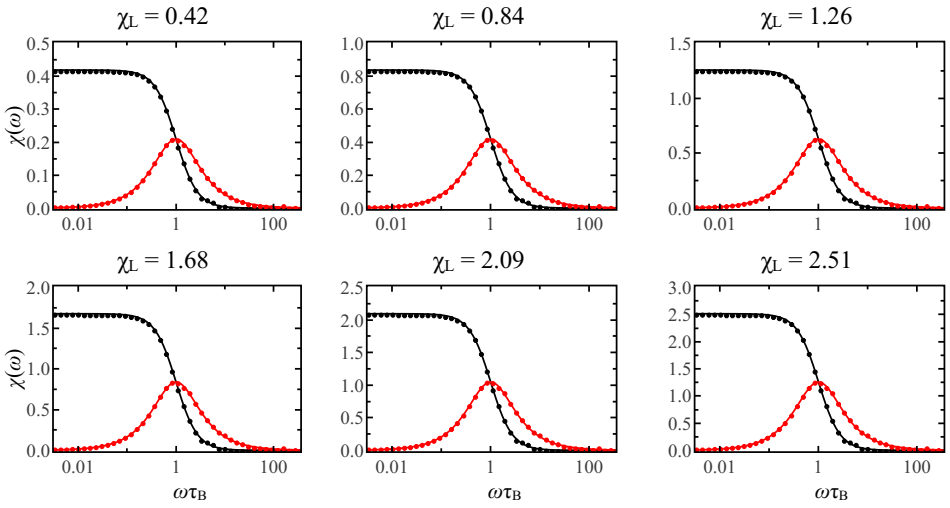

Figure 6.2: Dynamic susceptibilities $\chi(\omega)$ plotted as their real and imaginary components at varying χ_L. Debye-theory predictions for the real component (black lines) and imaginary component (red lines) of the DMS are plotted alongside simulation results for the real component (black symbols) and imaginary component (red symbols) of the DMS of systems of non-interacting dipolar particles at constant $\rho^* = 0.2$.

Debye-theory predictions for the DMS are exact for all systems of non-interacting particles. Therefore, a comparison of simulation results for non-interacting particles with Debye theory can be used to verify the accuracy of the simulation method for obtaining the DMS. The DMS is calculated from the magnetisation

autocorrelation function of the simulated systems. The magnetisation autocorrelation function for non-interacting systems can easily be derived from a simulation trajectory. The magnetic DMS is proportional to the Fourier transform of this decay function [Eq. 6.1]. It is therefore important for the simulated magnetic autocorrelation function to decay smoothly to keep noise in $\chi(\omega)$ to a minimum.

Figure 6.2 shows a comparison of the DMS obtained for a selection of systems of non-interacting particles with the Debye-theory predictions [Eq. 6.6]. The simulations were run both at constant density $\rho^* = 0.2$ and at constant dipolar coupling constant $\lambda = 1.0$. At constant χ_L, simulations with constant λ or constant ρ^* should result in exactly the same DMS, and this is confirmed in the figure. Furthermore, the simulated $\chi(\omega)$ matches the Debye-theory prediction $\chi_D(\omega)$ perfectly at each value of χ_L tested. This confirms that the method used to obtain $\chi(\omega)$ from simulation generates accurate results. The same method can therefore be used to derive $\chi(\omega)$ for systems of interacting dipolar particles.

6.4.3 DMS of interacting systems

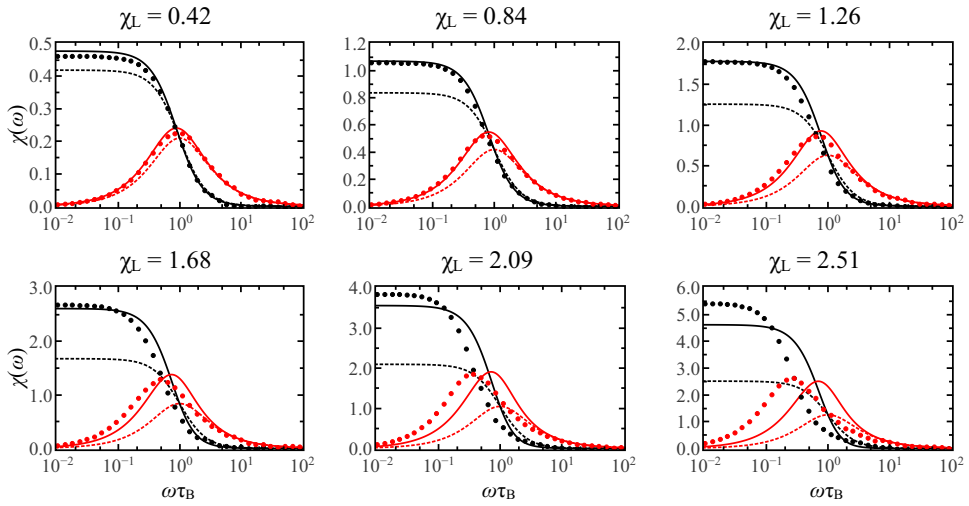

Figure 6.3: Dynamic susceptibilities $\chi(\omega)$ plotted as their real and imaginary components at varying χ_L. MMF predictions for the real component (full black lines) and imaginary component (full red lines) of the DMS and Debye-theory predictions for the real component (dashed black line) and imaginary component (dashed red lines) of the DMS are plotted alongside simulation results for the real component (black symbols) and imaginary component (red symbols) of the DMS of systems of interacting particles at constant density $\rho^* = 0.2$.

The Debye-theory predictions for the DMS have often been used to describe the magnetisation response of weakly interacting dipolar particles. Ivanov *et*

al. argue that the linear dependence on χ_L is only a good approximation for systems of particles with extremely weak dipole interactions at very low densities ($\chi_L \to 0$) [162]. They expect that the MMF predictions for the DMS, $\chi_{MMF}(\omega)$, will provide a much more accurate description in the the regime $\chi_L \lesssim 1.0$, which is characteristic of real ferrofluids of moderate interactions.

Figure 6.3 shows a comparison of the DMS from Debye theory, MMF theory, and simulations at constant density $\rho^* = 0.2$ with varying dipolar coupling constant. Interestingly, there is already a noticeable difference between the simulation results and the Debye-theory predictions at $\chi_L = 0.42$. The low-ω real component of the simulated susceptibility $\chi^{'}(\omega)$ plateaus at a higher value than is predicted by Debye (Langevin) theory. Furthermore, the peak position ω_0 of the imaginary component of the susceptibility $\chi^{''}(\omega)$ shifts to lower frequencies when interactions are present. The peak height $\chi^{''}(\omega_0)$ is also much higher in simulations than according to Debye theory. While these discrepancies between the Debye-theory predictions and the simulation results are small at low values of χ_L, these increase substantially as χ_L is increased. It is clear that the Debye-theory predictions are not accurate for any of the interacting simulated systems studied here. In all cases studied, MMF theory is in much better agreement with the simulation results.

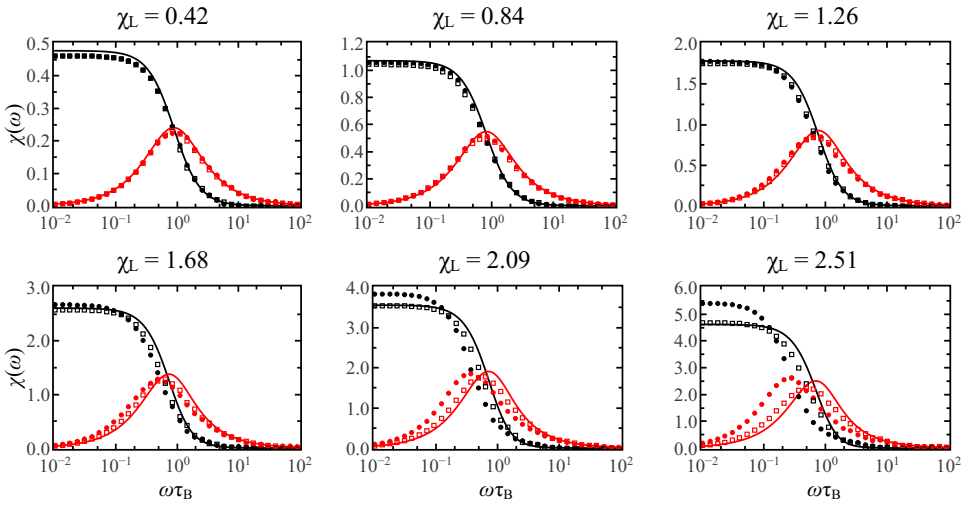

Figure 6.4: Dynamic susceptibilities $\chi(\omega)$ plotted as their real and imaginary components at varying χ_L. MMF predictions for the real component (black lines) and imaginary component (red lines) of the DMS are plotted alongside simulation results for the real component (full black circles) and imaginary component (full red circles) of the DMS of systems of interacting particles run at fixed density $\rho^* = 0.2$, and the real component (open black squares) and imaginary component (open red squares) of the DMS of systems of interacting particles run at constant dipolar coupling constant $\lambda = 1.0$.

Recall that χ_L, as defined in Eq. 6.5, is linearly proportional to both the dipolar

coupling constant λ and the density ρ^*. Both the Debye theory and the MMF theory predict that the DMS is dependent on ρ^* and λ through χ_L only. It therefore follows from these theories that systems with the same χ_L, but with different values of λ and ρ^* should possess the same DMS.

Figure 6.4 compares the MMF predictions of DMS against the DMS obtained from a set of simulation results run at constant density $\rho^* = 0.2$, and another set of simulations run at constant dipolar coupling constant $\lambda = 1.0$. At low values $\chi_L = 0.41$ and 0.84 the results from both sets of simulations are very closely matched to the MMF-theory predictions. As χ_L is increased, the peaks in $\chi''(\omega)$ from simulations at constant ρ^* shift to lower frequencies than the MMF-theory predictions whereas the peaks from simulations at constant λ remain closely matched to the MMF predictions. Only at higher values of χ_L (> 1.26) does a difference between the MMF predictions and the constant-λ simulations become evident. However, even at the highest values of χ_L tested, both the theory and the constant-λ simulations give the same value of $\chi(0)$ whereas the constant-ρ^* simulations give higher values of $\chi(0)$. It appears that the only effect of running a constant λ system at a high density is that $\chi(\omega)$ shifts to slightly lower frequencies than those predicted by the MMF theory. This is in following with the static susceptibility [Fig. 6.1] where, at high χ_L, the $\chi(0)$ obtained from constant-λ simulations were in good agreement with the MMF predictions, whereas this was not the case for simulations run at constant-ρ^*.

The normalised results for $\chi(\omega)$ are shown in Fig. 6.5. This emphasises the shifts in characteristic frequency and cancels out the difference in $\chi(0)$, and also highlights the differences in frequency predictions of the Debye theory and the MMF theory at high values of χ_L. At $\chi_L = 0.42$, there is no real difference between the constant-ρ^* simulation results and either of the theoretical predictions. As χ_L is increased, both the simulation results and MMF predictions shift to lower frequencies than those predicted by Debye theory. Again, there is very good match between the MMF predictions and the simulation results for $\chi_L = 0.42$ and 0.84, with the simulated $\chi(\omega)$ shifting to lower values of ω than those predicted by MMF theory at $\chi_L = 1.26$ and 1.68. Past this point, there is a huge discrepancy between MMF theory and the equivalent simulation results. In contrast, the normalised results for simulations run at constant λ [Fig. 6.6] retain a very good match to MMF-theory predictions up to and including $\chi_L = 1.68$. It is clear from the graphs that, for high χ_L, there is a frequency shift between $\chi(\omega)$ for simulated systems run at constant density and those at constant dipolar coupling constant.

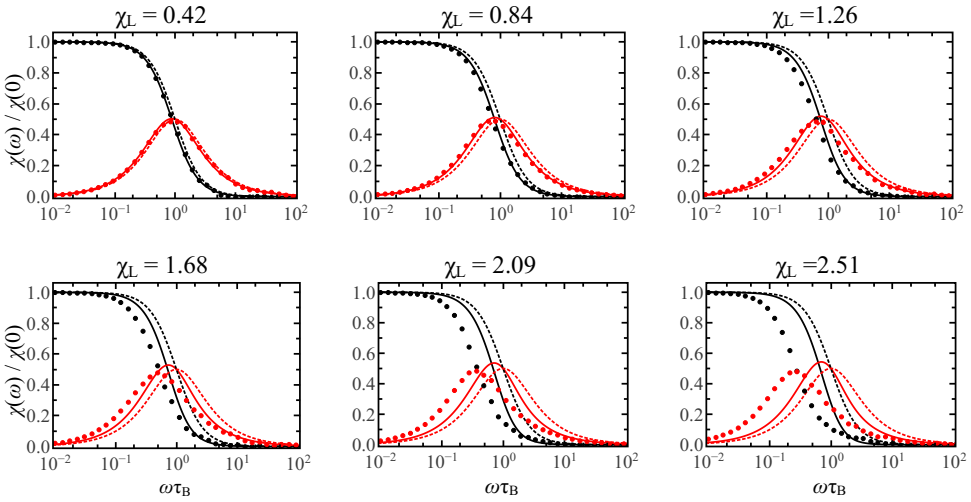

Figure 6.5: Normalised DMSs $\chi(\omega)/\chi(0)$ plotted as their real and imaginary components at varying χ_{L}. MMF predictions for the real component (full black lines) and imaginary component (full red lines) of the DMS and Debye-theory predictions for the real component (dashed black line) and imaginary component (dashed red lines) of the DMS are plotted alongside simulation results for the real component (black symbols) and imaginary component (red symbol) of the DMS of systems of interacting particles at constant density $\rho^* = 0.2$.

From this it appears that, for low values of $\chi_{\mathrm{L}} \lesssim 1.25$, the MMF theory is able to predict the DMS of a monodisperse system of dipolar particles very accurately. Past this point, its accuracy is dependent on the magnitudes of the parameters ρ^* and λ. Above $\chi_{\mathrm{L}} \geq 1.68$, MMF-theory predictions diverge from all simulation results. However, the MMF theory still provides much more accurate predictions than the Debye theory.

A comparison of the initial slopes of $\chi^{'}(\omega)$ and $\chi^{''}(\omega)$ is a good way of quantifying the accuracy of the theory at low ω. The initial slopes can easily be derived for both the Debye theory and MMF theory. In Debye theory a Taylor expansion of $\chi^{'}_{\mathrm{D}}(\omega)$ about $\omega = 0$ gives

$$\frac{\chi^{'}_{\mathrm{D}}(\omega)}{\chi_{\mathrm{D}}(0)} = \frac{\chi^{'}_{\mathrm{D}}(\omega)}{\chi_{\mathrm{L}}} = 1 - \omega^2\tau_{\mathrm{B}}^2 + O(\omega^4). \tag{6.12}$$

The corresponding result in the MMF theory is

$$\frac{\chi^{'}_{\mathrm{MMF}}(\omega)}{\chi_{\mathrm{MMF}}(0)} = 1 - A\omega^2\tau_{\mathrm{B}}^2 + O(\omega^4) \tag{6.13}$$

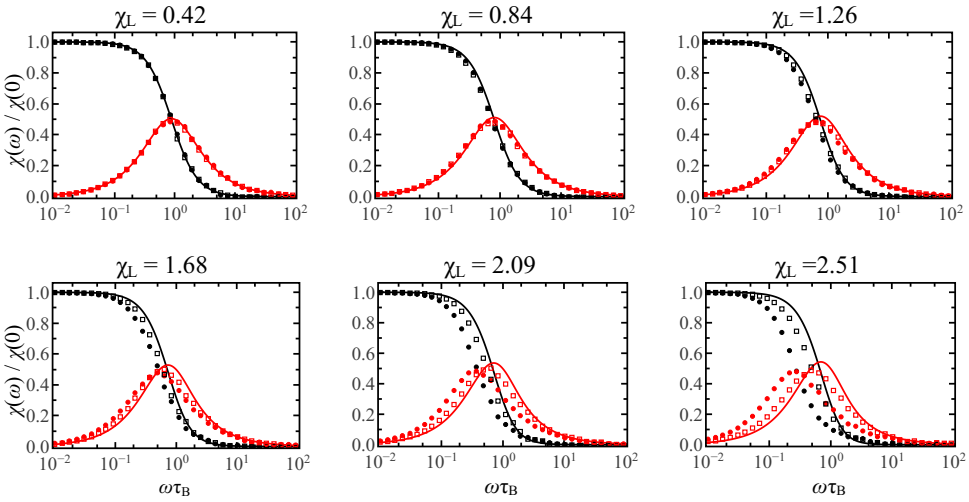

Figure 6.6: Normalised dynamic susceptibilities $\chi(\omega)/\chi(0)$ plotted as their real and imaginary components at varying χ_{L}. MMF predictions for the real component (black lines) and imaginary component (red lines) of the DMS are plotted alongside the real component (full black circles) and imaginary component (full red circles) of the DMS of systems of interacting particles run at fixed density $\rho^* = 0.2$, and the real component (empty black squares) and imaginary component (empty red squares) of the DMS of systems of interacting particles at constant dipolar coupling constant $\lambda = 1.0$.

where

$$A = \frac{3 + 3\chi_{\mathrm{L}}}{3 + \chi_{\mathrm{L}}}. \tag{6.14}$$

Clearly, for small values of χ_{L}, $A = 1$ as in the Debye theory. The initial slope of the imaginary part of the susceptibility is also easy to calculate. In the non-interacting, Debye-theory case, the low-ω behaviour of $\chi_{\mathrm{D}}^{''}(\omega)$ is

$$\chi_{\mathrm{D}}^{''}(\omega) = \chi_{\mathrm{L}} \frac{\omega\tau_{\mathrm{B}}}{1 + \omega^2\tau_{\mathrm{B}}^2} \approx \chi_{\mathrm{L}}\tau_{\mathrm{B}}\omega + O(\omega^3). \tag{6.15}$$

Similarly, by expanding out Eq. 6.8, the MMF-theory predictions for the initial slope can be derived from

$$\chi_{\mathrm{MMF}}^{''}(\omega) = \chi_{\mathrm{L}} \left[\frac{\omega\tau_{\mathrm{B}}}{1 + \omega^2\tau_{\mathrm{B}}^2} + \frac{2\chi_{\mathrm{L}}}{3} \frac{\omega\tau_{\mathrm{B}}}{(1 + \omega^2\tau_{\mathrm{B}}^2)^2} \right] \tag{6.16}$$

$$\approx \chi_{\mathrm{L}}\omega\tau_{\mathrm{B}} \left(1 + \frac{2}{3}\chi_{\mathrm{L}} \right) + O(\omega^3). \tag{6.17}$$

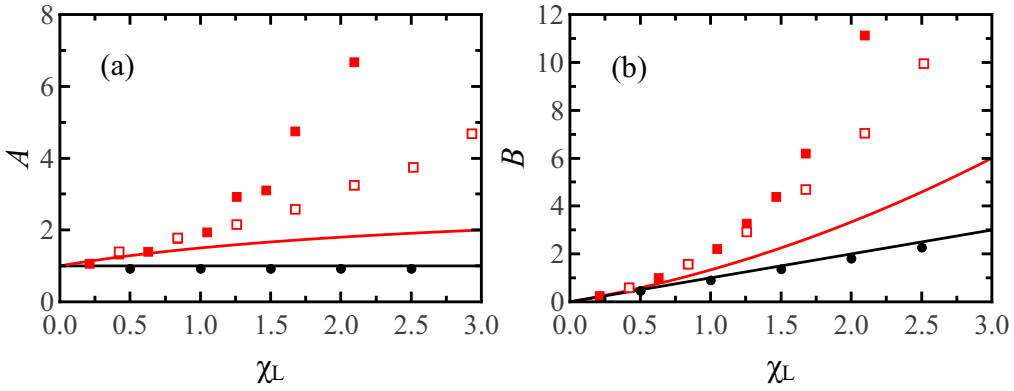

Figure 6.7: Initial slope parameters as a function of χ_{L} for the real part (a) and the imaginary part (b) of the DMS. Debye theory (black line) and MMF theory (red line) are shown alongside simulations results from systems of non-interacting dipolar particles (filled black circles), systems of interacting particles at constant density $\rho^* = 0.2$ (filled red squares), and systems of interacting particles at constant dipolar coupling constant $\lambda = 1.0$ (open red squares).

Both theories predict that $\chi''(\omega)$ has a linear dependence on ω for small ω. Therefore, it is possible to rewrite the imaginary component of the susceptibility as $\chi''(\omega) = B\omega\tau_{\mathrm{B}}$, where $B = \chi_{\mathrm{L}}$ according to Debye theory, and $B = (\chi_{\mathrm{L}} + 2\chi_{\mathrm{L}}^2/3)$ according to MMF theory. As with the real component, both theories predict the same results to the leading order term of χ_{L}, but diverge as χ_{L} is increased.

The predictions for the initial slope parameter A and B are plotted in Fig. 6.7(a) and Fig. 6.7(b), respectively. There is little agreement between Debye theory and MMF-theory predictions for A, whereas they are in good agreement on the prediction of B when $\chi_{\mathrm{L}} \leq 0.5$. The results for A and B obtained from systems of non-interacting particles match those predicted by Debye theory for all values of χ_{L}. With $\chi_{\mathrm{L}} \lesssim 0.21$, the initial slope parameters A calculated from simulated systems of interacting particles are close to those predicted by Debye theory. The range of agreement between simulation and Debye theory is greater for B, and there is a good match up to $\chi_{\mathrm{L}} \simeq 0.5$. With $\chi_{\mathrm{L}} \leq 0.5$, there is little or no agreement between simulation results and Debye-theory predictions of the parameters. MMF predictions for A and B are in good agreement with simulation results for $\chi_{\mathrm{L}} \leq 1.0$. Above this, there is evident divergence between the simulated results and the MMF predictions. However, MMF theory provides predictions that are closer to simulation results than Debye theory at these higher values of χ_{L}. It is interesting to note that the initial slope parameter results from the simulations run at constant ρ^* diverge from those obtained at constant λ. The results from constant λ runs diverge less from MMF theory at $\chi_{\mathrm{L}} > 1.0$. This

is true in both the real component parameter A and the imaginary component parameter B.

It is possible to define a characteristic relaxation lifetime τ_0 from the magnetic autocorrelation function. This gives a measure of the time it takes for the system to 'forget' its initial magnetisation, and is simply defined as

$$\tau_0 = \int_0^\infty \frac{\langle \boldsymbol{M}(t) \cdot \boldsymbol{M}(0) \rangle}{\langle \boldsymbol{M}(0) \cdot \boldsymbol{M}(0) \rangle} \mathrm{d}t. \tag{6.18}$$

In the non-interacting Debye-theory case, $\tau_0 = \tau_\mathrm{B}$. A convenient expression for τ_0 follows from Eq. 6.1 which, when rearranged, gives

$$\frac{1}{i\omega}\left(\frac{\chi(\omega)}{\chi(0)} - 1\right) = \int_0^\infty \frac{\langle \boldsymbol{M}(t) \cdot \boldsymbol{M}(0) \rangle}{\langle \boldsymbol{M}(t) \cdot \boldsymbol{M}(0) \rangle} \exp(i\omega t) \mathrm{d}t. \tag{6.19}$$

Plugging Eq. 6.19 into Eq. 6.18 defines τ_0 for all systems, interacting or not, as being

$$\tau_0 = \lim_{\omega \to 0} \left[\frac{1}{i\omega}\left(\frac{\chi(\omega)}{\chi(0)} - 1\right)\right] = \lim_{\omega \to 0} \left[\frac{1}{i\omega}\left(\frac{\chi^{'}(\omega)}{\chi(0)} + \frac{i\chi^{''}(\omega)}{\chi(0)} - 1\right)\right]. \tag{6.20}$$

Since $[\chi^{'}(\omega)/\chi(0) - 1] \to 0$ when $\omega \to 0$, Eq. 6.20 reduces to

$$\tau_0 = \lim_{\omega = 0} \left[\frac{1}{\omega}\frac{\chi^{''}(\omega)}{\chi(0)}\right] = \left(\frac{3 + 2\chi_\mathrm{L}}{3 + \chi_\mathrm{L}}\right)\tau_\mathrm{B}. \tag{6.21}$$

Figure 6.8(a) provides a comparison of the theoretical predictions for these lifetimes with results from simulations. As before, non-interacting systems are in perfect agreement with the Debye-theory predictions, and Debye theory provides good agreement with simulations of interacting particles at very low χ_L only. MMF theory provides a better match with simulations at values of $\chi_\mathrm{L} \lesssim 1.0$, before the predictions diverge from the results. Again, it is clear that simulated systems run at constant λ diverge less quickly from MMF predictions than systems run at constant ρ^*.

Finally, it is possible to compare the theoretical and simulated positions of the

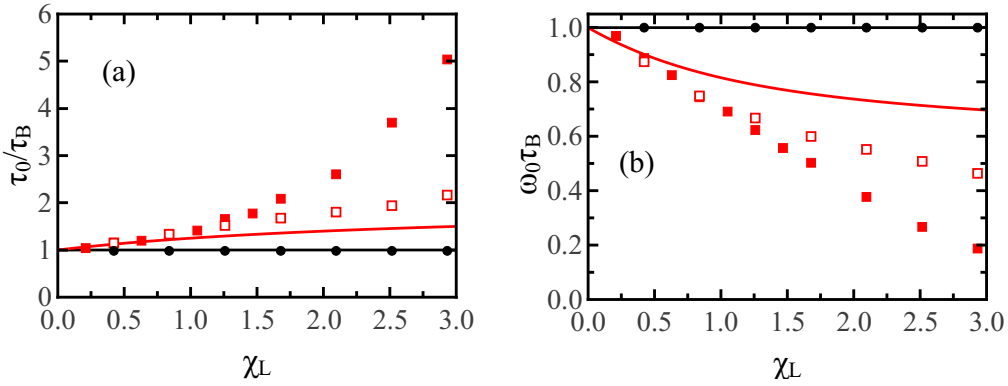

Figure 6.8: (a) Magnetic rotational relaxation time τ_0 as a function of χ_L. (b) Peak position ω_0 of the imaginary part of the DMS as a function of χ_L. Debye theory (black line) and MMF theory (red line) are shown alongside simulation results from systems of non-interacting dipolar particles (filled black circles), systems of interacting particles at constant density $\rho^* = 0.2$ (filled red squares), and systems of interacting particles at constant dipolar coupling constant $\lambda = 1.0$ (open red squares).

peak in the imaginary part of the DMS. In both theories, the peak position ω_0 can be found simply by solving $\mathrm{d}\chi''(\omega)/\mathrm{d}\omega = 0$. For Debye theory, the peak position $\omega_0 = \tau_B^{-1}$ is found to be independent of χ_L. The MMF-theory prediction for the peak position is dependent on χ_L and is given by

$$\omega_0 = \frac{1}{\tau_B}\left[\left({\chi_L}^2 + \frac{2}{3}\chi_L + 1\right)^{\frac{1}{2}} - \chi_L\right]^{\frac{1}{2}}. \tag{6.22}$$

This reduces to the Debye-theory results in the limit of $\chi_L \to 0$. These predictions are compared with simulation results in Fig. 6.8(b). The positions of the peaks in the simulated $\chi''(\omega)$ were found by fitting a Gaussian function to the tops of the peaks. This was done to ensure that small fluctuations resulting from noise would not strongly affect the numerical determination of ω_0. The methodology is validated with the non-interacting systems producing a perfect match with Debye theory at all values of χ_L. Again, the Debye theory predicts the low-χ_L limit but fails to generate accurate predictions at high χ_L for interacting particles. For systems of interacting particles, MMF theory provides accurate predictions for $\chi_L < 0.5$, but fails to predict the change in peak-frequency as χ_L is increased past this point. Also, simulation results from runs at constant λ diverge from MMF-theory predictions less quickly than simulation results from runs at constant ρ^*.

Both τ_0 and ω_0 decrease as χ_L is increased. This is attributable to the rise in the

collective motion of particles within the system. As seen before (Chapter 5), particles with higher λ have a greater propensity to form chain-like structures. While none of the systems simulated here are in the chain-forming regime, medium- to long-lived trimers and tetramers may begin to form at the higher χ_{L} tested. The orientations of individual dipolar particles forming these proto-chains may be coupled. It would therefore follow that the change in orientation of one dipole must result from a rotation of this proto-chain, leading to collective, rather than individual, motion. Furthermore, the chains should rotate more slowly than a single particle as they are larger.

For all parameters studied, MMF theory provides an accurate description of systems run at constant λ and ρ^* for values of $\chi_{\mathrm{L}} \lesssim 1.0$. Therefore, the assumption that the DMS depends only on χ_{L} seems to be correct in this region. This is the region for which MMF theory is predicted to work, and the region in which it is currently possible to manufacture ferrofluids easily. Beyond $\chi_{\mathrm{L}} = 1.0$, increasing χ_{L} by increasing only λ leads to a different susceptibility than if only ρ^* is increased. Both theories predict that $\chi(\omega)$ depends only on χ_{L}, and neither predicts a separate dependence on λ and ρ^*. It is worth emphasising that the high-ρ^* simulations resulted in a closer match to MMF-theory predictions than the equivalent high-λ simulations. The high-λ simulations were run with $\lambda \geq 2.5$. These values are very close to the dipolar coupling constants at which chains begin to form ($\lambda \simeq 4.0$). Therefore, it is possible that long-lived trimers or tetramers of dipolar particles in a linear formation are beginning to form at these values of λ. In contrast, this pre-chaining correlation is not likely to occur in dense fluids with low λ. The formation of long-lived 'chains' of particles would probably result in three-body correlations needing to be taken into account. The MMF theory was developed while only retaining the leading-order contributions to the pair correlations. It is possible that the inclusion of three-body correlations to the MMF theory would result in a decoupling of the λ and ρ^* dependence of $\chi(\omega)$, and better prediction of the DMS of systems with higher dipole moments. This effect could also result from MMF theory being truncated too early. $\chi_{\mathrm{MMF}}(\omega)$ is derived from only the leading-order terms in $\rho^*\lambda$ ($\propto \chi_{\mathrm{L}}$). It is possible that the inclusion of lower-order terms in this derivation could lead to 'mismatched' powers of λ and ρ^* occurring.

6.5 Conclusions

In this chapter, two theoretical expressions for the DMS of magnetic nanoparticles in suspensions were tested against simulation results. This was done to verify whether the MMF approach should yield more accurate predictions for the DMS of a system of interacting monodisperse dipolar particles than the Debye-theory approach. It was confirmed that the classical Debye theory predicts the behaviour of systems of non-interacting dipolar particles exactly. It was shown that the DMS of a system of interacting particles could only be predicted by Debye theory if the interactions were extremely weak ($\chi_{\mathrm{L}} \ll 1$). The MMF theory was found to be much more accurate in predicting the DMS of systems of interacting particles, with simulation results being in excellent agreement in the range $0 < \chi_{\mathrm{L}} < 1$, with a close but not exact match in the range $1 < \chi_{\mathrm{L}} < 2$. At all interacting strengths simulated, MMF-theory predictions were found to be more accurate than those produced using Debye theory.

Whereas both theories predict that the DMS is only dependent on concentration ρ^* and dipolar coupling constant λ *via* a dependence on the Langevin susceptibility χ_{L} ($\propto \rho^*\lambda$), simulation results showed that, at high χ_{L}, a system with high concentration and low dipole strength will produce a different susceptibility curve than a system with low concentration and high dipolar coupling constant. That MMF theory predicts a dependence on χ_{L} alone results from it being a perturbation theory with only the leading-order term $\rho^*\lambda$ being retained. The recent development of the second-order modified mean field theory suggest that it may be possible to systematically improve the current MMF prediction of the DMS [165]. The systems run at low dipolar coupling constants were found to have a consistently closer match with MMF theory at all densities. This is likely a result of long-lived structure beginning to form at high dipole constant.

Chapter 7

Conclusions

In this thesis, molecular simulations were used to predict and understand the behaviour of systems on timescales and lengthscale much shorter than can be easily observed experimentally. In the first part, the structures of aqueous salt solutions near and above saturation concentrations were studied to try to understand the mechanisms by which non-photochemical laser-induced nucleation (NPLIN) acts to cause these solutions to crystallise. The second part was focussed on the study of systems of dipolar particles, with a new method for simulating chain-forming particles presented, and a new theory to predict the dynamic magnetic susceptibility of dipole systems tested for systems of monodisperse dipolar particles.

The study of aqueous potassium chloride solutions demonstrated that, at very high salt concentrations, there exist long-lived amorphous clusters. These clusters form randomly and have lifetimes of similar order of magnitude as the laser-pulse duration required to induce NPLIN. This suggests that the laser may act on these amorphous clusters to reorder them somehow to form crystal nuclei. This hypothesis would support the two-step nucleation model proposed by Erdemir *et al.* [17], with the first step being the creation of these areas of high local solute density, and the second step being the reordering of the clusters into crystal nuclei. Though the amorphous clusters have lifetimes in the $10 - 100$ ps region, it is nearly impossible to accurately observe solvated non-crystallised solute on these timescales experimentally.

Another proposed mechanism of NPLIN is that the laser pulse acts on impurities in the solution, causing them to heat up and create nanobubbles that may induce a metastable system to crystallise. As the existence of such impurities is

impossible to demonstrate experimentally, simulation offers the perfect solution to study the effects of a hot impurity on a solution near crystallisation. The study of aqueous potassium chloride solutions showed that it is very difficult to observe crystallisation of this system in the simulation timescale, therefore the system was changed to aqueous sodium chloride solutions as these are proven to crystallise near experimental saturation concentration. To begin, the simulation saturation concentration, that is, the maximum concentration at which long-lived large crystals are no longer observed within the simulation timescale, was found. From this, the effects that adding and heating a spherical carbon impurity had on the structure of the salt solution were studied. It was found that the heating of the impurity results in a depletion of ions surrounding the impurity. When the heat added to the system was not great enough to vaporise the solution, the only noticeable effect of the hot impurity on the water was a reduction in the total number of molecules in the first hydration shell of the impurity. When the energy was high enough to cause vaporisation, the solution surrounding the impurity became ion depleted on a faster scale than water evaporated, implying that nanobubbles created by impurity heating are highly unlikely to have an effect in the NPLIN process. It is possible that heated impurities still play a role in NPLIN, and a mechanism is proposed whereby the heating of the impurity creates a flux of ions away from the impurity into the solution $15 - 20$ Å from the surface of the impurity, which causes amorphous pre-clusters in this region to become supersaturated and crystallise.

The second part of this work was concerned with the study of ferrofluids. These systems were modelled as spherical particles with a magnetic dipole moment that interacts *via* long-ranged dipole-dipole interactions. These long-ranged interactions are very computationally expensive, and reducing the number of long-ranged interactions needed would result in faster simulations. In the 1970s, Stell and coworkers demonstrated that it is possible to model the long-ranged dipole-dipole interaction as a short-ranged many-body interaction [145]. Here, the dipole-dipole interaction was modelled as a short-ranged many-body interaction composed of only the leading-order two- and three-body terms of the expansion proposed by Stell *et al.* The structures produced by fluids interacting *via* this many-body potential were compared with structures from equivalent fluids run using the dipole-dipole interaction. It was found that, for low values of dipolar coupling strength, the many-body approximation is able to reproduce the structure observed in dipole systems. For higher dipolar coupling strength, however, the many-body approximation over-emphasises the characteristic chaining

observed in systems of dipolar particles, with more rigid chains than expected being formed. A method to reconnect the structure produced by both systems is proposed, and it was demonstrated that, by altering some parameters in the many-body potential, the structure observed in equivalent dipole systems is reproduced. This work concludes with a description of the effects that increasing the strength of the three-body, chain-inducing part of the many-body potential has on the vapour-liquid phase transition. It was shown that, as the ability of the system to form chains is increased, the critical temperature and density of the system decrease. There is a point at which the critical temperature of the system is expected to reach zero, implying that the vapour-liquid phase transition disappears completely at a certain degree of chaining.

The study of ferrofluids was continued by testing a new theory for predicting the dynamic magnetic susceptibility of systems of dipolar particles. Ivanov *et al.* proposed this new, modified mean-field (MMF) theory and tested it against the preceding Debye theory for an experimental system composed of polydisperse dipolar particles. The new theory was shown to generate better predictions [162]. However, Ivanov *et al.* conclude by emphasising that, while the predictive improvements of the new theory were noticeable in a polydisperse system, the greater accuracy of the new theory over the original Debye theory would be emphasised more dramatically if a monodisperse system of dipolar particles was used. As creating monodisperse systems of dipolar particles is incredibly difficult experimentally, Brownian dynamics simulations were used to compare the results obtained from simulated monodisperse systems of dipolar particles with those predicted by Debye theory and the new MMF theory. For all systems tested, the new theory was found to predict the dynamic magnetic susceptibility more accurately than the original Debye model. Furthermore, the new theory was able to predict the dynamic susceptibility exactly over most of the experimentally achievable range of dipole strengths. At very high dipolar coupling strength, the theory deviated from simulation results, but was still significantly more accurate than Debye theory. Finally, because the new theory is based on fundamental statistical mechanics, it can be can be systematically improved to obtain better and better predictions.

If nothing else, this work has demonstrated that simulation holds a central place in science. It is possible to use simulations to predict effects that can not yet be observed experimentally, and it is possible to use simulations to test existing theories. As a result, the scope and accuracy of simulation are being increased.

The link between the microscopic and the macroscopic regimes has never been so clear, and simulations allow us to sneak a peak at what the future holds in store.

Bibliography

[1] Garetz, B. A.; Aber, J. E.; Goddard, N. L.; Young, R. G.; Myerson, A. S. *Physical Review Letters* **1996,** *77,* 3475–3476.

[2] Zaccaro, J.; Matic, J.; Myerson, A. S.; Garetz, B. A. *Crystal Growth & Design* **2001,** *1,* 5–8.

[3] Garetz, B.; Matic, J.; Myerson, A. *Physical Review Letters* **2002,** *89,* 175501.

[4] Sun, X.; Garetz, B. A.; Myerson, A. S. *Crystal Growth & Design* **2006,** *6,* 684.

[5] Lee, I. S.; Evans, J. M. B.; Erdemir, D.; Lee, A. Y.; Garetz, B. A.; Myerson, A. S. *Crystal Growth & Design* **2008,** *8,* 4255–4261.

[6] Sun, X.; Garetz, B. A.; Myerson, A. S. *Crystal Growth & Design* **2008,** *8,* 1720–1722.

[7] Alexander, A. J.; Camp, P. J. *Crystal Growth & Design* **2009,** *9,* 958963.

[8] Ward, M. R.; Alexander, A. J. *Crystal Growth & Design* **2012,** *12,* 45544561.

[9] Ward, M. R.; Copeland, G. W.; Alexander, A. J. *The Journal of Chemical Physics* **2011,** *135,* 114508_1114508_8.

[10] Ward, M. R.; McHugh, S.; Alexander, A. J. *Physical Chemistry Chemical Physics* **2012,** *14,* 90–3.

[11] Ward, M. R.; Jamieson, W. J.; Leckey, C. A.; Alexander, A. J. *The Journal of Chemical Physics* **2015,** *142,* 144501.

[12] Knott, B. C.; Doherty, M. F.; Peters, B. *The Journal of Chemical Physics* **2011,** *134,* 154501.

[13] Turnbull, D.; Fisher, J. C. *The Journal of Chemical Physics* **1949,** *17,* 71–73.

[14] Kim, Y.; Park, C. B.; Chen, P.; Thompson, R. B. *Soft Matter* **2011,** *7,* 7351–7358.

[15] Merikanto, J.; Zapadinsky, E.; Lauri, A.; Vehkamki, H. *Physical Review Letters* **2007,** *98,* 145702.

[16] Lauri, A.; Zapadinsky, E.; Vehkamki, H.; Kulmala, M. *The Journal of Chemical Physics* **2006,** *125,* 164712.

[17] Erdemir, D.; Lee, A. Y.; Myerson, A. S. *Accounts of Chemical Research* **2009,** *42,* 621–629.

[18] Knott, B. C.; LaRue, J. L.; Wodtke, A. M.; Doherty, M. F.; Peters, B. *The Journal of Chemical Physics* **2011,** *134,* 171102.

[19] Alder, B. J.; Wainwright, T. E. *The Journal of Chemical Physics* **1957,** *27,* 1208–1209.

[20] Alpert, P. A.; Aller, J. Y.; Knopf, D. A. *Atmospheric Chemistry and Physics* **2011,** *11,* 5539–5555.

[21] Vega, C.; Sanz, E.; Abascal, J. L. F.; Noya, E. G. *Journal of Physics: Condensed Matter* **2008,** *20,* 153101.

[22] Papell, S. S. "Low viscocity magnetic fluid obtained by the colloidal suspension of magnetic particles", US Patent 3215572, 1965.

[23] Hezaveh, H.; Fazlali, A.; Noshadi, I. *Journal of the Taiwan Institute of Chemical Engineers* **2012,** *43,* 159–164.

[24] Rosensweig, R. E. *Ferrohydrodynamics;* Dover Publications: 1997.

[25] Robert, K. "Ferrofluid composition", US Patent 3700595, 1972.

[26] Teixeira, P. I. C.; Tavares, J. M.; Gama, M. M. T. d. *Journal of Physics: Condensed Matter* **2000,** *12,* R411.

[27] Tsuda, S.; Rosensweig, R. E. "Ferrofluid centered voice coil speaker", US Patent 7729504, 2007.

[28] Mahmoudi, M.; Hosseinkhani, H.; Hosseinkhani, M.; Boutry, S.; Simchi, A.; Journeay, W. S.; Subramani, K.; Laurent, S. *Chemical Reviews* **2011,** *111,* 253–280.

[29] Casula, M. F.; Floris, P.; Innocenti, C.; Lascialfari, A.; Marinone, M.; Corti, M.; Sperling, R. A.; Parak, W. J.; Sangregorio, C. *Chemistry of Materials* **2010,** *22,* 1739–1748.

[30] Corti, M.; Lascialfari, A.; Marinone, M.; Masotti, A.; Micotti, E.; Orsini, F.; Ortaggi, G.; Poletti, G.; Innocenti, C.; Sangregorio, C. *Journal of Magnetism and Magnetic Materials* **2008,** *320,* e316–e319.

[31] Corti, M.; Lascialfari, A.; Micotti, E.; Castellano, A.; Donativi, M.; Quarta, A.; Cozzoli, P. D.; Manna, L.; Pellegrino, T.; Sangregorio, C. *Journal of Magnetism and Magnetic Materials* **2008,** *320,* e320–e323.

[32] Mahmoudi, M.; Sant, S.; Wang, B.; Laurent, S.; Sen, T. *Advanced Drug Delivery Reviews* **2011,** *63,* 24–46.

[33] L. Raikher, Y.; Stepanov, V. I. *Journal of Magnetism and Magnetic Materials* **2014,** *368,* 421–427.

[34] Maier-Hauff, K.; Ulrich, F.; Nestler, D.; Niehoff, H.; Wust, P.; Thiesen, B.; Orawa, H.; Budach, V.; Jordan, A. *Journal of Neuro-Oncology* **2010,** *103,* 317–324.

[35] Durán, J.; Arias, J.; Gallardo, V.; Delgado, A. *Journal of Pharmaceutical Sciences* **2008,** *97,* 2948–2983.

[36] Fortin, J.-P.; Wilhelm, C.; Servais, J.; Mnager, C.; Bacri, J.-C.; Gazeau, F. *Journal of the American Chemical Society* **2007,** *129,* 2628–2635.

[37] Maier-Hauff, K.; Rothe, R.; Scholz, R.; Gneveckow, U.; Wust, P.; Thiesen, B.; Feussner, A.; Deimling, A. v.; Waldoefner, N.; Felix, R.; Jordan, A. *Journal of Neuro-Oncology* **2006,** *81,* 53–60.

[38] Jordan, A.; Scholz, R.; Maier-Hauff, K.; Landeghem, F. K. H. v.; Waldoefner, N.; Teichgraeber, U.; Pinkernelle, J.; Bruhn, H.; Neumann, F.; Thiesen, B.; Deimling, A. v.; Felix, R. *Journal of Neuro-Oncology* **2005,** *78,* 7–14.

[39] Albernoz, A.; Jacobo, S. E. *Journal of Magnetism and Magnetic Materials* **2006,** *305,* 12-15.

[40] Raj, K.; Lennon, J. "Ferrofluid sculpting apparatus", US Patent 6290894, 2001.

[41] Ivanov, A. O.; Kantorovich, S. S.; Reznikov, E. N.; Holm, C.; Pshenichnikov, A. F.; Lebedev, A. V.; Chremos, A.; Camp, P. J. *Physical Review E* **2007,** *75,* 061405.

[42] Sekar, K.; Oza, J. *bioRxiv* **2015,** 022590.

[43] Xie, J.; Chen, K.; Chen, X. *Nano research* **2009,** *2,* 261–278.

[44] Tan, S. H.; Nguyen, N.-T. *Physical Review E* **2011,** *84,* 036317.

[45] Klokkenburg, M.; Erné, B. H.; Meeldijk, J. D.; Wiedenmann, A.; Petukhov, A. V.; Dullens, R. P. A.; Philipse, A. P. *Physical Review Letters* **2006,** *97,* 185702.

[46] de Gennes, P. G.; A., P. P. *Physik de Kondensierten Materie* **1970,** *11,* 189-198.

[47] Wei, D.; Patey, G. N. *Physical Review Letters* **1992,** *68,* 2043.

[48] Wei, D.; Patey, G. N. *Physical Review Letters* **1992,** *46,* 7783.

[49] Alder, B. J.; Wainwright, T. E. *The Journal of Chemical Physics* **1959,** *31,* 459–466.

[50] Plimpton, S. *Journal of Computational Physics* **1995,** *117,* 1-19.

[51] Martínez, L.; Andrade, R.; Birgin, E. G.; Martínez, J. M. *Journal of Computational Chemistry* **2009,** 2157–2164.

[52] Verlet, L. *Physical Review* **1967,** *159,* 98-103.

[53] Verlet, L. *Physical Review* **1968,** *165,* 201.

[54] Metropolis, N. *Los Alamos Science* **1987,** *15,* 125-130.

[55] Eckhardt, R. *Los Alamos Science* **1987,** *15,* 131-136.

[56] Metropolis, N.; Rosenbluth, A. W.; Rosenbluth, M. N.; Teller, A. H.; Teller, E. *The Journal of Chemical Physics* **1953,** *21,* 1087–1092.

[57] Weeks, J. D.; Chandler, D.; Andersen, H. C. *The Journal of Chemical Physics* **1971,** *54,* 5237–5247.

[58] Allen, M. P.; Tildesley, D. J. *Computer Simulation of Liquids;* Oxford University Press: New York, 1987.

[59] Frenkel, D.; Smit, B. *Understanding Molecular Simulation From Algorithms to Applications;* Academic Press: London, Second Edi ed.; 2002.

[60] Frenkel, D. *The European Physical Journal Plus* **2013,** *128,* 10.

[61] Hansen, J.-P.; McDonald, I. R. *Theory of Simple Liquids;* Academic Press: London, 3rd ed.; 2006.

[62] Holden, A.; Morrison, P. *Crystals and Crystal Growing;* The MIT Press: Cambridge, Mass, 1st MIT edition ed.; 1982.

[63] Burger, M.; Capasso, V.; Bellomo, N. *Mathematical Models & Methods in Applied Sciences* **2001,** *11,* 1029.

[64] Revalor, E.; Hammadi, Z.; Astier, J.-P.; Grossier, R.; Garcia, E.; Hoff, C.; Furuta, K.; Okustu, T.; Morin, R.; Veesler, S. *Journal of Crystal Growth* **2010,** *312,* 939–946.

[65] Goh, L.; Chen, K.; Bhamidi, V.; He, G.; Kee, N. C. S.; Kenis, P. J. A.; Zukoski, C. F.; Braatz, R. D. *Crystal Growth & Design* **2010,** *10,* 2515–2521.

[66] Durán-Olivencia, M. A.; Otálora, F. *Journal of Crystal Growth* **2013,** *380,* 247–255.

[67] Maggioni, G. M.; Mazzotti, M. *Faraday Discussions* **2015,** *179,* 359–382.

[68] Ward, M. R.; Ballingall, I.; Costen, M. L.; McKendrick, K. G.; Alexander, A. J. *Chemical Physics Letters* **2009,** *481,* 25-28.

[69] Lyubartsev, A. P.; Laaksonen, A. *The Journal of Physical Chemistry* **1996,** *100,* 16410–16418.

[70] Brodholt, J. P. *Chemical Geology* **1998,** *151,* 11–19.

[71] Chowdhuri, S.; Chandra, A. *The Journal of Chemical Physics* **2001,** *115,* 3732.

[72] Zahn, D. *Physical Review Letters* **2004,** *92,* 040801.

[73] Valeriani, C.; Sanz, E.; Frenkel, D. *The Journal of Chemical Physics* **2005,** *122,* 194501.

[74] Kawska, A.; Brickmann, J.; Kniep, R.; Hochrein, O.; Zahn, D. *The Journal of Chemical Physics* **2006,** *124,* 024513.

[75] Yamanaka, S.; Shimosaka, A.; Shirakawa, Y.; Hidaka, J. *Journal of Nanoparticle Research* **2009,** *12,* 831–839.

[76] Kadota, K.; Shirakawa, Y.; Wada, M.; Shimosaka, A.; Hidaka, J. *Journal of Molecular Liquids* **2012,** *166,* 31–39.

[77] Chakraborty, D.; Patey, G. N. *The Journal of Physical Chemistry Letters* **2013,** *4,* 573–578.

[78] Chakraborty, D.; Patey, G. N. *Chemical Physics Letters* **2013,** *587,* 25–29.

[79] Mester, Z.; Panagiotopoulos, A. Z. *The Journal of Chemical Physics* **2015,** *143,* 044505.

[80] Lanaro, G.; Patey, G. N. *The Journal of Physical Chemistry B* **2015,** *119,* 4275–4283.

[81] Moucka, F.; Nezbeda, I.; Smith, W. R. *Journal of Chemical Theory and Computation* **2015,** *11,* 1756-1764.

[82] Vega, C.; Abascal, J. L. F.; Sanz, E.; MacDowell, L. G.; McBride, C. *Journal of Physics: Condensed Matter* **2005,** *17,* S3283.

[83] Vega, C.; Sanz, E.; Abascal, J. L. F.; Noya, E. G. *Journal of Physics: Condensed Matter* **2008,** *20,* 153101.

[84] Vega, C.; Abascal, J. L. F.; Conde, M. M.; Aragones, J. L. *Faraday Discussions* **2008,** *141,* 251–276.

[85] Kiss, P. T.; Baranyai, A. *The Journal of Chemical Physics* **2011,** *134,* 054106.

[86] Dang, L. X. *Journal of the American Chemical Society* **1995,** *117,* 69546960.

[87] Berendsen, H. J. C.; Grigera, J. R.; Straatsma, T. P. *The Journal of Physical Chemistry* **1987,** *91,* 6269–6271.

[88] Price, D. J.; Brooks III, C. L. *The Journal of Chemical Physics* **2004,** *121,* 10096–10103.

[89] Horn, H. W.; Swope, W. C.; Pitera, J. W. *The Journal of Chemical Physics* **2005,** *123,* 194504.

[90] Joung, I. S.; Cheatham, T. E. *The Journal of Physical Chemistry B* **2008,** *112,* 902041.

[91] Joung, I. S.; Cheatham III, T. E. *The Journal of Physical Chemistry B* **2009,** *113,* 1327913290.

[92] Benavides, A. L.; Aragones, J. L.; Vega, C. *The Journal of Chemical Physics* **2016,** *144,* 124504.

[93] Koneshan, S.; Rasaiah, J. C.; Lee, S. H. *The Journal of Physical Chemistry B* **1998,** *5647,* 41934204.

[94] Tuckerman, M. E.; Alejandre, J.; López-Rendón, R.; Jochim, A. L.; Martyna, G. J. *Journal of Physics A: Mathematical and General* **2006,** *39,* 56295651.

[95] Hockney, R. W.; Eastwood, J. W. *Computer Simulation Using Particles;* IOP Publishing: Bristol, 1988.

[96] Stillinger, F. H. *The Journal of Chemical Physics* **1963,** *38,* 1486.

[97] Wedekind, J.; Reguera, D. *The Journal of Chemical Physics* **2007,** *127,* 154516.

[98] Wedekind, J.; Strey, R.; Reguera, D. *The Journal of Chemical Physics* **2007,** *126,* 134103.

[99] Zhang, H.-L.,; Han, S.-J., *Journal of Chemical & Engineering Data* **1996,** *41,* 516–520.

[100] Chambers, J. F.; Stokes, J. M.; Stokes, R. H. *Journal of Physical Chemistry* **1956,** *111,* 67.

[101] Friedman, A. M.; Kennedy, J. W. *Journal of the American Chemical Society* **1955,** *77,* 44994501.

[102] Adleman, J. R.; Boyd, D. A.; Goodwin, D. G.; Psaltis, D. *Nano Letters* **2009,** *9,* 4417–4423.

[103] Lukianova-Hleb, E.; Hu, Y.; Latterini, L.; Tarpani, L.; Lee, S.; Drezek, R. A.; Hafner, J. H.; Lapotko, D. O. *ACS Nano* **2010,** *4,* 2109–2123.

[104] Carlson, M. T.; Green, A. J.; Richardson, H. H. *Nano Letters* **2012,** *12,* 1534–1537.

[105] Fang, Z.; Zhen, Y.-R.; Neumann, O.; Polman, A.; Garca de Abajo, F. J.; Nordlander, P.; Halas, N. J. *Nano Letters* **2013,** *13,* 1736–1742.

[106] Lombard, J.; Biben, T.; Merabia, S. *Physical Review Letters* **2014,** *112,* 105701.

[107] Sasikumar, K.; Keblinski, P. *The Journal of Chemical Physics* **2014,** *141,* 234508.

[108] Chen, X.; Munjiza, A.; Zhang, K.; Wen, D. *The Journal of Physical Chemistry C* **2014,** *118,* 1285–1293.

[109] Zimmermann, N. E. R.; Vorselaars, B.; Quigley, D.; Peters, B. *Journal of the American Chemical Society* **2015,** *137,* 13352–13361.

[110] Sun, X.; Chang, T.-m.; Cao, Y.; Niwayama, S.; Hase, W. L.; Dang, L. X. *The Journal of Physical Chemistry B* **2009,** *113,* 6473–6477.

[111] Dang, L. X.; Feller, D. *The Journal of Physical Chemistry B* **2000,** *104,* 4403–4407.

[112] Wolde, P. R. t.; Frenkel, D. *The Journal of Chemical Physics* **1998,** *109,* 9901–9918.

[113] Steinhardt, P. J.; Nelson, D. R.; Ronchetti, M. *Physical Review B* **1983,** *28,* 784–805.

[114] Valeriani, C.; Camp, P. J.; Zwanikken, J. W.; van Roij, R.; Dijkstra, M. *Soft Matter* **2010,** *6,* 2793.

[115] Errington, J. R.; Debenedetti, P. G.; Torquato, S. *The Journal of Chemical Physics* **2003,** *118,* 2256–2263.

[116] Wang, Y.; Teitel, S.; Dellago, C. *The Journal of Chemical Physics* **2005,** *122,* 214722.

[117] Lechner, W.; Dellago, C. *The Journal of Chemical Physics* **2008,** *129,* 114707.

[118] Lechner, W.; Dellago, C.; Bolhuis, P. G. *Physical Review Letters* **2011,** *106,* 085701.

[119] ten Wolde, P. R.; Ruiz-Montero, M. J.; Frenkel, D. *Physical Review Letters* **1995,** *75,* 2714–2717.

[120] ten Wolde, P. R.; Ruiz-Montero, M. J.; Frenkel, D. *The Journal of Chemical Physics* **1996,** *104,* 9932.

[121] Auer, S.; Frenkel, D. *The Journal of Chemical Physics* **2004,** *120,* 3015–3029.

[122] Trypu, M.; Kiekowska, U.; Chaat, M. *Journal of Chemical & Engineering Data* **2002,** *47,* 765–767.

[123] Freiser, M. J. *Physical Review Letters* **1970,** *24,* 1041–1043.

[124] McMillan, W. L. *Physical Review A* **1971,** *4,* 1238–1246.

[125] Klokkenburg, M.; Dullens, R. P. A.; Kegel, W. K.; Erné, B. H.; Philipse, A. P. *Physical Review Letters* **2006,** *96,* 037203.

[126] Camp, P. J.; Patey, G. N. *Physical Review E* **2000,** *62,* 5403–5408.

[127] Sreekumari, A.; Ilg, P. *Physical Review E.* **2013,** *88,*.

[128] Caillol, J.-M. *The Journal of Chemical Physics* **1993,** *98,* 9835–9849.

[129] Weis, J. J.; Levesque, D. *Physical Review E* **1993,** *48,* 3728–3740.

[130] Levesque, D.; Weis, J. J. *Physical Review E* **1994,** *49,* 5131–5140.

[131] Stevens, M. J.; Grest, G. S. *Physical Review E* **1995,** *51,* 5976–5984.

[132] Stevens, M. J.; Grest, G. S. *Physical Review E* **1995,** *51,* 5962–5975.

[133] Ganzenmüller, G.; Camp, P. J. *The Journal of Chemical Physics* **2007,** *127,* 154504.

[134] Ganzenmüller, G.; Camp, P. J. *The Journal of Chemical Physics* **2007,** *126,* 191104.

[135] Bartke, J.; Hentschke, R. *Physical Review E* **2007,** *75,* 061503.

[136] Hentschke, R.; Bartke, J.; Pesth, F. *Physical Review E* **2007,** *75,* 011506.

[137] Ivanov, A. O.; Kantorovich, S. S.; Camp, P. J. *Physical Review E* **2008,** *77,* 013501.

[138] Hentschke, R.; Bartke, J. *Physical Review E* **2008,** *77,* 013502.

[139] Ganzenmüller, G.; Patey, G. N.; Camp, P. J. *Molecular Physics* **2009,** *107,* 403-413.

[140] Camp, P. J.; Shelley, J. C.; Patey, G. N. *Physical Review Letters* **2000,** *84,* 115–118.

[141] Jia, R.; Braun, H.; Hentschke, R. *Physical Review E* **2010,** *82,* 062501.

[142] Rovigatti, L.; Russo, J.; Sciortino, F. *Physical Review Letters* **2011,** *107,* 237801.

[143] Rovigatti, L.; Russo, J.; Sciortino, F. *Soft Matter* **2012,** *8,* 6310-6319.

[144] Dussi, S.; Rovigatti, L.; Sciortino, F. *Molecular Physics* **2013,** *111,* 3608–3617.

[145] Stell, G. *Physical Review Letters* **1974,** *32,* 286-288.

[146] Rasaiah, J. C.; Stell, G. *Chemical Physics Letters* **1974,** *25,* 519-522.

[147] Linder, B. *The Journal of Chemical Physics* **1964,** *40,* 2003-2009.

[148] Axilrod, B. M.; Teller, E. *The Journal of Chemical Physics* **1943,** *11,* 299.

[149] Attard, P. *Physical Review A* **1992,** *45,* 3659-3669.

[150] Attard, P. *Physical Review A* **1992,** *45,* 5649-5653.

[151] Anta, J. A.; Lomba, E.; Lombardero, M. *Physical Review E* **1997,** *55,* 2707-2712.

[152] Shi, W.; Johnson, J. K. *Fluid Phase Equilibria* **2001,** *187-188,* 171-191.

[153] Panagiotopoulos, A. Z. *Journal of Physics: Condensed Matter* **2000,** *12,* R25.

[154] Elfimova, E. A.; Ivanov, A. O.; Camp, P. J. *The Journal of Chemical Physics* **2012,** *136,* 194502.

[155] Smit, B. *The Journal of Chemical Physics* **1992,** *96,* 8639–8640.

[156] Weissleder, R.; Reimer, P. *European Radiology* **1993,** *3,* 198–212.

[157] Bulte, J. W. M.; Kraitchman, D. L. *NMR in Biomedicine* **2004,** *17,* 484–499.

[158] Taukulis, R.; Cēbers, A. *Physical Review E* **2012,** *86,* 061405.

[159] Lévy, M.; Gazeau, F.; Wilhelm, C.; Neveu, S.; Devaud, M.; Levitz, P. *The Journal of Physical Chemistry C* **2013,** *117,* 15369–15374.

[160] Hergt, R.; Hiergeist, R.; Hilger, I.; Kaiser, W. A.; Lapatnikov, Y.; Margel, S.; Richter, U. *Journal of Magnetism and Magnetic Materials* **2004,** *270,* 345–357.

[161] Müller, R.; Hergt, R.; Zeisberger, M.; Gawalek, W. *Journal of Magnetism and Magnetic Materials* **2005,** *289,* 13–16.

[162] Ivanov, A. O.; Zverev, V.; Kantorovich, S. S. *Soft Matter* **2016,** .

[163] Ivanov, A. O.; Kuznetsova, O. B. *Physical Review E* **2001,** *64,* 041405.

[164] Langevin, P. *Journal de Physique Théorique Appliquée* **1905,** *4,* 678–693.

[165] Ivanov, A. O.; Kuznetsova, O. B. *Colloid Journal* **2006,** *68,* 430–440.

Appendix – List of Ph.D. publications

1. Sindt, J. O.; Alexander, A. J.; and Camp, P. J. "Structure and Dynamics of Potassium Chloride in Aqueous Solution" *Journal of Physical Chemistry B* **118**, 9404–9413 (2014)

2. Sindt, J. O. and Camp, P. J. "Simulations of dipolar fluids using effective many-body isotropic interactions" *Journal of Chemical Physics* **143**, 024501 (2015)

3. Elfimova, E. A.; Ivanov, A. I.; Sindt, J. O.; and Camp, P. J. "Thermodynamics of the Stockmayer fluid in an applied field" *Molecular Physics* **113**, 3717–3728 (2015)

4. Waterson, C. N.; Sindt, J. O.; Cheng, J.; Tasker, P. T.; and Morrison, C. A. "First-Principles Study on Ligand Binding and Positional Disorder in Pentlandite" *Journal of Physical Chemistry C* **119**, 25457–25468 (2015)

5. Sindt, J. O; Camp, P. J.; Kantorovich, S. S.; Elfimova, E. A; and Ivanov, A. O. "The influence of dipolar interactions on the magnetic susceptibility spectra of ferrofluids" *Physical Review E* **93** 063117 (2016)